Title
Structural and Phonon Transmission Study of Ge-Au-Ge Eutectically Bonded Interfaces

Author
Knowlton, W.B.

Publication Date
1995-07-01

LBL-37582
UC-404

Center for Advanced Materials

CAM

Structural and Phonon Transmission Study of Ge-Au-Ge Eutectically Bonded Interfaces

W.B. Knowlton
(M.S. Thesis)

July 1995

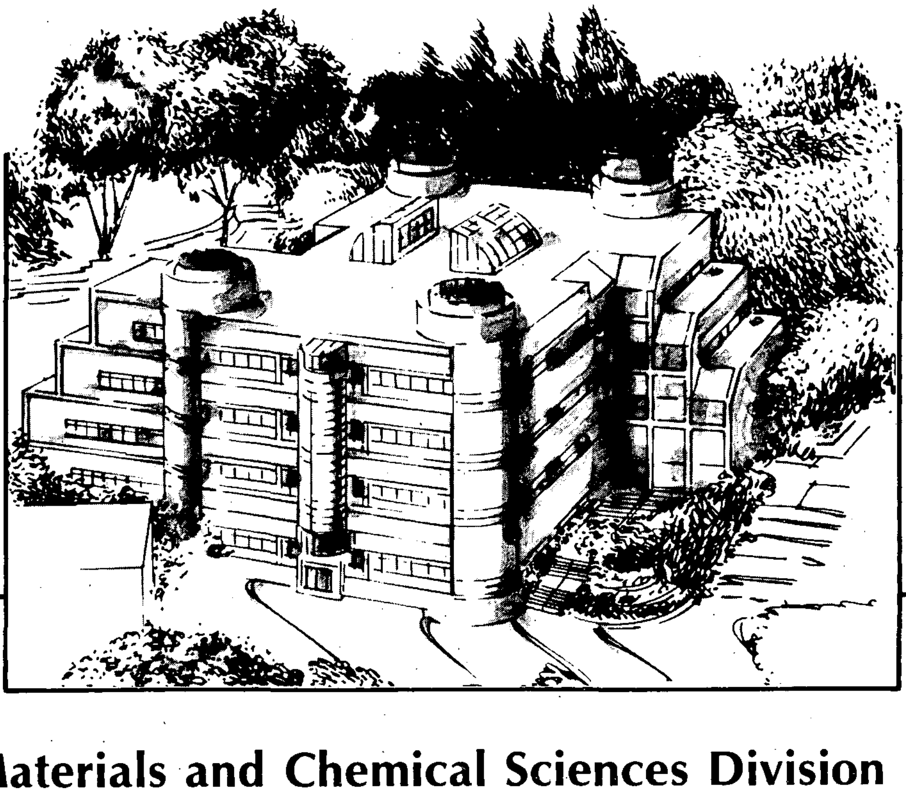

Materials and Chemical Sciences Division

Lawrence Berkeley Laboratory • University of California

ONE CYCLOTRON ROAD, BERKELEY, CA 94720 • (415) 486-4755

Prepared for the U.S. Department of Energy under Contract DE-AC03-76SF00098

LBL-37582
UC-404

Structural and Phonon Transmission Study of Ge-Au-Ge Eutectically Bonded Interfaces

William Barthélémy Knowlton
M.S. Thesis

Department of Materials Science and Mineral Engineering
University of California, Berkeley

and

Materials Sciences Division
Lawrence Berkeley Laboratory
University of California
Berkeley, CA 94720

July 1995

This work was supported by the Director, Office of Energy Research, Office of Basic Energy Sciences, Materials Sciences Division, of the U.S. Department of Energy under Contract No. DE-AC03-76SF00098.

Structural and Phonon Transmission Study of Ge-Au-Ge Eutectically Bonded Interfaces

by

William Barthélémy Knowlton

B. S. (University of California at Berkeley) 1992

A thesis submitted in partial satisfaction of the

requirements for the degree of

Master of Science

in

Engineering-Materials Science and Mineral Engineering

in the

GRADUATE DIVISION

of the

UNIVERSITY of CALIFORNIA at BERKELEY

Committee in charge:

Professor Eugene E. Haller, Chair
Dr. David Loretto
Professor Bernard Sadoulet

1995

Table of Contents

Acknowledgments

There are many people, in the past and in the present, to whom I am gratefully thankful for helping me reach the point where I am today. And, it is in this section that I wish to acknowledge and thank them. Eugene Haller gave me the opportunity as an undergraduate, and now as a graduate, to pursue my academic goals. He also had to toil through this thesis and provided constructive suggestions. It was Kohei Itoh who chose me, as an undergraduate, to work with him on several projects. Kohei did a considerable amount of the work which is presented in this thesis including much of the phonon imaging experiments and many of the transmission electron microscopy (TEM) micrographs. Without Jeff Beeman's teaching skills, help in the lab and many discussions, this work could not have been done. John Emes collaborated on much of the work presented here and was an invaluable source of information. David Loretto not only took the time to read and edit this thesis, he also performed all the TEM in this study at the National Center for Electron Microscopy. The Jim Wolfe group at the University of Illinois at Urbana-Champaigne performed the phonon imaging experiments in their lab. They include Madeline Msall, Ben Wieman, Matt Hauser, and others. Bernard Sadoulet read and edited this work and provided useful suggestions. Without his laboratory and graduate students, especially Walter Stockwell, the P2 experiment could not have been done.

The technical assistance I received was excellent. Wendy Swider performed the TEM sample preparation and developed several TEM micrographs. Steve Rothway taught me how to use many of the tools in the machine shop. Without his help, many of the "rigs" I built would not exist. Rodney Post taught and allowed me to use his

interferometer on a moments notice. Kevin Roderick performed the ion implantation for the P2 device.

Many graduate students and staff in the group contributed to this work. To all of them I thank. Kristin Duxstad, Oscar Dubon, Hilary B. Cherry, and Jim Walker helped with editing and figures.

There were many people in the past that I am indebted to for their impact on my academic success thus far. And their are several who I especially wish to thank and acknowledge. I am very much appreciative to D. Jay Seibens, a friend I met in the oil fields, who convinced me that I was intelligent enough to succeed in college. I give very warm thanks to Joseph Grim, my chemistry instructor at Sacramento City College who made me strive to great lengths in order to succeed.

Of course, I would not have been able to attain the goals I have thus far without my immediate family. My mother, Simone, has supported me every step of the way. At times, she gave me the extra push I needed. My sister, Lorraine Lyvia (Loly), and her husband, Les, were always supportive. I also wish to thank them for giving me my nephew Tyler. Difficult times were overcome because of Timothy M. Rogers - the big brother I never had. Although he is not here in the physical sense, he is here in the spiritual sense. He is my father, Bill, who encouraged my academic path and substantiated it with "care packages" of food every time he visited.

I am very grateful for the support of my pack: Amy, Duke, Bica, and Selway. The last three took me on many walks to relieve my stress. Amy provided me with love and many hours of editing. Without her, you would not be reading this thesis. To those that I have forgotten, I apologize. Time, not disregard, was the reason.

This work has been supported by the Director, Office of Energy Research, Office of Basic Energy Sciences, Materials Sciences Division of the U.S. Department of Energy under Contract No. DE-AC03-76SF00098.

1. Introduction

The driving force for this study is the quest to answer one of the fundamental questions of humankind: what is the origin of the universe? One part of the answer to this question is given by the "Big Bang" theory. One weakness of this theory is that a significant amount of the universal mass needed to validate the Big Bang theory is missing (i.e., has not been detected). This has spurred the search for this missing or "dark" matter. Several candidates for dark matter have been postulated. It is for one of them, referred to as weakly interacting particles (WIMPS), that researchers at the Center for Particle Astrophysics (CfPA), a National Science Foundation (NSF) Center in the Physics Department at University of California at Berkeley are striving to find. If they do find this elusive matter, then the Big Bang theory would be strengthened enormously.

By what means can one detect the signature of the evasive WIMP? Due to the lack of electric charge, the WIMP is believed to interact with matter much like a neutrino. Hence, if WIMP interaction occurs within a solid, the WIMPs will interact mainly with the solid's nuclei and not with the solids charged particles. Two types of excitation occur due to nucleonic interaction: nuclear recoil and electron recoil. About 90% of the nuclear recoil energy produces phonons, while the remaining nuclear recoil energy causes electronic excitation (ionization). Approximately 66% of the electron recoil energy generates phonons, and the remaining energy causes electronic excitation (ionization). Therefore, most of the energy from the WIMP interaction produces phonons. Phonon detection methods are well developed. Bolometers operating at low temperature act as thermometers and can sensitively measure minute temperature rises. In the case of WIMP detection, a bolometer by itself is insufficient. Since the WIMP is so elusive, a significant number of nuclei (i.e., a large mass) are required to improve the chances of a WIMP encounter. The large detector mass acts essentially as an antenna. The requirements of the antenna include: as previously mentioned, a large size, an attached bolometer to detect the phonons produced by a particle encounter, and ideally all the phonons should reach the bolometer unhindered. The last property requires that the phonons propagate through the antenna unhindered, therefore the antenna is preferably a pure single crystal. Additionally, it requires that the phonons pass through the interface between the antenna and the bolometer unobstructed. It is the last requirement on which this study is focused.

The method of choice for attaching the bolometer to the antenna is either by conductive epoxy or eutectic bonding. Ge-Au eutectic bonding is used here, since both the antenna and the bolometer are Ge. As does conductive epoxy, eutectic bonding introduces a dissimilar material (i.e., Au in this case) to the interface. Therefore, the epoxy and eutectic bonding create an interface between the bolometer and the antenna which will interfere with the phonons traveling to the antenna. Experimental results indicate that the eutectic bond creates an interface less obtrusive to the phonons than an epoxy created interface.[Wang, 1991, 103] The goal of this study was to optimize the eutectically bonded interface such that interfacial interference of the phonons is minimized.

The Au-Ge eutectic bonding method is attractive because it is a low temperature process. The eutectic temperature, T_e, of the Au-Ge system is 361°C while the melting points, T_m, of Au and Ge are 1064°C and 938°C, respectively.[Okamoto and Massalski, 1984, 75] Thus, annealing temperatures, which are about 50°C above T_e, are far below the T_m's of the materials. Since the diffusivity of Au is very small in Ge ($<10^{-15}$ m^2s^{-1} at 600°C), and the solubility of Au in Ge is very low (10^{15} cm^{-3} at 550°C), the phase separated Ge will be practically free of Au.[Almazouzi, et al., 1991, 1; Bracht, et al., 1991, 9] This significantly decreases the addition of impurities into the bulk material.

The approaches used to attain the best possible (i.e., most suitable) interface were two fold. First, the surfaces to be bonded were prepared such that intimate contact would be achieved. Chemomechanical polishing of the surfaces was performed to obtain optically flat surfaces. The polished surfaces were characterized by interferometry to optimize the technique.

The second step taken was to reduce the amount of Au introduced to the surfaces of the antenna and bolometer which were to be bonded. This was done by progressively decreasing the Au thickness used in the bonding process following each successful eutectic bond. Both structural and phonon transmission studies were carried out to determine the effect of the Au thickness on the interface.

The contents of this thesis describes the theory behind the processes used, the experimental procedures used, and the results obtained.

2. Ge-Au-Ge Interface Structural Studies

2.1. Theory

2.1.1. Equilibrium Ge-Au Phase Diagram

One of the most useful relationships between materials employed in materials science and engineering, especially in the field of materials growth, is the equilibrium phase diagram. An extensive amount of information can be deduced from these plots. An equilibrium phase diagram graphically depicts the phases of a material over a range of a thermodynamic extensive variable with respect to a thermodynamic intensive (or field) variable. A classic example is the equilibrium phase diagram of water shown over a range of volume (extensive) with respect to a range of temperature (intensive). In materials science and engineering, the materials of interest are primarily alloys, thus giving rise to binary, ternary, and quaternary equilibrium phase diagrams for two, three, or four constituent systems, respectively. In these cases, the extensive variable is typically the number of atoms given by mole fraction or atomic percent of each element present, while the intensive variable is temperature. Also, the constituents of the system can either be elements or compounds. Experimentally, the equilibrium phase diagram is determined by mixing specific ratios of constituents, bringing the mixture to a specific temperature, and quenching the mixture. The resulting phase structure of the material is shown on a temperature versus mole fraction or atomic weight percent diagram. Consequently, phases can extend over a wide temperature and composition range. The work in this thesis makes extensive use of the equilibrium phase diagrams of the Ge-Au binary system, hence a review of equilibrium phase diagrams is in order. More comprehensive evaluation of equilibrium phase diagrams can be found in Engineering Materials 2, authored by Ashby and Jones.[Ashby, 1986 #189]

In this thesis, the Ge-Au binary phase diagram shown in figure 2.1 is studied. Several aspects of the diagram should be pointed out which include variables associated with the abscissa (horizontal) and ordinate (vertical) axes, the solidus and liquidus curves, the phases and phase transitions, the melting points of Ge and Au, the eutectic point, and the result of quenching versus quasi-equilibrium cooling.

The abscissa axis shows the composition in atomic percent. From left to right, the abscissa axis displays the percentage of Ge from 0% to 100%, while from right to left the percentage of Au is given. Hence, at a value of 40% Ge, a 60% value of Au is present. The ordinate axis gives the temperature and is in units of °C.

The melting points of both Ge and Au are indicated as the largest temperature value intercepts on both the ordinate axes. Extending from the melting points are the liquidus and solidus curves. These curves represent the border between two phases and are where equilibrium occurs between the two phases. Crossing either curve, because of a change in temperature and/or composition, results in a phase transition. Crossing the liquidus curve produces a transition from liquid to solid plus liquid or vice versa. Similarly, traversing the solidus curve yields a phase transition from liquid plus solid to solid or the reverse. Because the curves represents an equilibrium coexistence between two phases, then crossing the curves gives rise to a nonequilibrium process. Hence, the phase transitions described above are nonequilibrium processes. The importance of this point will become apparent later.

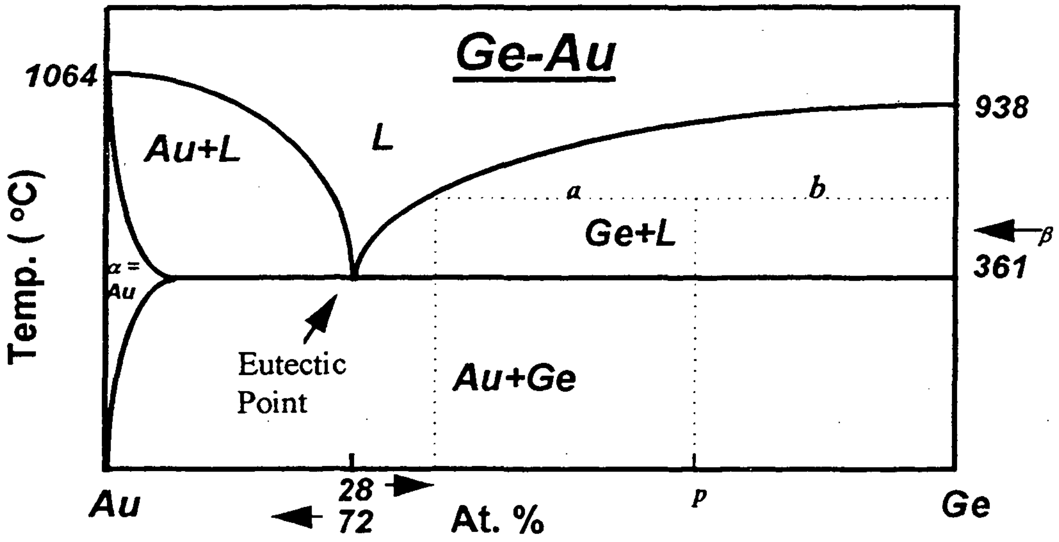

Figure 2.1: The Ge-Au Equilibrium Phase Diagram. The eutectic point depicts the point of composition and temperature where three phases exist in equilibrium.

A useful rule to use with equilibrium phase diagrams when determining the percentage of phases present for a given composition and temperature is called the *lever* *rule*. It is based on the requirement that matter is conserved. To illustrate the lever rule, observe the two phase region containing Ge and liquid at a composition *p* shown in figure 2.1, where ***a*** is the distance between the two vertical dashed lines, and ***b*** is the distance between the right most vertical dashed line and the left ordinate axis. The sum of *a* and *b* gives the distance *D*. The lever rule gives the atomic % fractions of each phase in a multi-phase region of the equilibrium phase diagram by using the following relations:

$$W_{phase1} = \frac{a}{D} \qquad [2.1a]$$

$$W_{phase2} = \frac{b}{D} \qquad [2.1b]$$

where W_{phase1} and W_{phase2} are the atomic percent fraction of phase one and two, respectively.

One of the main points of interest on a equilibrium phase diagram is the *eutectic point*. The eutectic point represents the composition and temperature at which three phases exist in equilibrium with each other. In a binary system, the eutectic reaction is given by:

$$L \rightarrow \alpha + \beta \qquad [2.2]$$

The symbols α and β represent solid Au and Ge phases, respectively, and L denotes the liquid phase. Although a certain percent composition of Au and Ge exists at the eutectic point, the phases in which the composition exists is given by the above equation. At the eutectic point, a specific composition of the two elements results in a melting point minimum much lower than the respective melting points of the elements. The *lever rule* applies at the eutectic point. For the Ge-Au binary system, the eutectic occurs at a composition of 28% Ge and 72% Au. Ge, given as β in binary systems, is a line phase at the eutectic temperature. The liquid composition is the eutectic composition (28% Ge, 72% Au). The composition of α is given by the point at which the isothermal line extending to the left from the eutectic point intersects the Au solidus. The third phase is 100% Ge since the isothermal line intersects with the right most ordinate axis. Here, Ge is a line phase (i.e., vertical line representing a phase) which signifies that the solubility of Au in Ge is very small as previously mentioned. The implication of this last fact and the low melting point of the solid eutectic composition are very important for this study.

2.1.2. Diffusion Couple: General Binary System

In order to understand eutectic epitaxial growth, comprehension of a *diffusion couple* (i.e., 2 pure materials joined together) through the use of an equilibrium phase diagram is beneficial. A diffusion couple is usually described in the solid phase, whereas eutectic epitaxial growth occurs when both liquid and solid phases are present. However, by reversing the process of a diffusion couple, epitaxial growth may be described. A diffusion couple is made by placing two pure solid materials together, material A and material B. Diffusion occurs across the interface A/B (note that / means interface) as shown in figure 2.2. The driving force for diffusion is the minimization of the diffusion couples' free energy (i.e., Gibb's free energy here). As soon as diffusion occurs, a variety of binary phases can form. When the minimum free energy of the diffusion couple is reached, equilibrium phases are formed. Since diffusion is a function of the free energy and the equilibrium phase diagram is a result of free energy minimization, then the diffusivities of the pure substances and the equilibrium phase diagram of the 2 materials are essential to determine the type and number of phases at a specific temperature.[Porter and Easterling, 1981, 81]

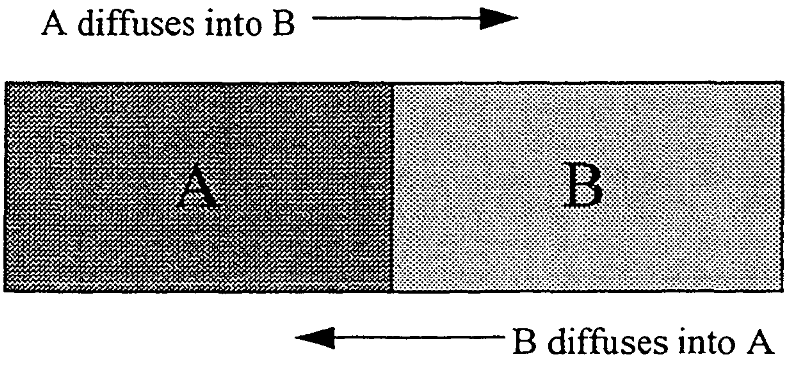

Figure 2.2: A diffusion couple of material A and material B

If the diffusivity (i.e., diffusion coefficient) of the two materials are of the same

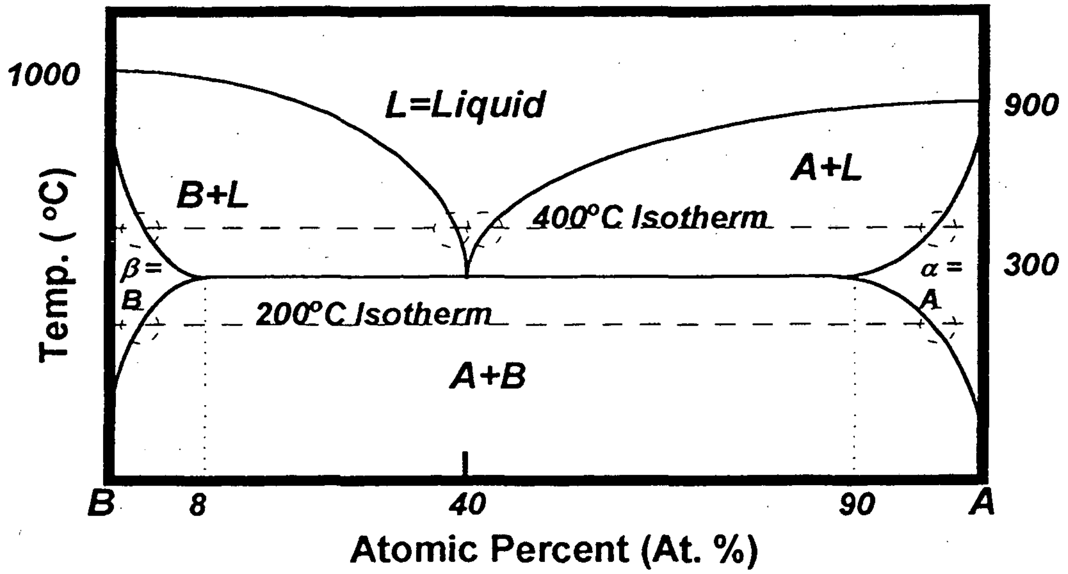

Figure 2.3: Equilibrium Phase Diagram of a general binary system.

order, the rates of diffusion of the first material into the second material matrix will be similar to the diffusion of the second material in the first material matrix. If the diffusivities are not of the same order, the material with the higher diffusivity may be the determining factor in phase formations.

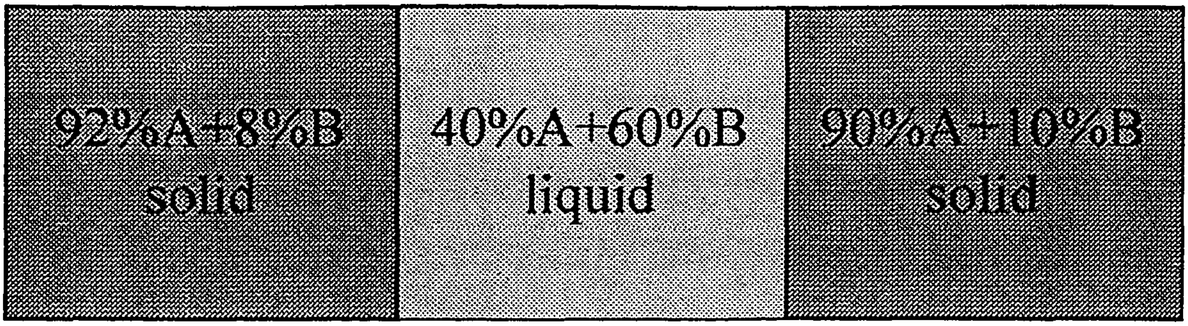

Figure 2.4: A diffusion couple of the A-B binary system at an equilibrium eutectic temperature. That is, diffusion has ceased because the equilibrium compositions of the three phases have been reached.

The equilibrium phase diagram gives a first order approximation of which phases will form within a diffusion couple. At a specific temperature consider the equilibrium phase diagram of a fictitious binary system containing the constituents A and B shown in figure 2.3. Joining A (i.e., α) and B (i.e., β) at 200°C, 100°C below the eutectic temperature, diffusion will occur until equilibrium is attained or until either A or B are depleted. The intersections of the 200°C isotherm with the α and β solidus gives the equilibrium conditions and compositions of the two phases. The intersection occurring near the A ordinate axis gives a phase composition consisting of about 5% B in pure A while the other intersection near the B ordinate axis shows a composition consisting of about 3% A in pure B.

At the eutectic temperature (here 300°C), a diffusion couple reaching equilibrium will have three phases present. As described earlier in section 2.1.1, the intersection of the eutectic isotherm with the solidus gives the compositions of two solid phases while the liquid composition is given by the eutectic point itself. As shown in figures 2.3 and 2.4, the composition of the phases is 10% A in B, 8% B in A, and the eutectic phase consists of 40% A and 60% B.

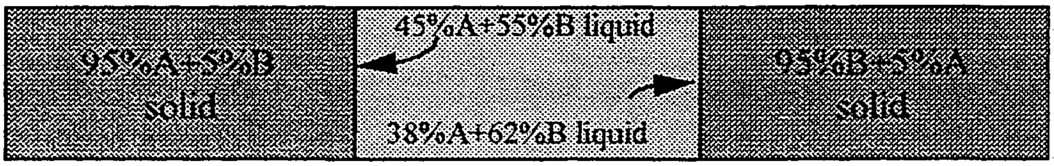

Figure 2.5: An A-B diffusion couple following diffusion and at a temperature above the eutectic temperature but below the melting point of both constituents A and B.

A third temperature range of interest is above the eutectic temperature but below the melting points of the A and B constituents. This is exemplified by the 400°C segmented isotherm in figure 2.3. Notice that, along the 400°C segmented isotherm, there are four dashed-circled intersections: two intersections with liquidus curves and two with solidus curves. This means that, for an A-B diffusion couple in which diffusion has ceased and thus equilibrium has been attained, there are two interfaces. At each interface two phases exist in equilibrium. The phases consist of both liquid and solid components. These phases are shown in the diffusion couple in figure 2.5 below. The liquid and solid compositions of the two phases at the right interface are given by the two left circled intersections. The liquid component at the interface contains about 38% A and 62% B while the solid component contains about 5% A in a B matrix. The compositions of the liquid and solid components at the left interface are given by the right most dashed-circled intersections along the 400 °C isotherm. The intersection of the liquidus gives a liquid composition at the interface of about 45%A and 55%B whereas the solidus intersection shows a 5%B in an A matrix solid composition. Note that a composition gradient exists in the liquid between the two interfaces, whereas the composition in each solid is homogeneous.

2.1.3. Diffusion Couple: Ge-Au Binary System

Solidification and epitaxial growth are predominant mechanisms in Ge-Au-Ge eutectic bonding. Their explanation is facilitated through the use of a diffusion couple. Therefore, the Ge and Au diffusion couple is discussed in this section. When Au and Ge are placed together to form a diffusion couple, diffusion will occur. The diffusivity (diffusion coefficient), of Au in Ge, D_{Au}, is 2.2×10^{-11} cm^2/s at 596°C.[Almazouzi, et al., 1991, 1; Bracht, et al., 1991, 9] Conversely, the diffusivity of Ge in Au, D_{Ge}, is 7.3×10^{-2} cm^2/s between 737°C and 1014°C.[Neumann, 1990, 66] The diffusivity of an element in the liquid phase is on the order of 10^{-5} cm^2/s. Hence, the diffusion of Ge in Au is several orders of magnitude faster than the self-diffusion of an element in the liquid phase. The diffusion of Ge through a thin film (~ 2000 Å) of Au has been seen.[Chang, 1983, 14] Since $D_{Ge} \gg D_{Au}$ and the diffusion of Ge through Au has been seen, the strongly supported assumption is made here that the only solid phase diffusion occurring is Ge in Au.

A first order approximation to which phases will form is given by the equilibrium phase diagram. Consider a temperature below the eutectic temperature in the Ge-Au equilibrium phase diagram (figure 2.6), say 300 °C. In order to more easily describe the diffusion couple, imagine a line drawn from one ordinate axis to the other at the chosen temperature. This line is the 300 °C isotherm. Beginning with pure Au, located on the left side of the equilibrium phase diagram, travel along the 300 °C isotherm. Diffusion of Ge into Au occurs along the isotherm until the Au acquires the equilibrium amount of Ge. That is, once the isotherm reaches the equilibrium phase boundary, then the Au Au/Ge interface is at equilibrium and diffusion of Ge into Au will cease. The equilibrium composition of Ge in Au is 1 atomic percent (at. %). The intercept of the isotherm with the right ordinate axis (on the Ge pure side) indicates that Ge remains essentially Au free. This is seen by extrapolating the data of Almazouzi *et al.* to 300 °C which gives a Au concentration in Ge of 5.27×10^{10} cm^{-3}.[Almazouzi, et al., 1991, 1] Thus, when a Au and Ge couple is formed, equilibrium will be reached only when the maximum solubility of Ge in Au is attained and the Ge will remain Au free. If the volume of Ge is more than Au (i.e., more accurately, $Ge_{atoms} >> Au_{atoms}$) as is the case in the experiments performed for this thesis, then the only interface that will exist in equilibrium at 300 °C is between the

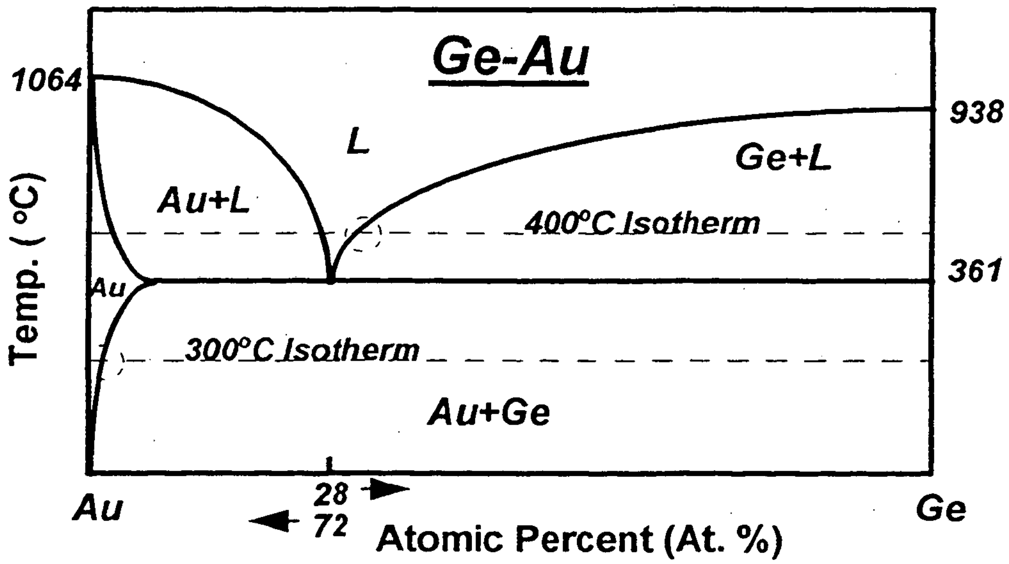

Figure 2.6: The Ge-Au equilibrium phase diagram showing the 300°C and 400°C isotherms.

two resulting phases: Ge and Au:1 at. % Ge alloy.

Based on the above, the process of forming a eutectic composition from a diffusion couple can now be discussed. At the Ge and Au eutectic temperature of 361°C and the condition $Ge_{atoms} >> Au_{atoms}$, the resulting phases are the same as described in the preceding paragraph with the addition of a liquid phase. From the equilibrium phase diagram, the maximum solid solubility of Ge in Au is about 3 at. %, and according to Almazouzi *et al.*, the Ge will contain a maximum of 9.97×10^{12} cm^{-3} of Au.[Almazouzi, et al., 1991, 1] If this value is exceeded, a phase transformation occurs resulting in a 28 at. % Ge and 78 at. % Au liquid phase called the eutectic liquid phase. Hence an interface will exist between Au free Ge and an alloy of Au containing 3 at. % Ge and an interface between the Au alloy with 3 at. % Ge and eutectic liquid phase.

As the temperature rises above the eutectic temperature, all the Au will be consumed assuming the Ge is a quasi-infinite source. Since solid Au no longer exists, the equilibrium of the system is only shown by the intersection of the isotherm and Ge liquidus. Above the eutectic temperature, say at 400°C, the diffusion couple at thermal equilibrium is a two phase system: Ge + L.

2.1.4 Eutectic Solidification and Epitaxial Growth of the Ge-Au Binary System

Eutectic epitaxial growth of Ge-Au is a major theme of this thesis. Since eutectic epitaxial growth is a form of solidification, eutectic solidification should be examined. There are two types of eutectic solidification and they are usually classified as *normal* and *anomalous*. Normal eutectic solidification occurs when the simultaneous growth of both phases progresses as a planar solid/liquid interface. The structure of the solid phases is either *lamellae* or *rod-like*. The lamellae eutectic structure appears as alternating planes either *lamellae* or *rod-like*. The lamellae eutectic structure appears as alternating planes of phases where the planes are parallel to the growth direction. The rod-like eutectic structure consists of rods of the minor phase parallel to the growth direction embedded in the major phase. The normal eutectic microstructures of lamellae and rod-like are both continuous microstructures where, from the beginning to the end of crystallization, the phases can be traced along an unbroken path.

Anomalous structures are produced when one phase facets (e.g., highly orientated) occurs during growth indicating a high entropy of melting.[Porter and Easterling, 1981, 81] Anomalous eutectic solidification results in discontinuous microstructure. Discontinuous microstructures are either discontinuous lamellae or rod-like structures or the microstructure consists of one phase dispersed as discrete particles in the matrix phase.[Tiller, 1991, 97]

The type of microstructure depends heavily on the cooling rate and the amount of the two constituents present in the binary system during solidification.[Hellawel, 1970, 30] The cooling rate dictates the amount of diffusion occurring during solidification. Generally, eutectic solidification consists of rapidly cooling a liquid whose initial composition is eutectic. The cooling rate used in this study is slow enough that the system is considered to be in quasi-equilibrium, hence only slow solidification of the eutectic processes will be discussed. It is in this realm of cooling rate that epitaxial growth is prevalent.

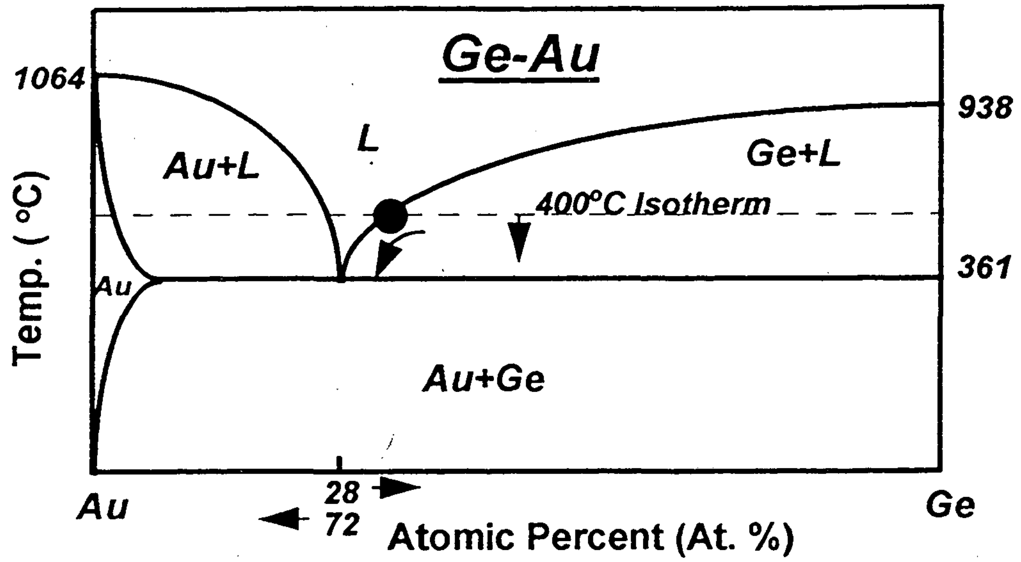

Figure 2.7: The Ge-Au equilibrium phase diagram depicting the case where a quasi-infinite amount of Ge and a finite amount of Au exists. Thus, all the Au is in the liquid phase and only the Ge liquidus has meaning.

Although eutectic solidification is not an equilibrium but a kinetic process, the equilibrium phase diagram can still be used as a guide to the mechanism of eutectic solidification. Thus, Ge-Au eutectic solidification is explained in terms of the equilibrium phase diagram. The general eutectic solidification case will not be examined here. Rather, consider the special case where the amount of Ge is much greater than the amount of Au. Hence, at a temperature above the eutectic point, solid Ge readily exists, but the solid Au has been consumed into the liquid alloy. During the slow cooling process, the temperature of the solid is considered cooler than the liquid so a thermal gradient exists. Because the liquid Ge-Au alloy (hereafter just liquid) and solid Ge phases coexist, assume that the solid/liquid interface is in equilibrium.

The physical picture of this present case is shown in figure 2.7. In essence, it is the diffusion couple explained in the latter part of section 2.1.3. By reversing the explanation of the diffusion couple, solidification is described. Assuming quasi-equilibrium cooling, the composition of the liquid at the solid/liquid interface follows downward along the Ge liquidus curve as depicted by the arrow in figure 2.7. Since the temperature of the solid/liquid interface decreases and Ge supersaturation occurs, this promotes interfacial solidification. At the eutectic temperature, the phase transformation given by equation 2.1 takes place resulting in the simultaneous creation of three phases: Au_s:3 at.% Ge, Ge_s, and liquid consisting of 28 at.% Ge and 78 at. % Au (s = solid). Furthermore, if the cooling rate is slow, epitaxial growth occurs.

A similar method of eutectic epitaxial growth was first performed as early as 1964 by Wagner and Ellis, and subsequently by others, using Si and Au.[Chang and Ottaviani, 1984, 15; Chang, et al., 1988, 16; Wagner and Ellis, 1964, 102; Wilk, et al., 1994, 108] The equilibrium phase diagram shows the same eutectic configuration as the Ge-Au system with a eutectic temperature and composition of 363°C and 18% Si and 82% Au, respectively. The approach of Wagner and Ellis was to deposit Au on to a silicon substrate, heat it to 950°C, and hold it at that temperature. Rather than decreasing the temperature to promote growth, they added Si to the melt thereby supersaturating the solution. The excess Si in the liquid promoted epitaxial growth of Si out of the liquid and onto the Si at the liquid/solid interface (i.e., homoepitaxial growth) while the Au remained in solution. Using a similar technique, where 1μm to 5μm of Au was deposited on Si, annealed at 400°C, and cooled at various cooling rates, Philofsky *et al.* found that, at cooling rates less than 10^3°C/s, epitaxial growth occurred.[Philofsky, et al., 1972, 77] Au also nucleated within the liquid for cooling rates between 10^3°C/s and 5°C/s. For cooling rates below 5°C/s, Au nucleated onto the epitaxially grown Si. They postulated that Si from the melt nucleated at the silicon substrate and grew towards the surface in the direction of heat flow, because a thermal gradient existed.

This form of homoepitiaxial growth, also known as *liquid-metal mediated* homoepitaxial growth and *surfactant epitaxial growth*, has been investigated by Xiong *et al.* using Ge and Au.[Iwanari and Takayanagi, 1992, 38; Iwanari and Takayanagi, 1992, 39; Xiong, et al., 1991, 110] As did Wagner and Ellis, Xiong *et al.* deposited Au on a heated substrate (400°C) and a eutectic solution immediately formed. Keeping the temperature constant, they deposited Ge using a slow deposition rate. As in the Si case, the addition of Ge supersaturated the liquid alloy causing epitaxial growth of Ge at the solid/liquid interface. After deposition was terminated, the sample was kept at the growth temperature for 20 minutes, then slowly cooled. The resulting structure showed further homoepitaxial growth and the formation of Au layers and Au agglomerations Xiong *et al.* called *islands*. Furthermore, the Au precipitates were both crystalline and faceted indicating anomalous eutectic solidification with heteroepitaxial growth.

2.1.5 Ge-Au-Ge Eutectic Epitaxial Bonding

Previous studies covering eutectic or near eutectic bonding are prevalent.[Bernstein, 1966, 7; Li, et al., 1984, 50; MacDonald and Eagar, 1992, 53; Nolder and Malone, 1987, 68; Tuah-Poku, et al., 1988, 98; Yost, 1974, 111] Yet, studies concerning eutectic epitaxial bonding are limited in number thereby increasing the difficulty of explaining the process.[Cros and Canella, 1991, 17; Dubey, et al., 1994, 19] However, because in this study Ge is bonded to Ge, the explanation is simplified. One manner in which to conceptualize eutectic bonding of equivalent material is to both reverse, as was done in the previously section, and somewhat change the diffusion couple mechanism.

Consider the case described in the preceding section where the abundance of one constituent is much greater than the other. Thus, at or above the eutectic temperature, the constituent of less abundance is consumed while the other still exists in the solid form. In the context of this study, assume the abundant material is Ge and the consumed material is Au as was explained in the case investigated by Xiong *et al.* Additionally, rather than on one side, let the liquid be constrained or bordered on either side by Ge. Above the eutectic temperature, the diffusion couple now resembles figure 2.5, but both solids are Ge without Au. Furthermore, the liquid's composition at the solid/liquid interface is given by the intersection of the liquidus and isotherm. Using the results of Wagner *et al.* and Xiong *et al.* and the equilibrium phase diagram, quasi-equilibrium cooling through the eutectic temperature resulting in Ge-Au epitaxial bonding is explained.

As the system is cooled from above the eutectic temperature, the composition of the liquid will follow the Ge liquidus line of the Ge-Au equilibrium phase diagram. As depicted in equilibrium phase diagram of figure 2.7, the drop in temperature causes a decrease in Ge concentration and an increase in Au concentration. Xiong *et al.* stipulated that the decrease in Ge concentration was attributed to the epitaxial nucleation of Ge if a thermal gradient existed across the liquid solid interface (here, the solid is cooler than the liquid). Nucleation will occur at both solid/liquid interfaces as long as this thermal gradient exists. Such a thermal gradient is present if, for instance, this particular diffusion couple configuration is cooled radially. The use of a clamshell furnace will give rise to radial cooling. Cooling to just prior to the eutectic temperature, the liquid consists of slightly less than 72 at. % Au and slightly greater than 28 at. % Ge. As the eutectic temperature is reached, spontaneous solidification of 28 at. % Ge and 72 at. % Au liquid results in a two phase system containing solid Ge and solid Au containing 3 at. % Ge alloy. As depicted by the phase diagram, solidification at the eutectic temperature causes a discontinuous change in composition. In other words, this is a second order phase transformation.

The volume, from the liquid to solid phases, also changes. In the pure state, Ge undergoes a volume expansion.[Hansen and Haller, 1992, 28] Since the density of Au increases upon solidification, the volume is assumed to decrease since density is the inverse of a normalized volume.[Brandes and Brook, 1992, 10] Linear relationships (i.e., equations) are used successfully to treat changes in density, viscosity, and surface tension of elementally pure liquids, so it is also assumed that this is the case for volume changes in pure and binary liquids.[Brandes and Brook, 1992, 10] Such a linear relationship, called

Vegard's law, exists for the changes in lattice constant with varying composition.[Barrett and Massalski, 1980, 5] For volume changes in solid cubic materials, the linear dependence remains. The form of Vegard's law is:

$$X_1V_1 + X_2V_2 = V_{total} \qquad [2.2]$$

where X_1 and X_2 and V_1 and V_2 are the compositions and volumes of the constituents in the liquid, respectively. Whether this simple relation can also be applied to binary liquid phases is not known.

The spontaneity of the transformation at the eutectic point is analogous to rapid solidification, which occurs for extremely fast cooling rates. In the similar system of Si-Au, Philofsky *et al.* showed that rapid cooling rates hinder or terminate epitaxial growth. This suggests that epitaxial bonding cannot occur. Yet, the results of Xiong *et al.* imply that epitaxial bonding can occur. Furthermore, Cros and Canella have shown that Si-Au epitaxial bonding is possible.[Cros and Canella, 1991, 17] The equilibrium phase diagram illustrates the existence of a spontaneous phase transformation at the eutectic temperature. However, epitaxial growth is not an equilibrium process which requires a deviation from the equilibrium phase diagram to explain why crystalline rather than amorphous Au and Ge form at the eutectic temperature. A possible explanation is that the transformation at the eutectic temperature is not spontaneous.

2.2 Experimental Procedure

2.2.1 Introduction

The experimental procedure is schematically shown in figure 2.8. Several aspects of the experimental procedure were critical in order to attain an epitaxial interface during solidification. As pointed out previously, they include proper crystallographic orientation during the mounting (shown in figure 2.8c) prior to annealing. Also, surface flatness and cleanliness were paramount and, as indicated in figure 2.8d, a slow cooling rate was essential to achieve interfacial epitaxial growth. All of these processes are described in the sections to follow.

2.2.2 (100) Ge Wafer Cutting and Orientation

In this study, a Czochralski grown (100) Ge crystal with a net carrier concentration of ~10^{12} cm^{-3} was used. The low dislocation density (100) Ge ingot was mounted on and adhered to (using Do All cement) a graphite block. Two adjacent 1.4 mm thick, 3.5 cm diameter (100) Ge wafers were cut with a Silicon Technology Corporation inside diameter (ID) diamond saw (see figure 2.9a). With the Ge wafers still attached to the graphite block, several notches were scribed into the edge of the wafers

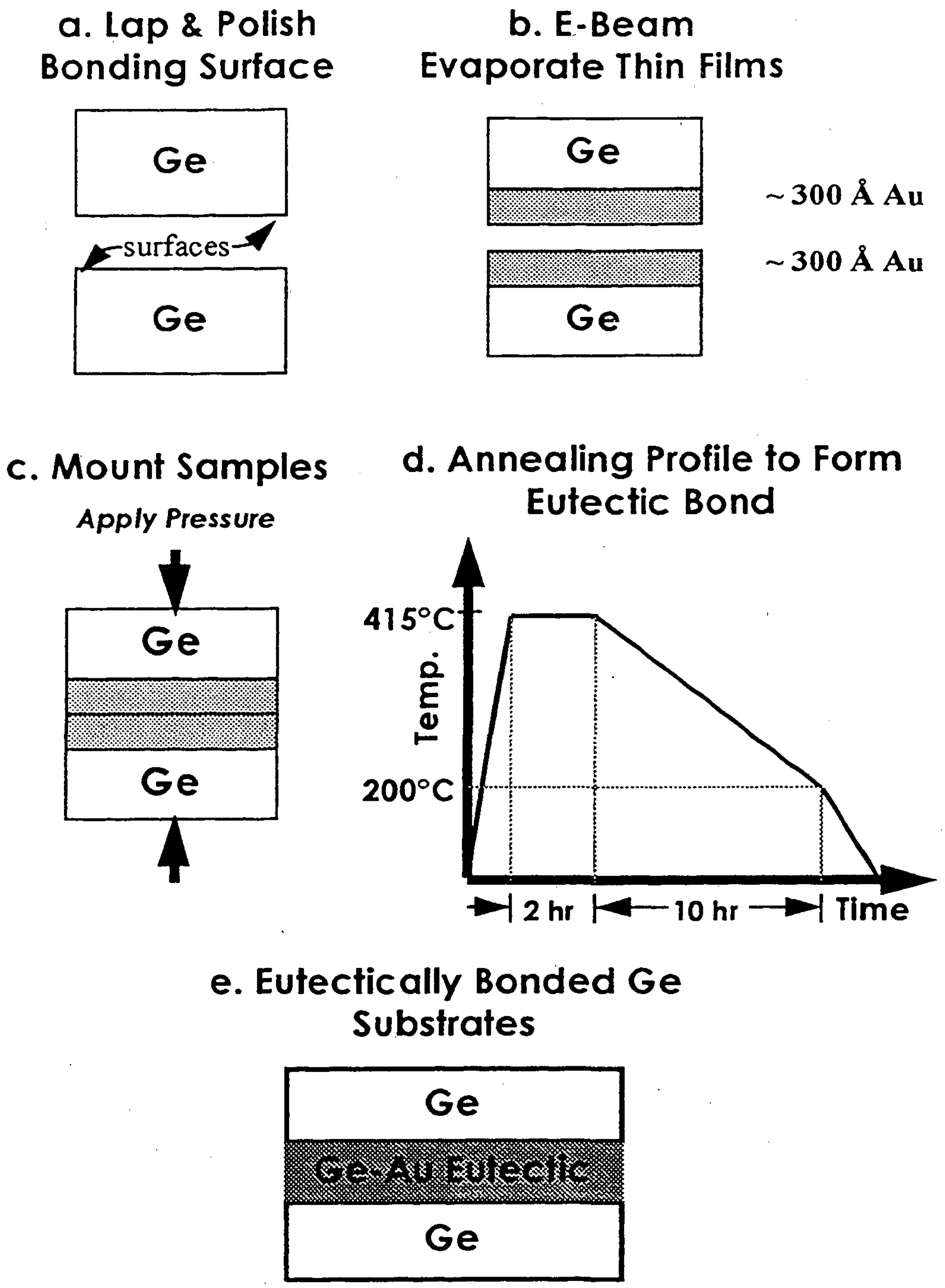

Figure 2.8: The sample preparation and experimental procedure for eutectically bonding two Ge bonding pairs.

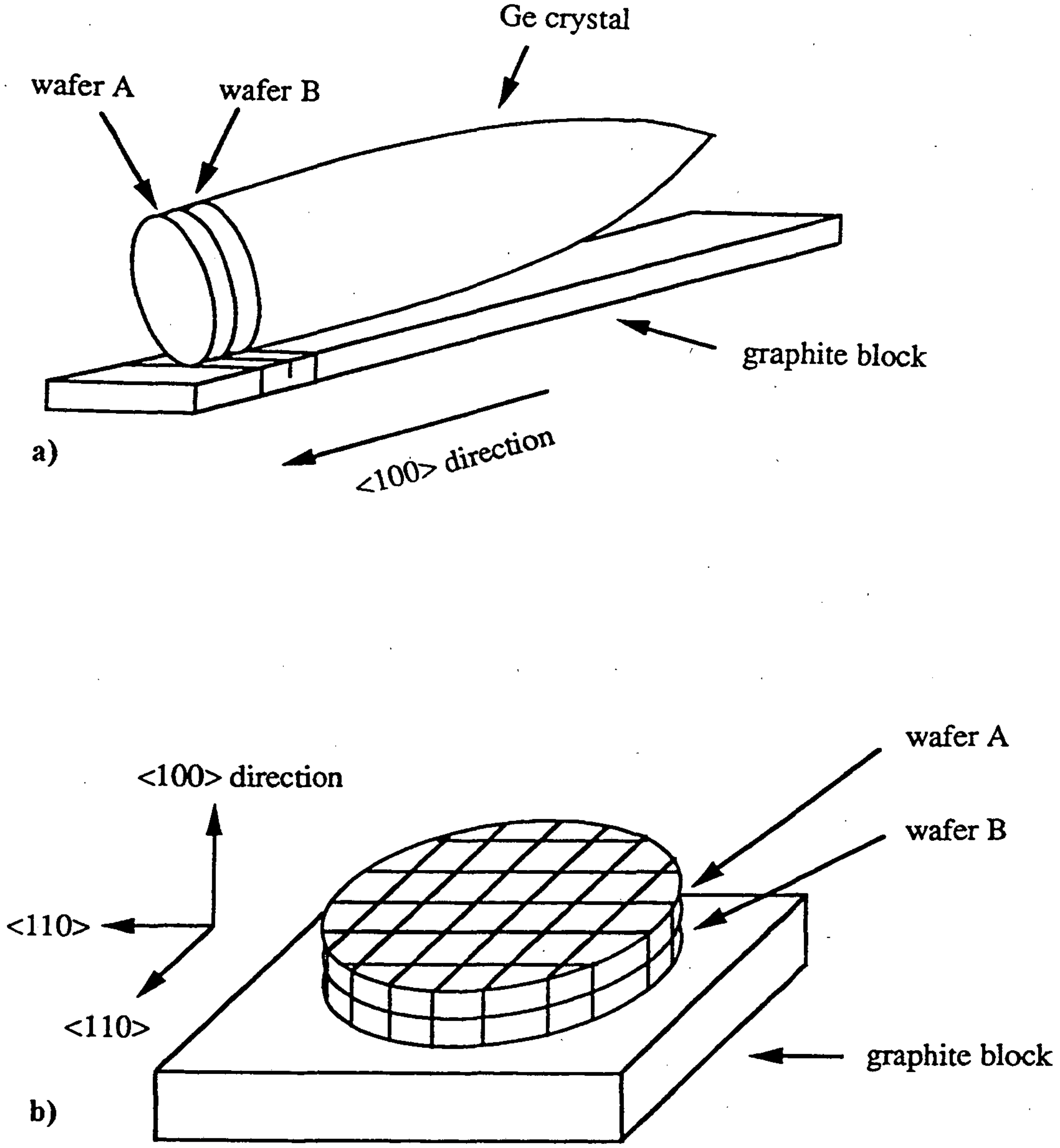

Figure 2.9: **a)** (100) Ge wafers cut from graphite mounted Czochralski grown Ge ingot. **b)**: (100) Ge wafers mounted and diced into bonding pairs.

with a SiC scribe. This was done to retain the orientation of the wafers while they were lapped and optically polished (described in the following section). The polished surfaces of the wafers were placed together and the notches were aligned. In this configuration, the wafers were mounted on a graphite block and cut using a pneumatically and hydraulically controlled dicing saw producing 3x4 mm^2 rectangular bonding pairs (see figure 2.9b).

2.2.3 Lapping and Chemomechanical Optical Polishing

Equally as important as orientation, intimate contact between the two 1.4 mm thick 3x4 mm^2 (100) Ge bonding pairs was required to obtain epitaxial growth through the interface. An atomically flat and smooth surface morphology was necessary to achieve intimate contact between the bonding pair surfaces. Lapping and optical polishing of the bonding pair surfaces was performed to attain flat and smooth surface morphology. That is, each wafer was individually lapped and polished. Lapping is the removal of material from the surface via abrasive particles. Chemomechanical polishing (optical polishing) is the removal of surface layers by the interaction of surface atoms with a colloid and friction by a polishing cloth.

The lapping block on which the Ge crystals were attached during lapping and polishing also required an atomically flat mounting surface. For this reason, the lapping block was lapped and polished prior to lapping and polishing of the Ge crystals. The lapping block, which is a stainless steel cylinder 4 inches (102 mm) in diameter and 1.5

inches (38 mm) in height, was lapped by the optics shop at Lawrence Berkeley Laboratory (LBL). Spherometer measurements of the lapping block mounting surface indicated the height differential of the surface to be less than 1/10,000th of an inch (2.54×10^{-6} m) when measured 2 inches (5.08×10^{-2} m) radially from the center, and 1/500th of an inch (5.08×10^{5} m) when measured 2 inches (5.08×10^{-2} m) tangent from the edge. Interferomic measurements of the lapping block mounting surface are discussed later.

The optimized lapping procedure is as follows. The lapping block was heated on a hot plate to approximately 100°C. Wax was used to attached the Ge wafer to the lapping block. At this temperature, the wax melted as it was applied to the lapping block. The excess wax was wiped off so that a thin film was left on the block. The Ge wafer to be lapped was placed in the center of the lapping block. Eight to nine 1.4 mm thick pieces of polycrystalline stock Ge, called *spacers*, were placed around the wafer and on the outer edge of the lapping block as close together as possible. This assures uniform lapping of the Ge wafer and minimizes oscillations of the lapping block caused by surface unevenness of the Ge wafer. The lapping block, spacers, and Ge wafer configuration are shown in figure 2.10.

The above configuration was lapped on a "Lap Master 500" polishing apparatus shown in figure 2.11. The lap master consists of a rotating lapping "stone" (similar to a whetstone), three lapping block holders, an oil reservoir, a peristaltic pump, and an oil feed line. The lapping block was placed in the lapping block holder (figure 2.11) with the Ge wafer facing down onto the lapping stone. As the lapping stone turns (rate ~ 20 RPM), a solution consisting of 250 mL of #9 (9 μm) Al_2O_3 grit per 2 L of Pella oil was dripped onto the lapping stone at a rate of about 4 mL/min. The wafer and

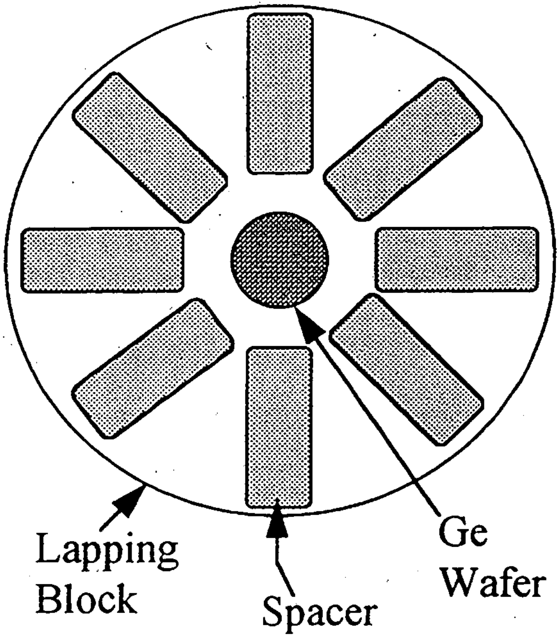

Figure 2.10: Lapping Block with (100) Ge Wafer and polycrystalline Ge spacers.

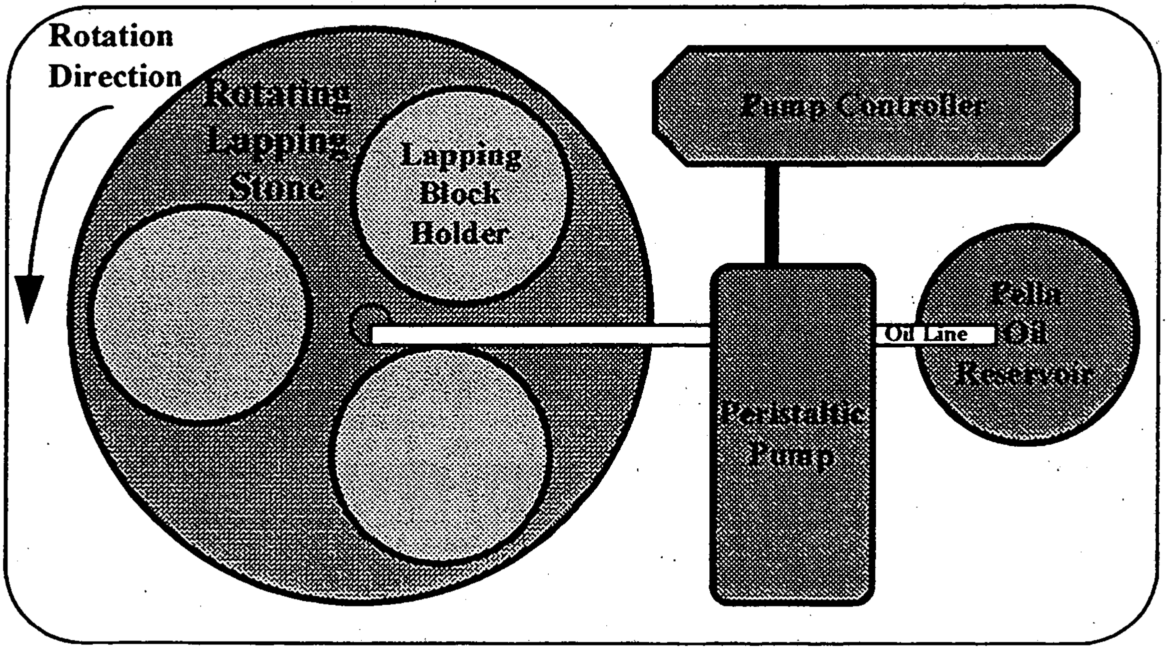

Figure 2.11: The lapping apparatus - Lapmaster 500.

the spacer's surfaces were entirely lapped. Approximately 150 μm of Ge was removed during this process. Following lapping, the Pella oil solution was cleaned from the lapped surfaces and block using a strong laboratory soap and blown dry with N_2 gas. The lapping block was placed on the hot plate and the wafer and spacers were removed. The Ge wafer and spacers were cleaned by boiling them for three minutes in 1,1,1-trichloroethane, then acetone, and finally methanol and finally were blown dry with N_2 gas. The excess wax was wiped from the lapping block and a new film of wax was applied to its surface. The cleaned wafers and spacers were attached, lapped side down, to the lapping block. They were lapped again on the opposite side until all surfaces were uniformly lapped. Periodically, throughout the process, the wafer thickness was measured with a surface micrometer. From this data, the lapping rate was calculated to be about 3 μm/min. The data is plotted in figure 2.12. At this stage, the wafer was about 1.25 mm thick. The surfaces were then thoroughly cleaned with a strong laboratory soap and blown dry with N_2 gas.

It should be noted that several different Al_2O_3 grit sizes in the lapping solution were initially investigated. They included 250 mL of either 3μm Al_2O_3 grit, #9 (9 μm) Al_2O_3 grit, or #12 (12 μm) Al_2O_3 grit in 2L of Pella Oil. Both the 12μm Al_2O_3 grit and 3μm Al_2O_3 grit left numerous large, deep (at least 5 μm) scratches in the lapped surface and thus were not used for lapping. However, the 9 μm Al_2O_3 grit in Pella oil solution did not produce any scratches. For this reason, the 9 μm Al_2O_3 grit Pella oil was used for lapping.

Once lapping was completed, the 1.1 μm thick Ge wafer was ready to be polished. The polishing cloth on the Chemical-Mechanical Polisher (see figure 2.13) was scrubbed

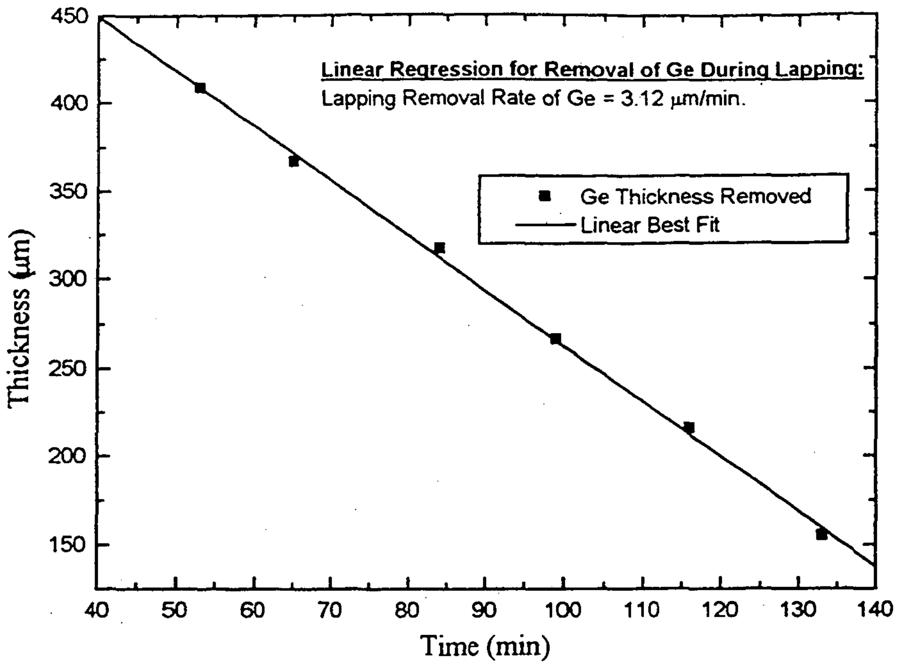

Figure 2.12: A plot of Ge wafer thickness versus lapping time to determine the lapping rate of Ge.

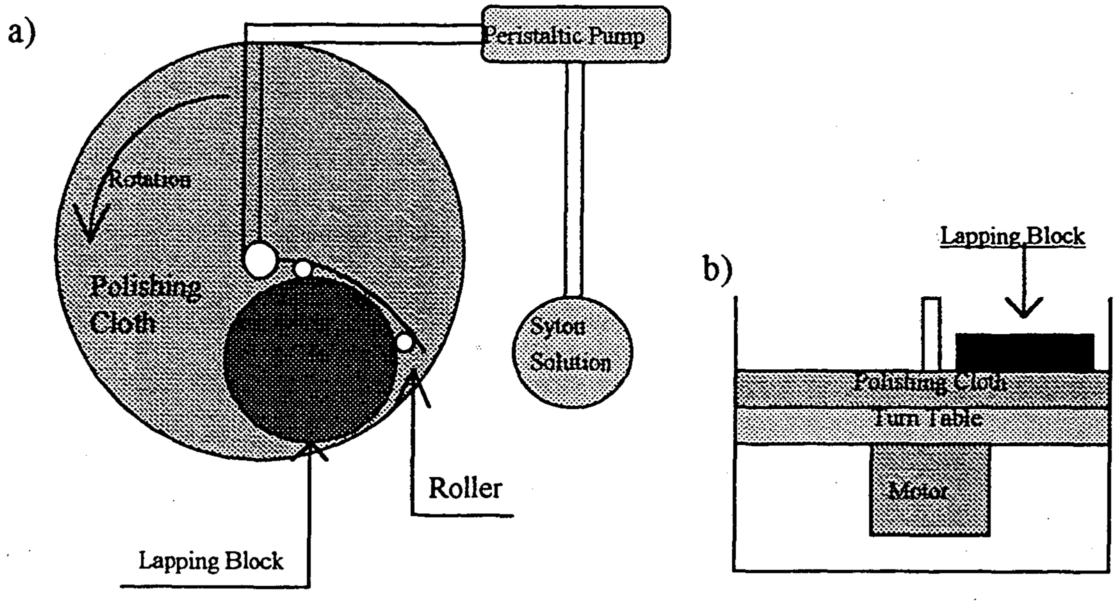

Figure 2.13: Chemomechanical polisher. **a)** Top view. **b)** Side view.

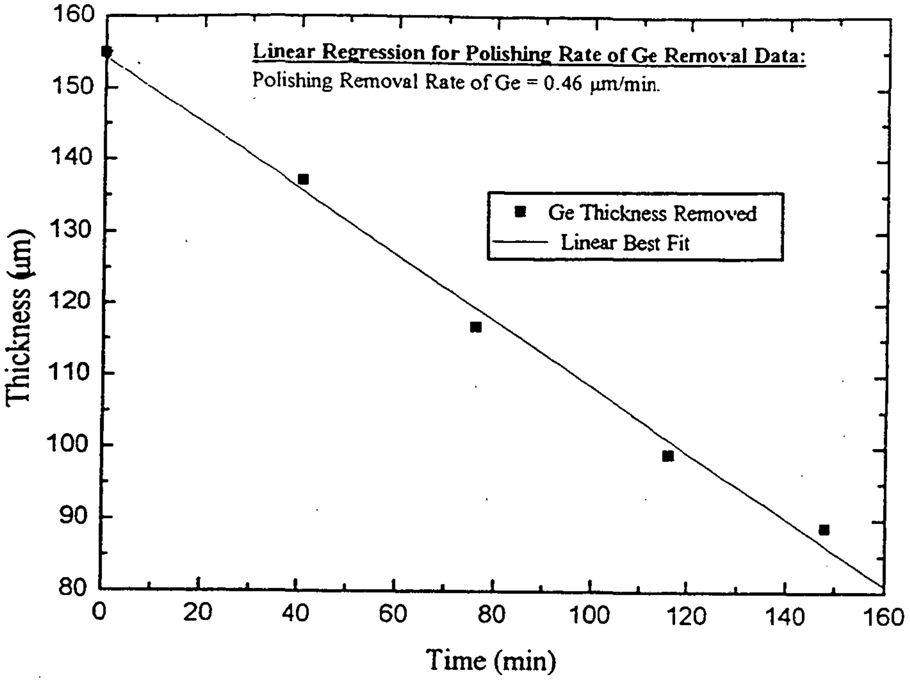

Figure 2.14: Ge removal rate during chemomechanical polishing.

clean with de-ionized water and saturated with the Syton® solution. A 7:3:1 solution of de-ionized water, Syton (an aqueous SiO_2 colloidal suspension made by Dupont), and H_2O_2 (30 wt. %) was prepared. The mechanism for chemomechanical polishing of Ge with this solution begins with the removal of GeO_2 by H_2O_2. The polishing cloth moves the hydroxide (OH^-) anions to the Ge surface. The OH^- reacts with the Ge forming surface hydroxyl groups which are removed frictionally by the Si colloid.[Pietsch, et al., 1994, 78] The lapping block was placed wafer-side down onto the cloth. The motor of the chemomechanical polisher was set to rotate at about 180 RPM while Syton solution was dripped onto the pad at a rate of 3.3 mL/min. At 180 RPM, the Ge was removed at a rate of about 0.46 µm/min (see figure 2.14). When polishing was completed on one side, the wafer was approximately 1 mm thick. The lapping block was placed on a hot plate and the wafer and spacers were removed. Cleaning the wafer and spacers was done using the same solvents and procedure as when lapping. If polishing was required on the opposite side of the wafer, then the newly polished side of the wafer was protected from the lapping block surface with aluminized mica. The mica, cut to the dimensions of the wafer, was quite thin (about 6 µm) and caused problems only when air pockets formed between it and the lapping block.

2.2.4 Pre-Metallization Sample Preparation

To eliminate organic surface contaminants, the crystals were immersed in boiling trichloroethane (TCA), then in boiling acetone, and finally in boiling methanol for 3 minutes respectively. In order to eliminate any oxide layers, the Ge crystals were placed in a 50:1 solution of H_2O:HF (i.e., 1% HF solution) and vigorously agitated for approximately 3 to 10 minutes. When the crystals were retrieved from the solution, and if they were thoroughly cleaned, the Ge bonds on the surface were hydrogen terminated and the HF solution formed tight beads and rolled off as the crystal was tilted.

2.2.5 Metallization

Thin films of Pd and Au were electron beam deposited on the polished surface of the two rectangular Ge samples. The Pd film was 10% the thickness of the Au film and was used to eliminate residual oxides and to decrease the surface tension of the Au on Ge during Au deposition.

Following the pre-metallization procedure, the bonding pairs were immediately placed in the Electron Beam (E-Beam) Deposition sample holder which was specifically designed to hold the bonding pairs. The holder was secured into the sample receptacle of an Airco Temescal E-Beam evaporator equipped with a Leybold 450 (450 liters/min. pumping capacity) backed by a Welch Duo-Seal vacuum roughing pump. The E-Beam sample receptacle is water cooled to prevent heating of the bonding pairs. The main chamber was pumped down to at least 5×10^{-6} Torr, and Pd (~30Å-50Å) then Au (~300Å-900Å) were deposited onto the crystals at room temperature. The deposition rate was about 5 Å per second. A Veeco quartz crystal transducer measured the thickness of the thin films.

2.2.6 Eutectic Bonding

After the main chamber of the E-Beam was brought to atmospheric pressure, the crystals were removed and placed into yet another custom machined sample holder with two Pd/Au thin films face to face (figure 2.8c). The eutectic bonding apparatus was equipped with a spring loaded plunger which was placed on top of the sandwiched crystals. In this arrangement, the plunger firmly held the two crystals together. The pressure exerted by the plunger onto the sandwiched bonding pairs was approximately 3.6×10^6 Pa. The eutectic bonding apparatus with the samples was slid into a clamshell annealing furnace which was purged with N_2 for 15 minutes. To obtain the annealing profile shown in figure 2.8d, the furnace's temperature controller was programmed so the furnace ramped up to 415°C and held at that temperature for two hours, then ramped down over 10 hr to 200°C with a cooling rate was about 22°C/hr. The slow cooling rate kept the system in quasi-equilibrium thus promoting epitaxial growth. After removing the eutectically bonded sample from the eutectic bonding apparatus, the integrity of the bond was tested through the application of a shear force. If the eutectic bond did not fail with a shear force of 2.72 N (shear stress = 0.68 MPa), the integrity of the eutectic bond was considered sufficient to undergo structural and phonon transmission studies.

2.3 Characterization

Several characterization techniques including He/Ne laser interferometry, optical microscopy, and transmission electron microscopy (TEM) were utilized in this study. Interferometry determined the quality (e.g., flatness, asymmetry) of the Ge surfaces to be bonded. Optical microscopy was employed to examine the surface morphology of the cleaved eutectic bonds. TEM was used to examine the surface morphology, crystallinity, structural continuity, and lattice mismatch of the eutectic interface.

2.3.1 Interferometry

To achieve a structurally intact Au-Ge eutectic bond, intimate contact must be made throughout the interface. Therefore, the Ge faces on which Pd and Au are deposited need to be extremely smooth and as flat as possible. Fizeau interferometry, which is explained in this section, was used to characterize the flatness of the optically polished Ge wafer surfaces.

Sir Isaac Newton illustrated the concept of interferometry with his discovery of Newton rings. Newton rings occur when light impinges on two materials placed one on top of the other. The light both transmits through and reflects within the first transparent material whose shape is either flat or planoconvex. The transmitted light then partially reflects off the planoconvex or flat surface of the opaque material underneath. Due to the interference between the light traveling back and forth between the two surfaces in intimate contact, alternating dark and bright fringes or rings are produced. The reflected wave undergoes a phase change of 180° (spatial path difference) whereas the refracted wave does not. The radius of the dark and bright fringes, respectively, are:

$$r \approx \sqrt{\frac{m\lambda R}{n}} \qquad [2.3a]$$

$$r \approx \sqrt{\frac{\left(m+\frac{1}{2}\right)\lambda R}{n}} \qquad [2.3b]$$

where R is the radius of curvature, λ is the wavelength, n is the index of refraction, and m is an integer.[Serway, 1986, 88] The 19th century French physicist, Armand Fizeau, used this phenomena to develop the Fizeau interferometer.[Incorporated, unknown, 37; Parker, 1989, 76; Robinson, et al., 1991, 83]

In the Fizeau interferometer, two surfaces are compared: the top surface is a transparent optically flat reference surface while the bottom surface is the test surface and is usually opaque. In this case, a He/Ne laser ($\lambda_{He/Ne}$=6328Å) is used as the light source. The laser beam impinges onto the flat reference surface which splits the beam. Half the laser beam is reflected and half passes through and reflects off the surface of the test sample (considered opaque). A half a wavelength change in surface height (hereafter surface = test surface) causes a one wavelength optical path change of the beam reflected off the surface. All beams converge or focus to one point and interference occurs yielding interference bands or fringe patterns. By adjusting the optics, the fringes are magnified and recorded on film.

The fringe patterns are essentially contour maps of the surface. Several types of information can be derived from the fringes: the symmetry of the surface height change, the area in which $\frac{n}{2}$ wavelength change occurs, and the test surface curvature. If the two surfaces are normal to the laser beam, Newton rings form. If the rings are concentric and circularly symmetric, the change in surface height is symmetric. If the ring is asymmetric, the surface is asymmetric with respect to height. If the rings are circular, the radius of the ring corresponds to a surface height change of $\frac{1}{2}\lambda$ (3164 Å). Assuming the surface shape is circular and the ring coincides with the outer edge of the surface, then the change in surface height is within $\frac{1}{2}\lambda$. By tilting the test surface with respect to the laser beam and reference surface, the fringes will form lines. If the lines are straight, the surface is flat.

Curved lines indicate the surface is either concave or convex. The amount of fringe curvature determines the deviation in surface height.

In this work, interferometry was an important tool for characterizing the quality of the Ge bonding surfaces prior to bonding. In addition, problems in the mounting procedure were determined and circumvented through analysis of interferograms. Figure 2.15a and 2.15b are plan views of the central (100) Ge wafer surrounded by Ge spacers. Figure 2.15a shows several spots on the central wafer which are due to air pocket formation under the wafer. The asymmetry of the fringes in figure 2.15b indicates uneven polishing of the central wafer due to either the lack of lapping block flatness or an uneven wax distribution between the lapping block and wafer.

To rectify these problems, the lapping block was itself lapped, heavier weights were placed onto the wafer and spacers while cooling the wax, and the polycrystalline Ge spacer density on the lapping block was increased. The interferograms of the lapping block surface after modification are shown in figure 2.16a and 2.16b. Figure 2.16a shows that the majority of the lapped surface is symmetric with a surface height change of no more than 3164 Å. Almost the full diameter is within one Newton ring. Tilting the lapping block results in straight fringes across almost the full surface (figure 2.16b). Spherometer measurements revealed that the central 3.5 cm diameter (~ diameter of Ge wafers) circular area is within $1/4\lambda_{He/Ne}$ or 1582 Å.

The improvements in the lapping block and mounting procedure resulted in improved Ge surfaces as shown by the interferograms seen in figures 2.17a and 2.17b. In figure 2.17a, the 3.5 cm diameter Ge wafer is within one Newtonian ring. Therefore, the surface height change over the radius of the wafer is < 3164Å ($\lambda_{He/Ne}$=6328Å). That is,

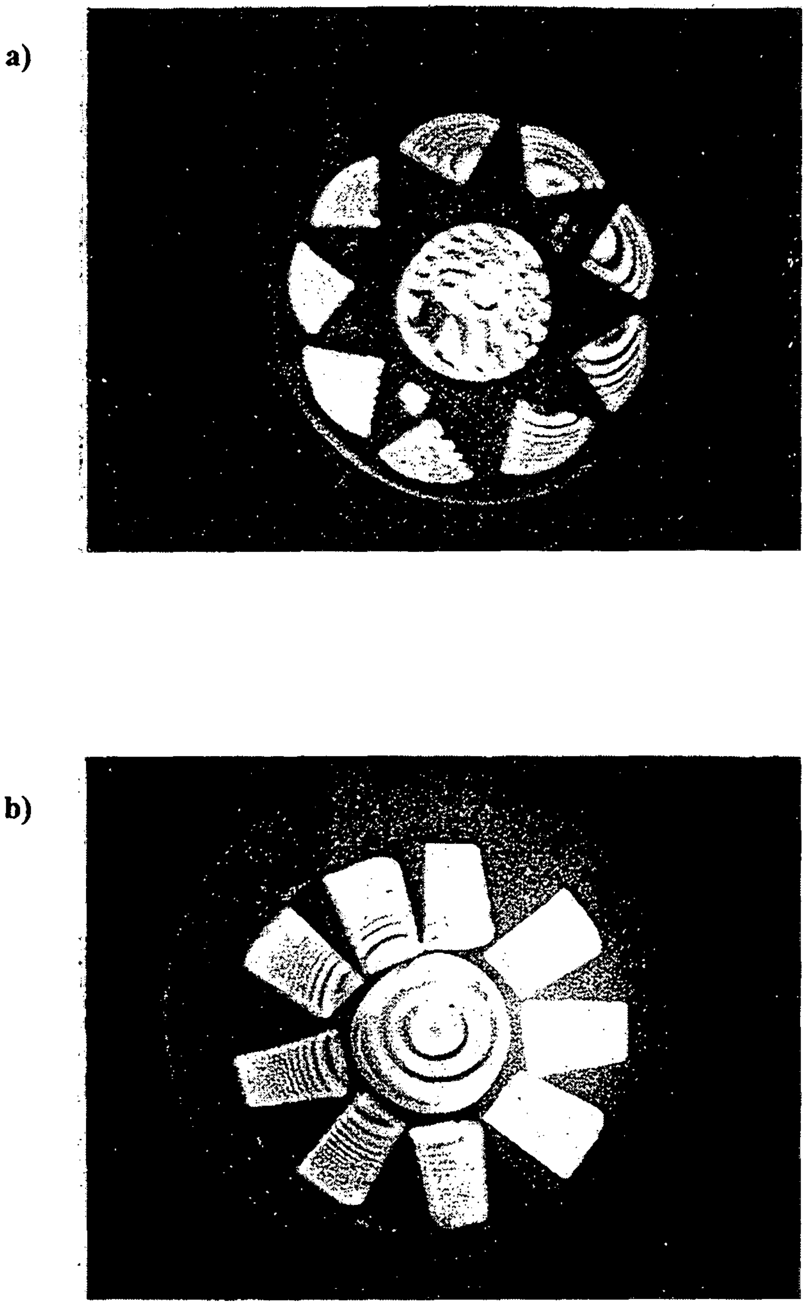

Figure 2.15: **a)** Plan view interferogram showing spots on the (100) Ge wafer centered between surrounding Ge spacers. **b)** Plan view interferogram of (100) Ge wafer showing asymmetry effects.

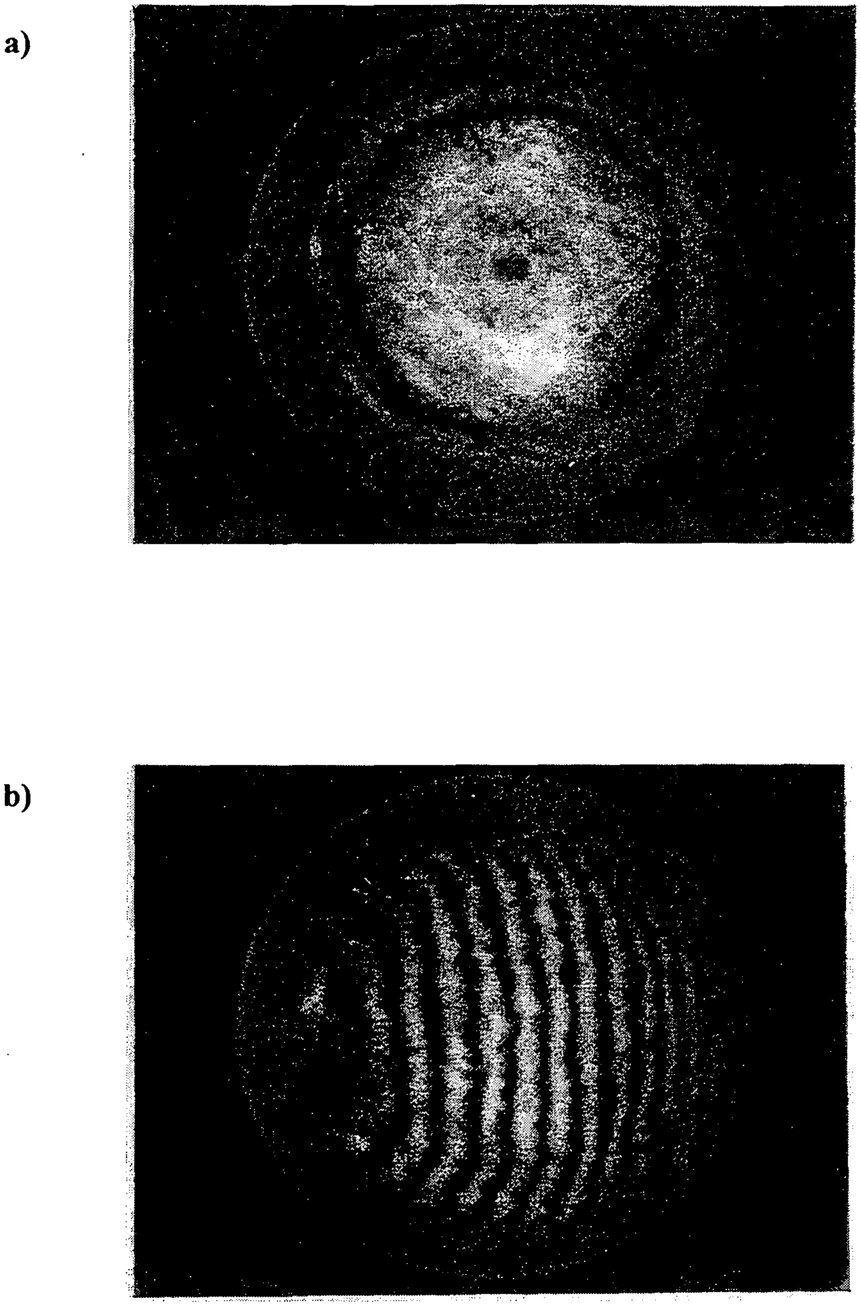

Figure 2.16: **a)** Plan view interferogram of lapping block surface following lapping. Almost the full diameter of the surface is within one Newton ring or $\frac{1}{2}\lambda_{He/Ne}$. **b)** Tilted view of lapping block surface showing the "contour line" of the surface. The straight lines indicate a flat surface.

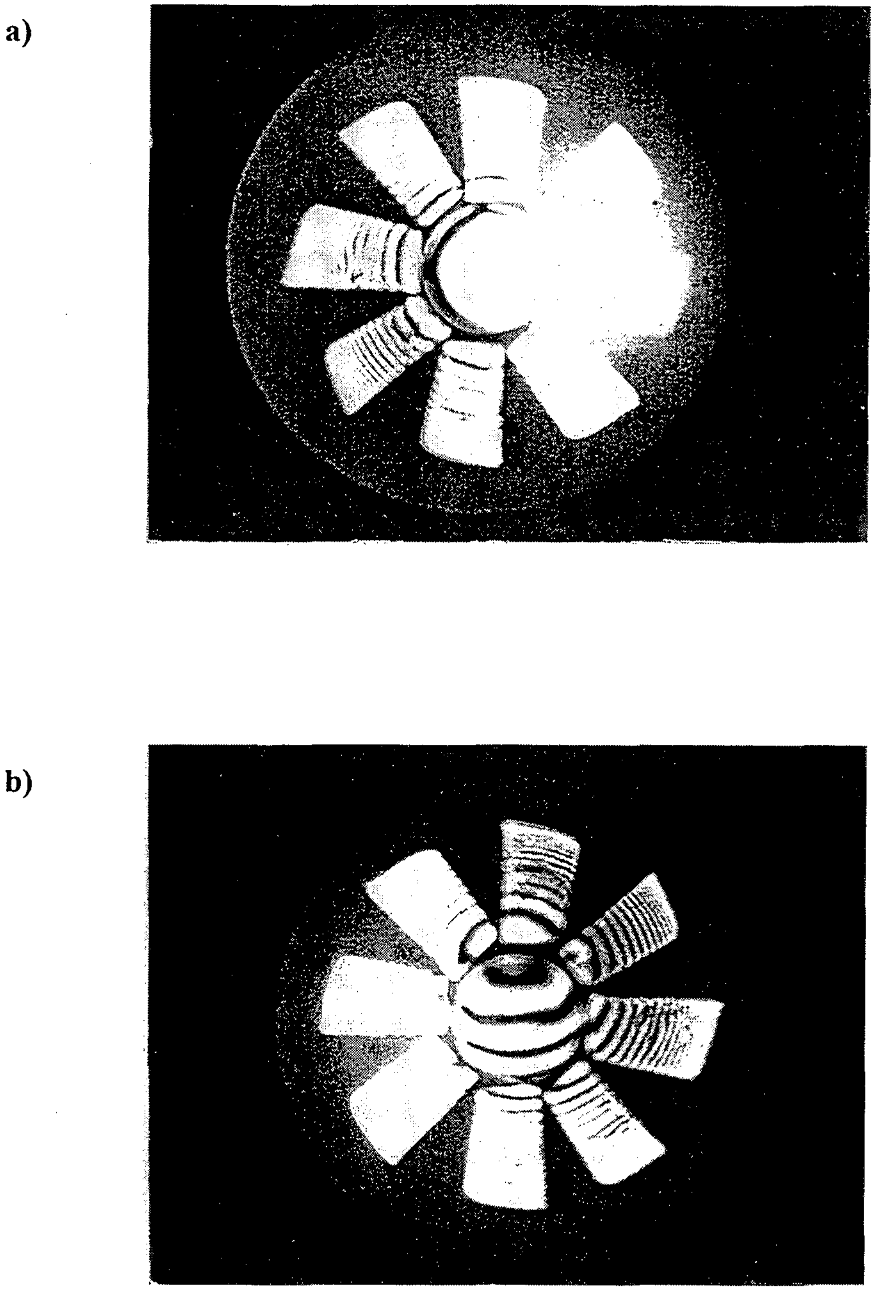

Figure 2.17: **a)** Plan view interferogram of 3.5 cm Ge wafer and spacers. The wafer's surface is within a $\frac{1}{2}\lambda_{He/Ne}$. **b)** Tilted view interferogram of the same wafer. The surface flatness is depicted by the contour lines which are straight over most of the wafer surface.

over an interval of 1 mm, the change in surface height is < 200Å indicating a highly optically flat surface. Second, the symmetric appearance of the fringe denotes a smooth surface morphology. The flatness is indicated by the relatively straight fringe contour lines seen in figure 2.17b.[Knowlton, et al., 1993, 46]

2.3.2 Optical Microscopy

In this study, optical microscopy is used to examine the morphology of eutectically bonded and free surfaces. The basic principles for optical microscopy including bright field microscopy, dark field microscopy, and differential interference contrast microscopy will be covered briefly in this section.

The optics of the optical microscope are not discussed here. This information can be found in many general physics books (e.g., Feynman Lectures). However, a definition of several figures of merit is given to aid in the understanding of the results. The *numerical aperture* (NA) is given by:

$$NA = n\sin\left(\frac{\alpha}{2}\right) \qquad [2.4]$$

where n is the refractive index of the medium between the lens and the object and α is the maximum angle at which the illuminating radiation can enter the lens when it is focused on the object. The minimum distance between different parts of an examined object or points which satisfies Raleigh's criterion (i.e., the limiting condition of resolution) defines the *resolution* of a microscope and is given by:

$$r_s = \frac{0.61\lambda}{NA} \qquad [2.5]$$

where λ is the wavelength of light in free space. The depth of the object in image space that is simultaneously in focus is called the *depth of focus* where:

$$D_{focus} = \frac{\lambda}{4(NA)^2} \qquad [2.6]$$

The depth of focus in object space is:

$$D_{field} = \frac{\lambda\sqrt{n^2 - (NA)^2}}{(NA)^2} \qquad [2.7]$$

and is called the *depth of field*. The magnification of the microscope can be expressed in terms of the ratio of the resolution limits of the eye and the microscope. It can also be represented with regard to resolving power and is given by the ratio of the maximum NA of the eye and microscope. Thus, *magnification* is given by:

$$M = \frac{\text{limit of microscope, } r_s^e}{\text{limit of eye, } r_s^m} = \frac{NA_{\max}^{eye}}{NA_{\max}^{microscope}} \qquad [2.8]$$

Bright field (BF) optical microscopy is what is generally known as optical microscopy. The incoming light impinges vertically onto the object surface and the light reflected by the object is observed.

Conversely, in *dark field* (DF) microscopy, a condenser lens deflects the incoming light so the light impinges at an angle. Therefore, only scattered light reaches the objective. The *contrast*, or the ability to distinguish between object parts, of small height variations or specular surfaces with different reflectance is enhanced. So, flat portions of the object do not reflect and remain black.

Differential interference contrast (DIC) examines the relief or small height variations (from several wavelengths to 1/20 of a wavelength) of the surface of an object. In DIC microscopy, the incident light is plane polarized and slightly phase shifted with a beam splitter. The incident and split beams pass through a condenser producing two transverse waves 90° out of phase but 45° from the normal axis of the plane polarizer. After reflecting off the object and passing through the objective lens, the beams pass through an adjustable beam splitter which recombines the light waves. The optical path difference, δ, between the recombined light gives rise to contrast and background differences. In table 2.1, several values of δ and the derived background brightness are given. In all three types of microscopy, the use of a green filter enhances contrast since the human eye is especially sensitive to that region of the visible spectrum.

Table 2.1: Values of δ and related background brightness (Schroder, 1990, 86a)

δ	**Background**
0	dark
$\lambda/4$	medium
$\lambda/2$	bright

After eutectic bonding, the cleaved surface morphology of eutectic bonds with differing Pd and Au thicknesses was examined using optical microscopy. Cleaving of the

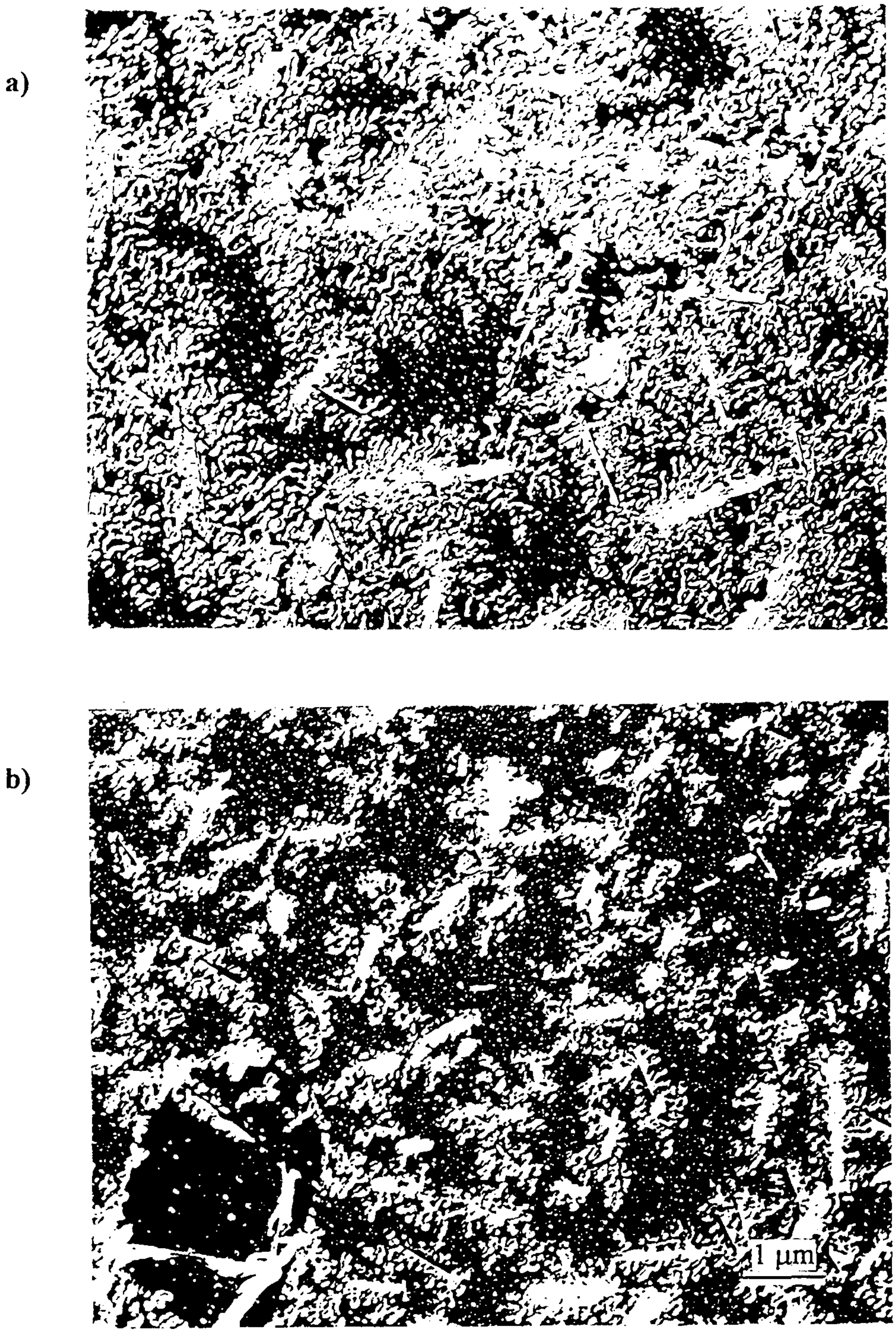

Figure 2.18: **a)** Optical micrograph of a cleaved eutectic bond with an initial Au deposition thickness of 900 Å/side. **b)** Optical micrograph of a cleaved eutectic bond with an initial Au deposition thickness of 700 Å/side.

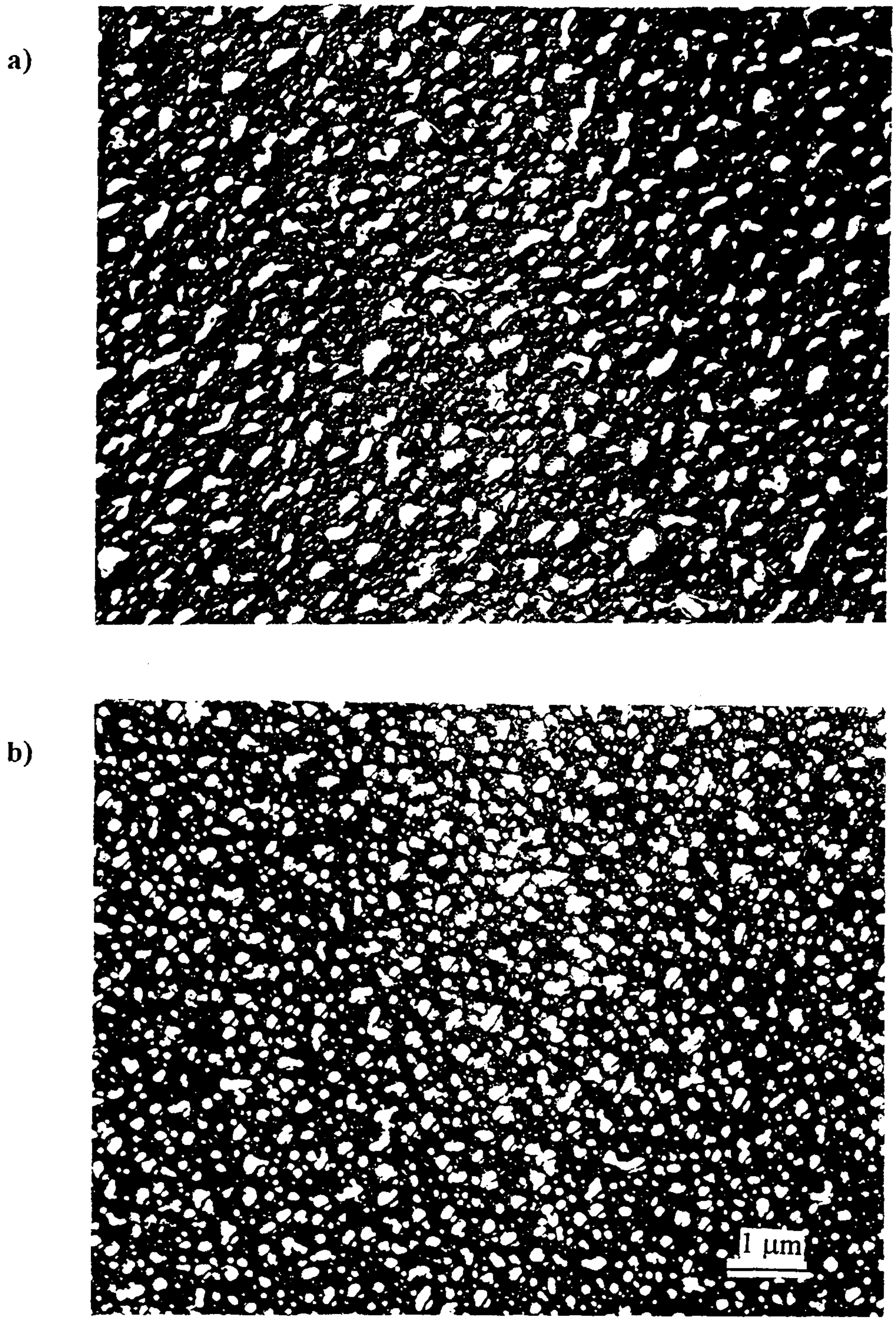

Figure 2.19: **a)** Optical micrograph of a cleaved eutectic bond with an initial Au deposition thickness of 500 Å/side. **b)** Optical micrograph of a cleaved eutectic bond with an initial Au deposition thickness of 300 Å/side.

eutectic bond was performed by placing a razor blade at the interface of the two bonded Ge pairs and applying a force. Optical microscopy of the cleaved samples with initial Au thicknesses of 900 Å/surface (sample surface) and 700 Å/surface revealed Ge area coverages of 20% and 30%, respectively. This is seen in the plan view (i.e., view perpendicular to interface) bright field (BF) optical micrographs shown in figures 2.18a and 2.18b. In these optical micrographs, the dendritic eutectic structure is seen. For Au deposition film thicknesses greater than 500 Å/surface, cleaved samples showed that the dentritic eutectic structure was retained. However, for cleaved samples with initial Au film thicknesses of 500 Å/surface or less, the dendritic eutectic morphology was replaced by the formation of Au agglomerates covering only 20% to 30% of the interface. The plan view BF optical micrographs in figure 2.19a and 2.19b show the eutectic microstructure of Au precipitate formation for initial Au thicknesses of 500 Å/side and 300 Å/side, respectively.

2.3.3 Transmission Electron Microscopy (TEM)

Transmission electron microscopy (TEM) was used extensively in this study to examine eutectic interfaces both in *plan view* (i.e., with the electron beam approximately normal to the plane of the interface) and in *cross section* (i.e., with the electron beam at grazing incidence to the interface). TEM is a powerful analytical tool used in the characterization of materials. The great strength of TEM is that it provides access to information in real and reciprocal space using the same instrument. Furthermore, it offers the ability to filter in one space and observe the effect in the other space.

In TEM, electrons are accelerated to greater than or equal to 100 keV and pass through a thin sample (~ 100 Å to 10 μm thick). The electrons are focused electromagnetically, and they are filtered in real and reciprocal space with apertures placed in the electron beam. The wave-like nature of the incident electrons (and all electrons) gives rise to diffraction from a periodic arrangement in the material. A crystal will therefore act like a diffraction grating resulting in well defined maxima in reciprocal space. The transmitted beam and diffracted beams can be used to form an image in several ways.

The two types of imaging used in this thesis were *low magnification* (< x100,000) *diffraction contrast* and *high magnification* (≥ x100,000) *phase contrast*. In low magnification diffraction contrast, usually either the transmitted or a single diffracted beam are used to form an image. *Bright field* (BF) is used to denote images formed using the transmitted beam while *dark field* (DF) is used to denote images formed with a diffracted beam. These images contain information about crystal orientation and perfection, and they are commonly used to investigate the structure of extended crystal defects (e.g., dislocations, stacking faults, precipitates, etc.). Diffraction contrast images are obtained from crystals as thick as several micrometers.

In phase contrast, many diffracted beams are used together with the transmitted beam to generate an image. The image contains periodic fringes corresponding to the projected planar spacings of the crystal. Phase contrast images are usually taken along high symmetry directions containing several low index planes. Phase contrast is applicable only to very thin (~ 100 Å) specimens. For a full discussion of phase contrast imaging, refer to the references of Loretto and Thomas.[Loretto, 1984, 52; Thomas and Goringe, 1979, 96]

In *selected area diffraction* (SAD), an aperture in real space is used to limit the area of the specimen from which diffraction information is collected. The diffraction pattern is a reciprocal space ($\bar{k}$-space) representation of the specimen. Diffraction patterns contain structure and symmetry information. A diffraction pattern from an amorphous material shows few features. Diffraction patterns from polycrystalline materials show concentric rings while diffraction patterns from crystalline materials are comprised of spots. Diffraction patterns are analyzed to determine such physical properties as the crystal structure, the crystal orientation, the lattice parameter, and the lattice mismatch between dissimilar materials.

Understanding image contrast requires knowledge of diffraction theories. If diffraction of the previously diffracted beam is considered, then *dynamical theory* must be used. The much simpler *kinematic theory* is used if diffraction of the previously diffracted beam is assumed not to occur. Kinematic theory is valid for thin specimens and weak scattering (diffraction) of electrons. If the crystal is oriented with respect to the incident electron beam such that only one diffracted beam is excited, then the *two beam approximation* (two beam condition) is assumed.[Hull and Bacon, 1984, 35] This further simplifies the analysis of diffraction contrast images. Full discussion of diffraction contrast is beyond the scope of this thesis. For those whose curiosity desires to be satisfied, the aforementioned theories are presented in the references of Loretto and Thomas.[Loretto, 1984, 52; Thomas and Goringe, 1979, 96]

A brief introduction to the ideas of the analysis of diffraction patterns is sufficient for the data presented in this thesis. Furthermore, this will be done only for cubic crystalline materials, which greatly simplifies the analysis, since the materials under investigation are cubic.

As previously mentioned, these diffraction patterns represent a two dimensional projection of the reciprocal lattice (in reciprocal or $\bar{k}$-space) of the material. The reciprocal lattice is defined by a *general reciprocal lattice vector* given by:

$$\bar{g}_{hkl} = h\boldsymbol{a}^{*} + k\boldsymbol{b}^{*} + l\boldsymbol{c}^{*} \qquad [2.9]$$

where (*hkl*) represent the Miller indices of the real space lattice planes, and $\boldsymbol{a}^*$, $\boldsymbol{b}^*$, and $\boldsymbol{c}^*$ are the reciprocal lattice fundamental translation vectors such that:

$$\boldsymbol{a}^{*} = \frac{\boldsymbol{b} \times \boldsymbol{c}}{V_c} \qquad [2.10a]$$

$$\boldsymbol{b}^{*} = \frac{\boldsymbol{a} \times \boldsymbol{c}}{V_c} \qquad [2.10b]$$

$$\boldsymbol{c}^{*} = \frac{\boldsymbol{a} \times \boldsymbol{b}}{V_c} \qquad [2.10c]$$

The volume of the real space unit cell, V_c, is given by:

$$V_c = \boldsymbol{a} \cdot \boldsymbol{b} \times \boldsymbol{c} = \boldsymbol{b} \cdot \boldsymbol{c} \times \boldsymbol{a} = \boldsymbol{c} \cdot \boldsymbol{a} \times \boldsymbol{b} \qquad [2.11]$$

where $\boldsymbol{a}$, $\boldsymbol{b}$, and $\boldsymbol{c}$ are the real lattice fundamental translation vectors (unit cell basis vectors). Note that the dot product between $\boldsymbol{a}$ and $\boldsymbol{b}^{*}$, $\boldsymbol{b}$ and $\boldsymbol{b}^{*}$, and $\boldsymbol{c}$ and $\boldsymbol{c}^{*}$ is 1. The general reciprocal lattice vector is normal to the planes (hkl) and its magnitude is equal to the reciprocal of the interplanar spacing, d_{hkl}, such that:

$$\left|\bar{g}_{hkl}\right| = \frac{1}{d_{hkl}} \qquad [2.12]$$

For cubic crystals, d_{hkl} is given by:

$$d = \frac{a}{\sqrt{h^2 + k^2 + l^2}} \qquad [2.13]$$

where a is the lattice constant. The interplanar distance, d_{hkl}, is determined from the diffraction pattern by the *camera constant*, λL:

$$d_{hkl} = \frac{\lambda L}{r} \qquad [2.14]$$

where L is the distance from the sample to the diffraction pattern recording film, λ is the electron's wavelength determined by the beam energy, and r is the distance from the center of the diffraction pattern to a specific diffraction spot. In TEM, the electron wavelength is small (~ 10^{-2} Å) so the corresponding Bragg angles (θ) for widely spaced planes (a few Angstroms) are less than 1°. It can therefore be assumed that, to a first approximation, the diffraction pattern is a planar section through the reciprocal lattice. The Bragg angle is defined such that electron scattering in a crystal will occur if the following condition is met:

$$n\lambda = 2d\sin(\theta) \qquad [2.15]$$

where n is an integral number.[Cullity, 1978, 18] Hence, by simply measuring the distance between two diffraction spots, planar spacing and angles are determined using equations 2.13, 2.14, and 2.15.

To determine the crystal structure, additional information is necessary. In crystals with more than one atom in the basis, certain lattice planes will not give rise to diffraction maxima. In general, the kinematical *structure factor* (scattering amplitude) of the unit cell, F_g, given by:

$$F_g = \sum_j f_j\left(\frac{\sin\theta}{\lambda}\right)e^{(2\pi\bar{g}\cdot\bar{r}_j)} \qquad [2.16]$$

where $\bar{r}_j$ is the general real lattice vector for the jth atom's position, $f_j(\sin\theta/\lambda)$ is the *atomic scattering factor* for the jth atom, and the sum is over all the atoms in the unit cell. The *general real lattice vector*, $\bar{r}$, is given by:

$$\bar{r} = xa + yb + zc \qquad [2.17]$$

The dot product between $\bar{g}$ and $\bar{r}$ is an integral value because, as previously mentioned, the dot products between the real and reciprocal fundamental lattice vectors of the same letter is 1. The condition F_g=0 gives the disallowed diffracting planes.[Thomas and Goringe, 1979, 96] Physically, this corresponds to destructive interference between atomic planes with a spacing of less than a projected unit lattice vector. In certain high symmetry directions, disallowed reflections may be present because of multiple diffraction (dynamical theory).

Transmission electron microscopy was used to examine both the cleaved and uncleaved eutectic bond structure. Plan view and cross section geometry eutectically bonded samples were prepared using standard mechanical, chemical, and ion-beam thinning procedures.[Loretto, 1984, 52; Thomas and Goringe, 1979, 96] Bonded samples with an initial Au thickness of 300 Å/side were analyzed first, followed by the samples with an initial Au thickness of 1000 Å/side. Using low magnification diffraction contrast, TEM analysis was done in plan view of a cleaved eutectically bonded surface. This gives a much larger sampling area and therefore a good overview of the morphology. A BF TEM micrograph in figure 2.20 shows the Au precipitate eutectic morphology with approximately 70% Ge surface coverage confirming the results given by optical

Figure 2.20: BF plan view micrograph of a cleaved eutectic bond with a 300 Å/side initial Au thickness revealing a 70% of the area is Ge. The areas marked **A**, **B**, and **C** indicate where SAD patterns were taken of Au, Ge, and Au and Ge, respectively.

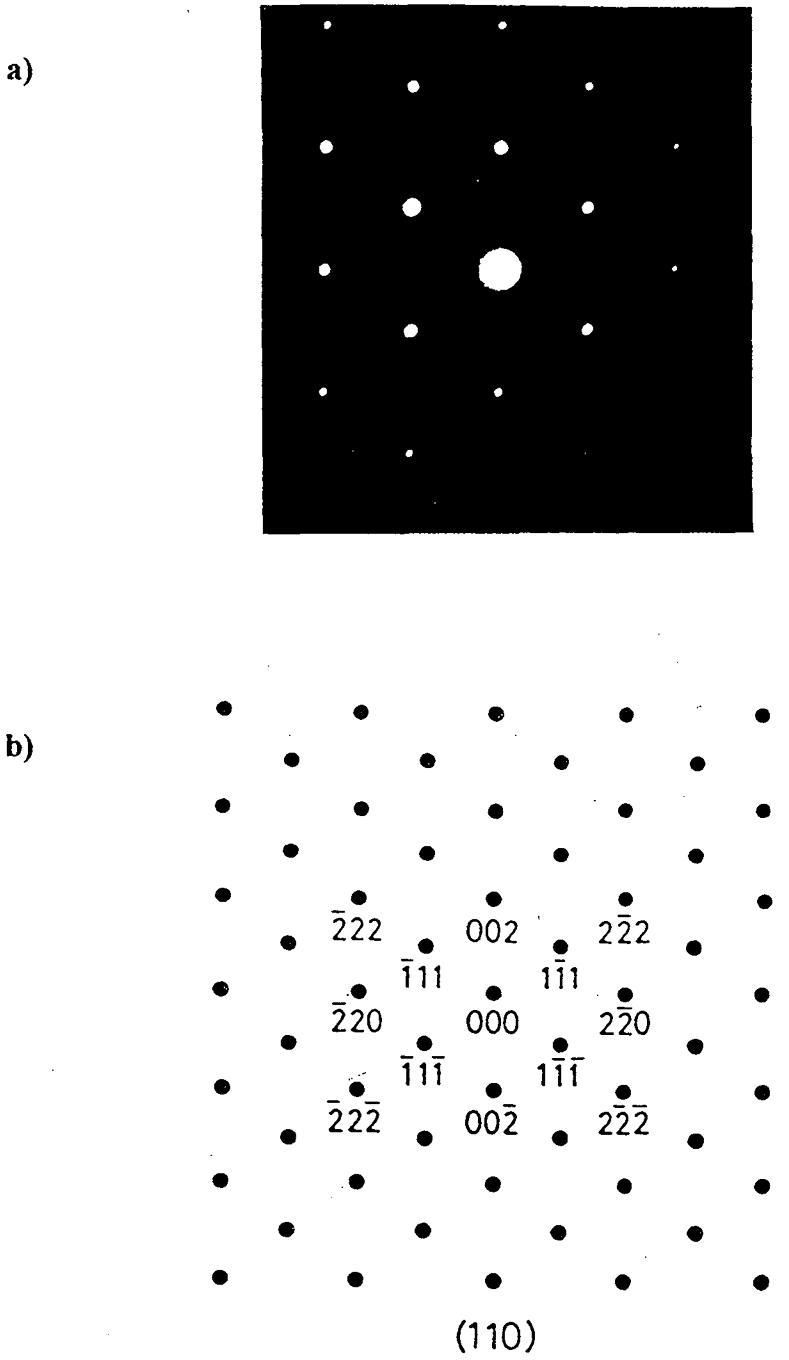

Figure 2.21: **a)** SAD pattern of Au showing a single crystal [011] orientation. **b)** An indexed representation of a).

microscopy. The areas marked A, B, and C are Au precipitates, the Ge matrix, and the border of a Au precipitate and the Ge matrix, respectively. Using the selected area diffraction mode, SAD patterns in figure 2.21a of the Au agglomerations (figure 2.20, area A) indicated the Au was crystalline with a <011> orientation. An indexed representation of this diffraction pattern is shown in Figure 2.21b. The indices denote the planes which are orthogonal to [011] and were responsible for the diffraction spots.

The SAD patterns of the Ge on either side of the Au precipitates were independently taken. One SAD pattern is shown in figure 2.22a. The indexed diffraction pattern (figure 2.22b) shows that the Ge is single crystal oriented in the [100] direction. Note that the indices shows only the planes which actually diffract the electron beam. They are determined by the structure factor, given by equation 2.16, and the crystal structure. So, the indices denote the planes which are orthogonal to [100] and were responsible for the diffraction spots. In figure 2.23a, a SAD pattern is shown of a Au precipitate on top of Ge. The diffraction pattern shows a superlattice structure. In other words, the [011] Au diffraction pattern is superimposed onto the [100] Ge diffraction pattern. The alignment of the Au diffraction pattern with respect to the Ge diffraction pattern indicates that heteroepitaxial regrowth occurred between the Ge and Au.

The Au and Ge heteroepitaxial interface is illustrated schematically in figure 2.24. Note in figure 2.23a and 2.23b that the diffraction spots of Ge in the [022] direction almost coincide with the Au diffraction spots in the [200] direction. By measuring the magnitude of $\bar{g}_{hkl}$ (hereafter $\boldsymbol{g}_{hkl}$) in these directions, and using the fact that $\boldsymbol{g}_{hkl}$ is the reciprocal of the interplanar spacing, d_{hkl}, the lattice mismatch in this direction was found to be ~ 1.55%. Using the known lattice constant values for Ge and Au, the lattice

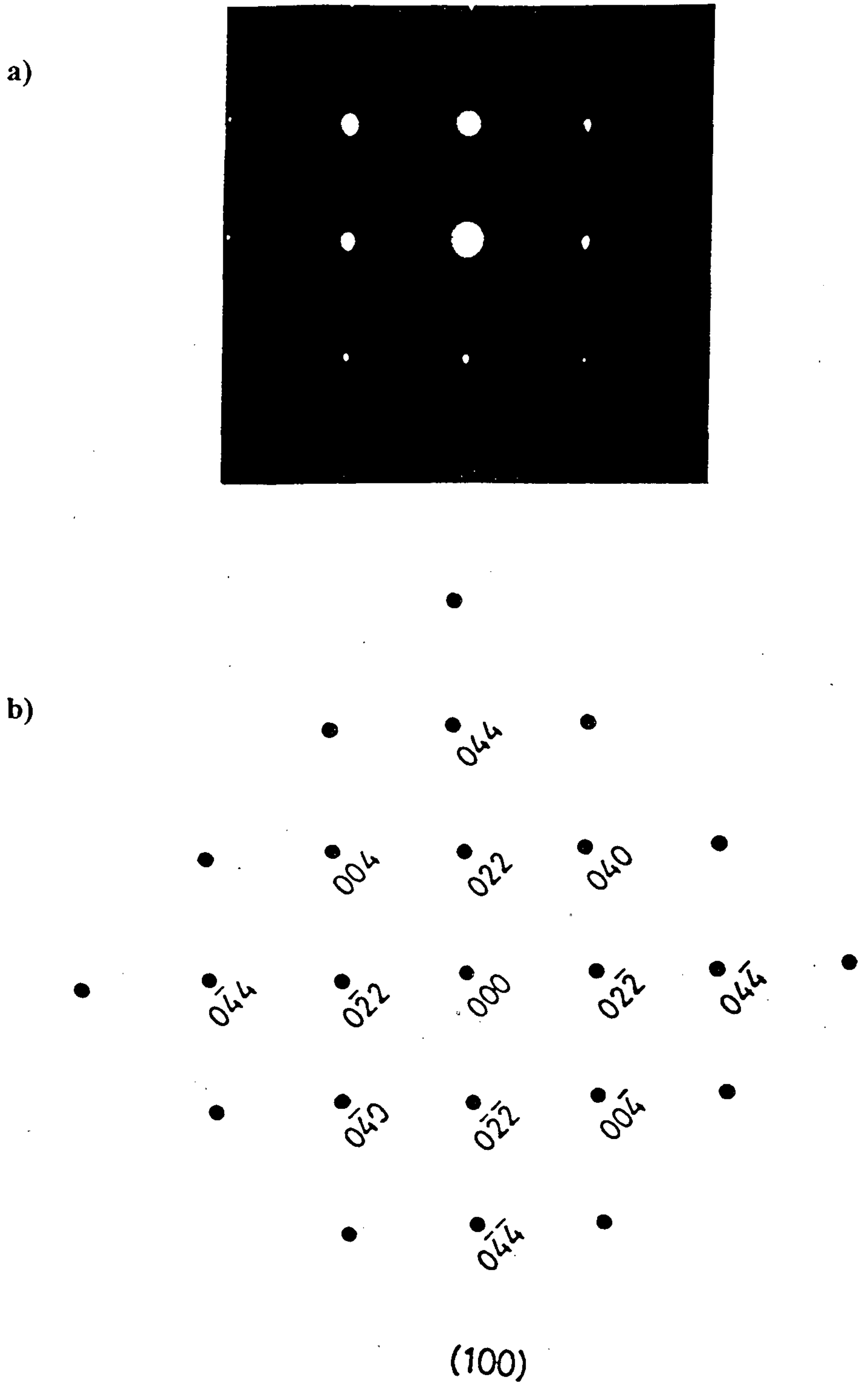

Figure 2.22: **a)** SAD pattern of Ge showing a single crystal [100] orientation. **b)** An indexed representation of a).

a)

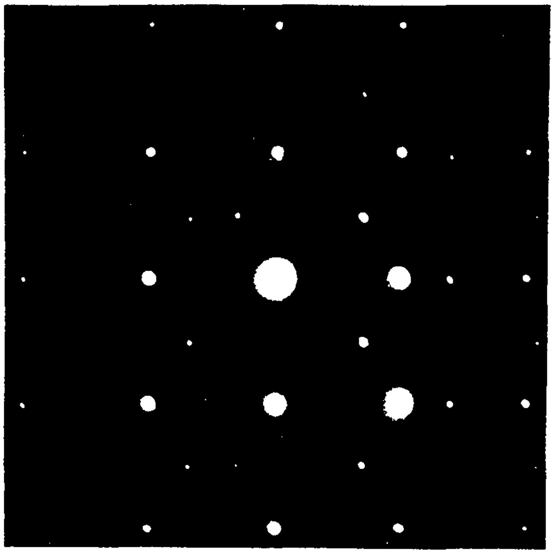

Figure 2.23: **a)** A SAD (selected area diffraction) pattern from area C showing the superlattice structure between Ge and Au. The Ge and Au are superimposed in a specific orientation indicating epitaxial growth had occurred.

b)

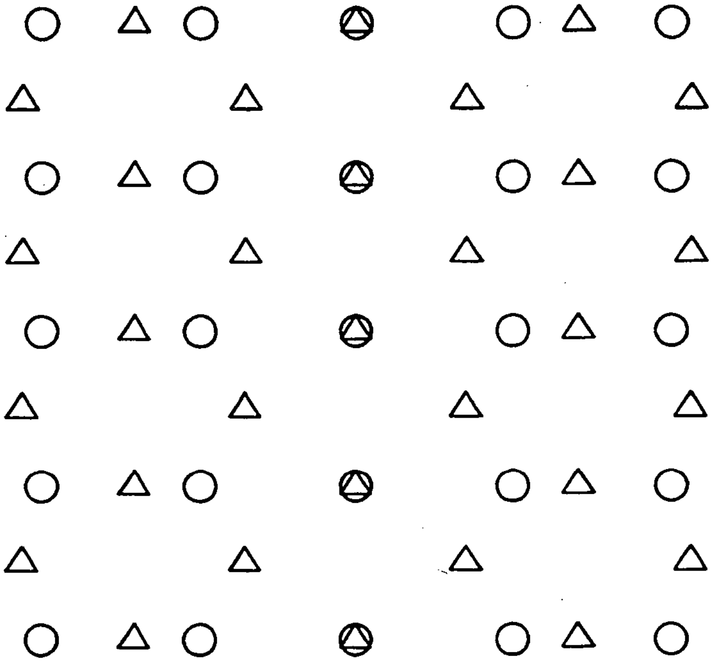

Figure 2.23: **b)** The indexing of a) shows the orientation of the Ge-Au superlattice. The circles and triangles correspond to the [100] and [011] orientation, respectively.

mismatch for this orientation was calculated as 1.95%. The difference could be related to the relaxation of the lattice in this direction. Although the diffraction spots of Ge in the [022] and Au in the [200] directions almost coincide, figure 2.23a and 2.23b show that the diffraction spots of Ge in the $[02\overline{2}]$ and Au in the $[02\overline{2}]$ direction do not coincide. The lattice mismatch in this orientation using the measured values of g_{hkl}'s is 28.0% while the calculated values using known lattice constants for Ge and Au is 27.9%. The small difference may signify either that lattice relaxation did not occur in this direction.

A structural representation of the Ge-Au eutectic interface is shown in figure 2.24. The plan view in figure 2.24a shows the epitaxial interface between Au (light atoms) and Ge (dark atoms). The volume shown is 20 Å by 20 Å in the plane and 20 atoms deep. The cross section view of the Ge-Au heteroepitaxial interface is shown in figure 2.24b. The Au (light) is orientated in the [002] direction while the Ge (dark) is orientated in the [220] direction.

TEM diffraction contrast imaging from cross sectioned specimens was used to examine the eutectic interface of samples with 300 Å /side initial Au thickness. The Ge lattice continuity across the interface and the structural morphology of the interface was examined. Figure 2.25 is a BF micrograph with a x30,000 magnification (hereafter, magnification = x30,000 = x30k) of a cross sectional view of the eutectic interface. The dark regions are Au precipitates which are surrounded by a Ge matrix. Note the faceted shape of the Au precipitates. The predominant measured angles of the Au facets ranged between 37° to 41°. The alternating bright and dark fringes are diffraction effects due to the varying thickness of the region. The sample thickness was a minimum at the interface and increased away from the interface. The hazy, dark and somewhat curved single lines

a)

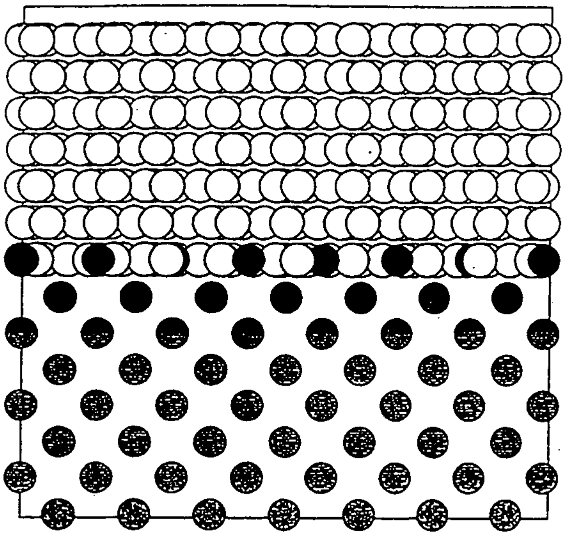

b)

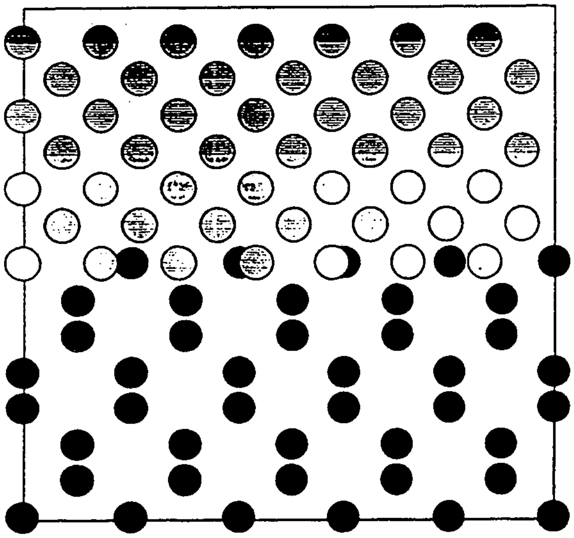

Figure 2.24: **a)** A real space plan view representation of the SAD pattern shown in figure 2.23a depicting the Ge-Au heteroepitaxial interface. The Au atoms (light) are slightly misoriented from the [022] direction. The Ge orientation is [200]. **b)** A real space cross sectional view of the heteroepitaxial interface. The orientation of the Au and Ge is [200] and [220], respectively.

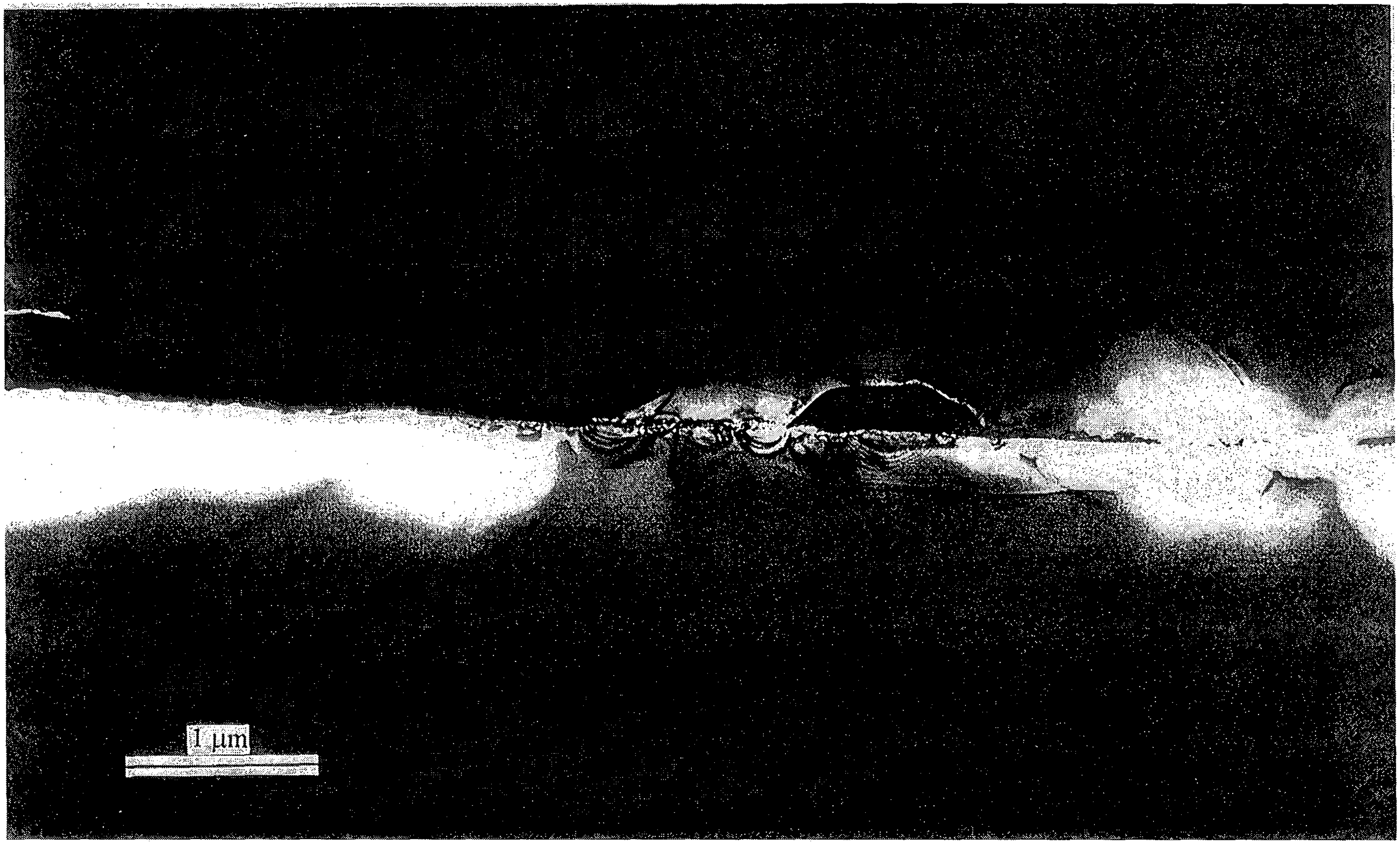

Figure 2.25: BF TEM micrograph showing the cross sectional view of a eutectic interface. The dark faceted form in the interface is a Au precipitate.

are most likely bend contours caused by stress from defects. The fringes and bend contours can be seen more clearly in the BF image of the interface shown in figure 2.26. The label “s” signifies a probable stacking fault or a planar defect.[Knowlton, et al., 1993, 46]

A BF image (x240k) in figure 2.27 was taken with the interface tilted 10° away from edge on to resolve the presence of any voids or defects. The crater-like structures are voids although their numbers were small relative to the continuous Ge interface.

In the area labeled “D” within the BF micrograph (x57k) shown in Figure 2.28, phase contrast high resolution TEM (HRTEM) micrographs of the cross sectional view of the interface were taken. This sample had an initial Au thickness of 300 Å/side. Note that Au precipitates do not exist in this region, therefore only the Ge interface is examined. The HRTEM micrograph is shown in figure 2.29. The eutectic interface is depicted by the arrow. The HRTEM micrograph illustrates Ge homoepitaxial growth across the interface. In other words, the Ge lattice is continuous through the interface. The two sets of {111} planes (atomic spacings ~ 3 Å) are clearly resolved in this image. The features resembling atoms are Ge "dumb bells" and arise from the projection of the two atom basis in the Ge unit cell. The top half of the micrograph is aligned with the [110] zone axis. The bottom half of the micrograph is slightly off the zone axis, indicating a less than a 1° misorientation between the two Ge interfaces.[Knowlton, et al., 1993, 46]

Cross sectional TEM was performed on bonded samples with 1000 Å/side initial Au thickness. The goal was to determine the existence and amount of Ge lattice continuity across the interface and the interface morphology. A low magnification (x4.3k) cross sectional BF TEM micrograph in figure 2.30 shows that at least 90% of the interface

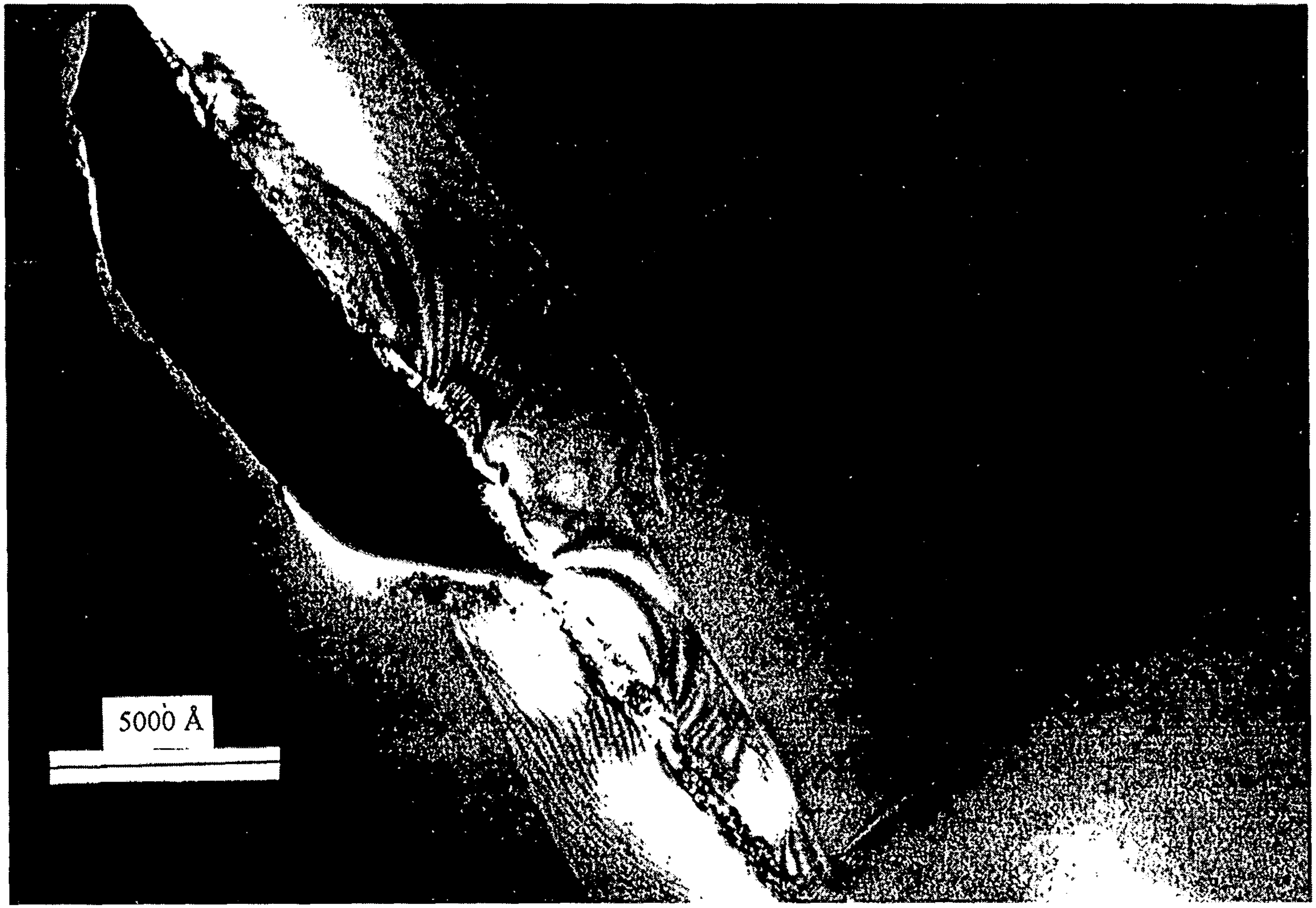

Figure 2.26: A higher magnified (x111k) BF TEM micrograph showing the cross sectional view of a eutectic interface better illustrates the Au precipitate, the bend contours, and possible stacking fault (labeled "s").

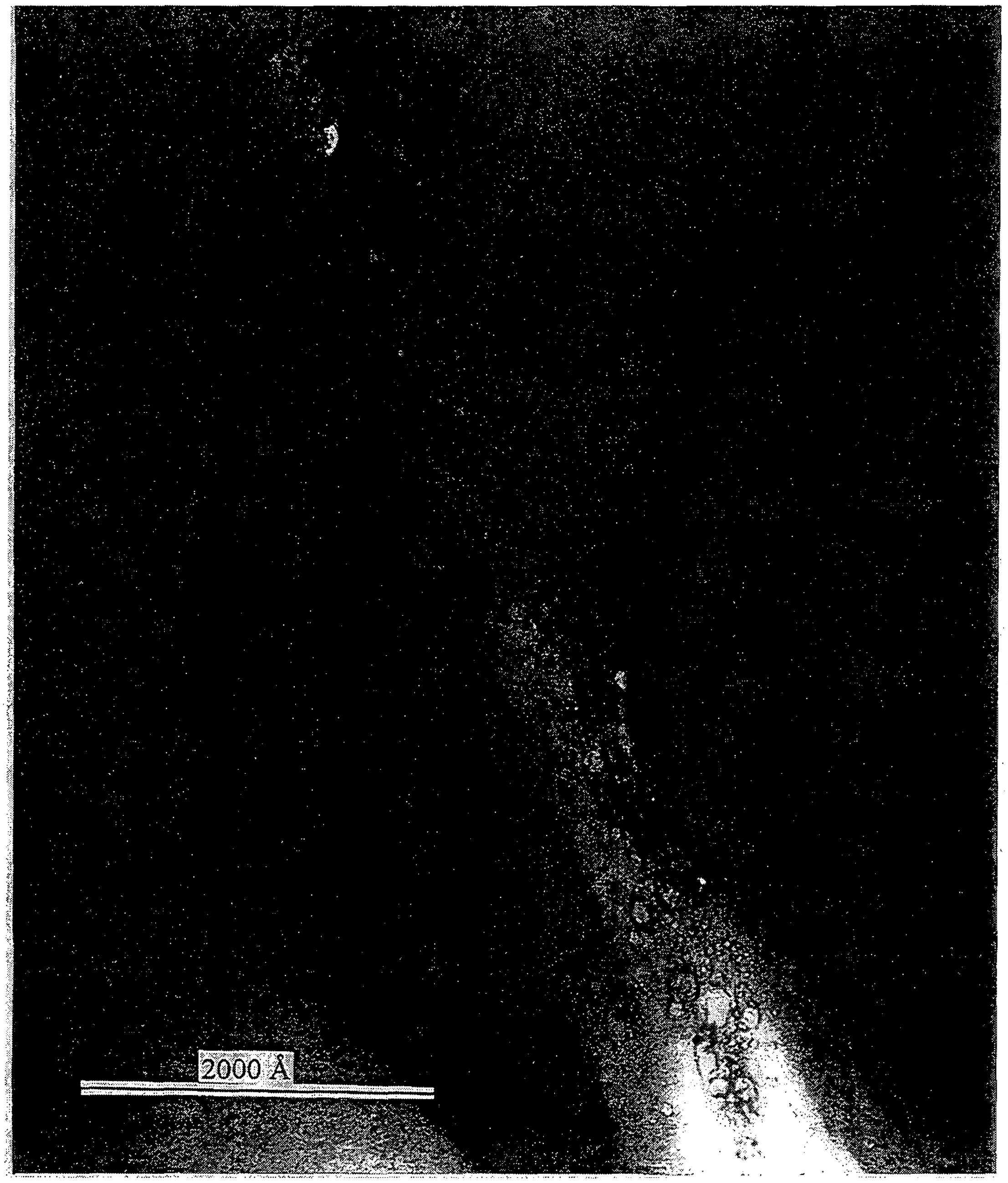

Figure 2.27: A ~10° tilted x240k BF TEM micrograph showing the presence of voids along the interface.

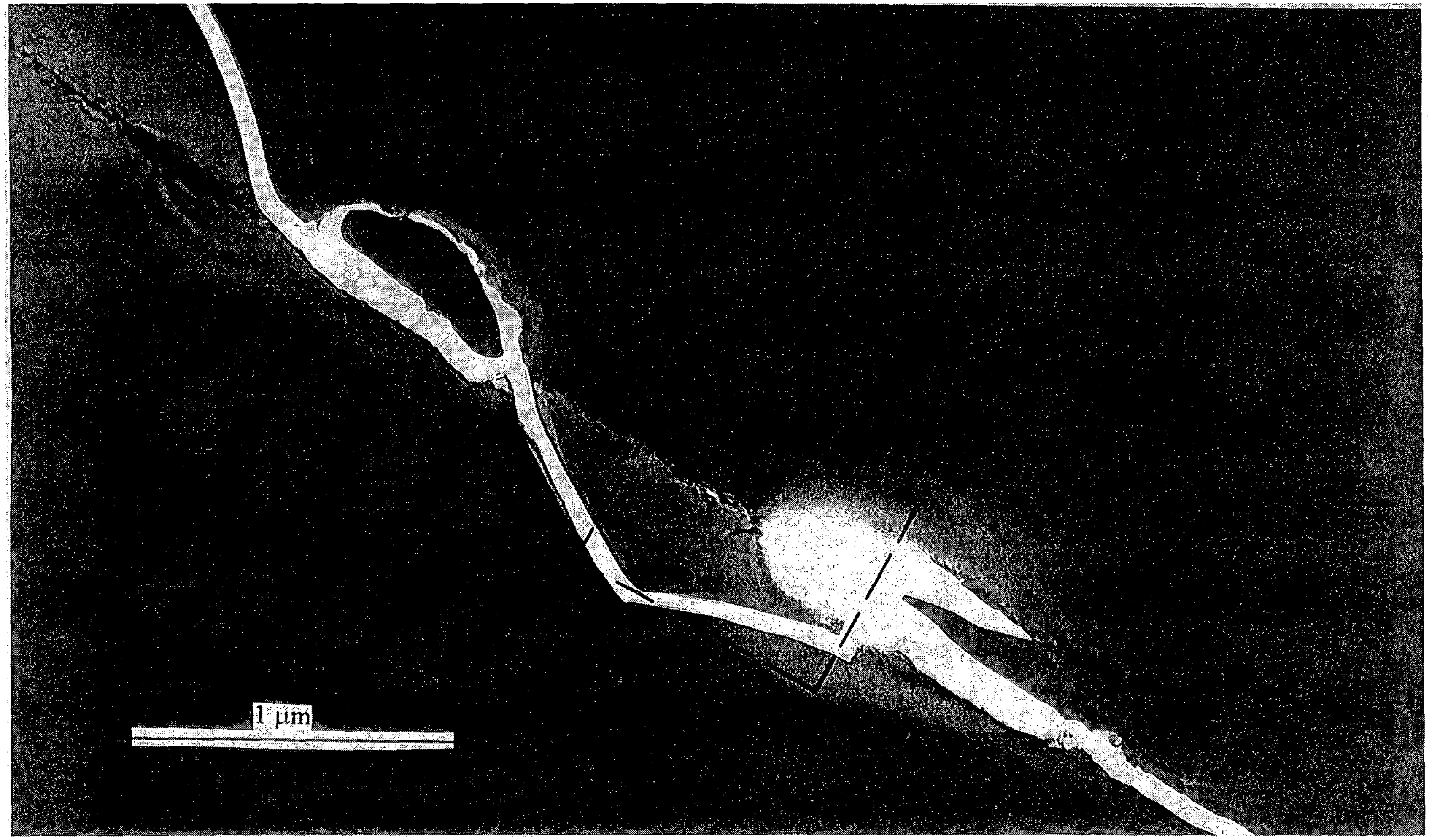

Figure 2.28: BF TEM micrograph showing the area, “D”, of the eutectic interface where HRTEM was performed.

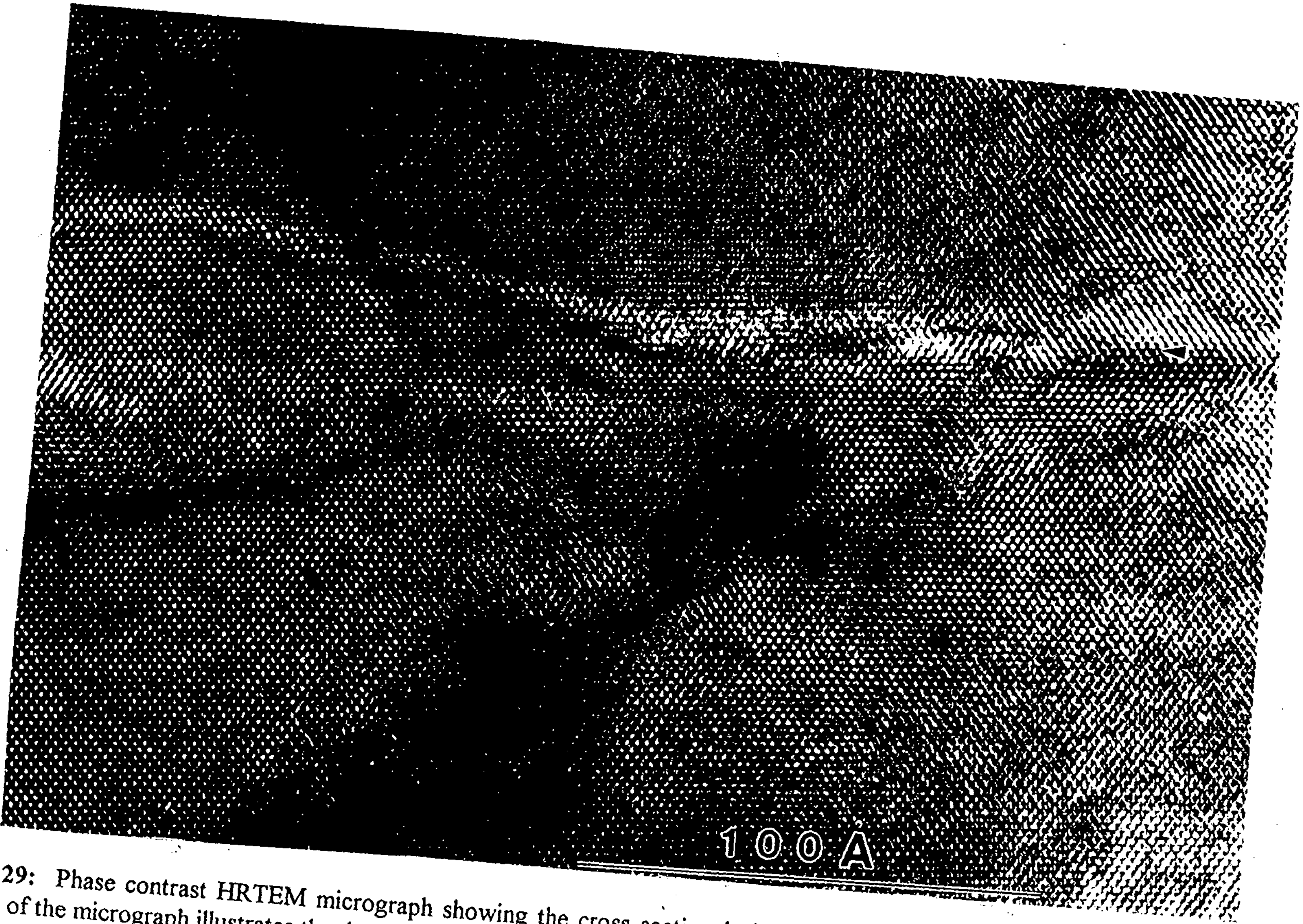

Figure 2.29: Phase contrast HRTEM micrograph showing the cross sectional view of a Ge region eutectic interface. The atomic resolution of the micrograph illustrates that homoepitaxial growth is continuous across the interface. The arrow indicates the interface.

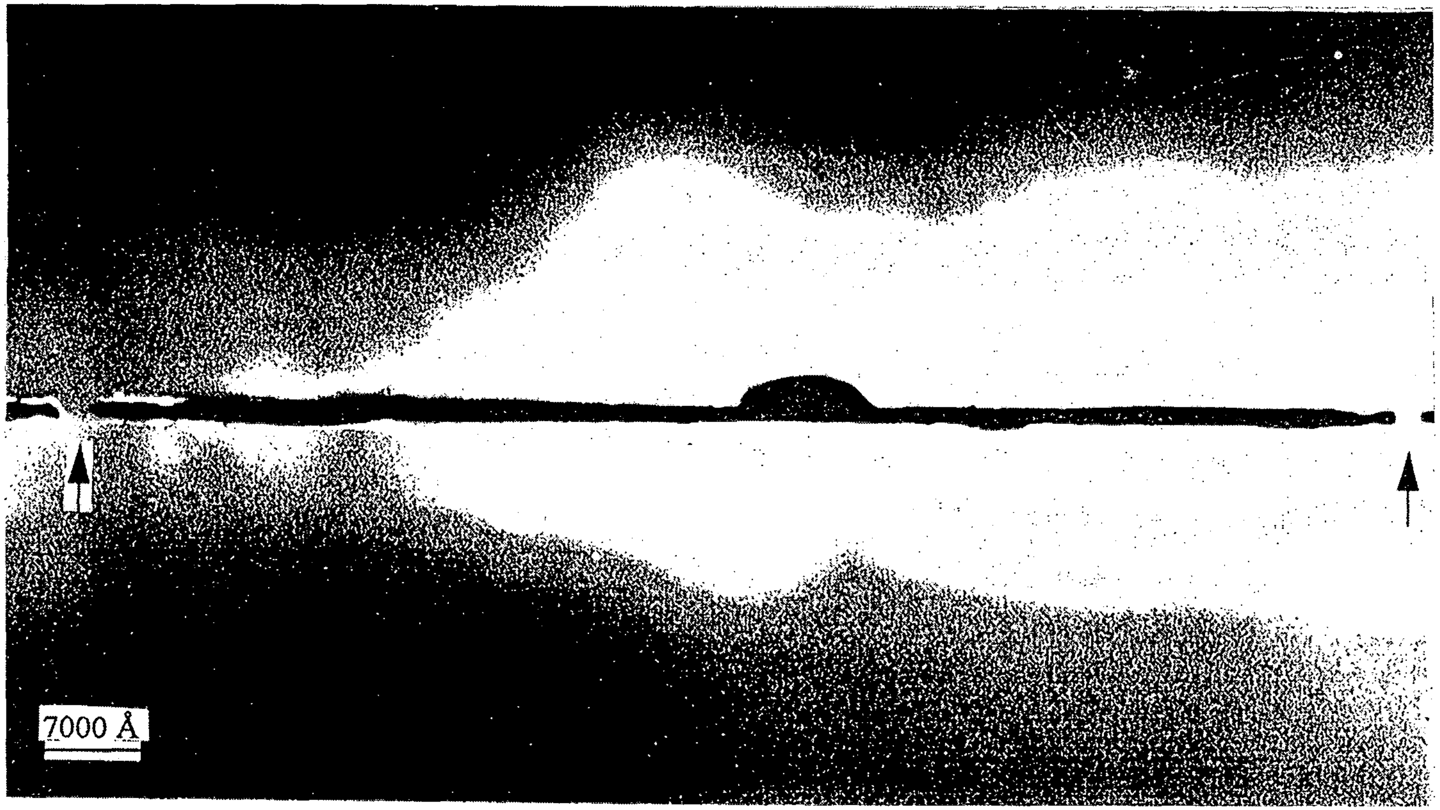

Figure 2.30: BF TEM micrograph showing the cross sectional view of a sample with an initial Au thickness of 1000 Å/side eutectic interface. The dark stripe is the Au surrounded by the light Ge. Note the two smaller Ge bridges at the left and right sides of the TEM micrograph in the interface shown by the arrows. The fact that the contrast does not change through the bridge to either side of the interface indicates that the Ge bridges are single crystal.

consists of Au. Since the interface length is so much greater than the interface width, the figure of 90% is not an area but a linear representation. The Au was determined to be single crystal by SAD. The Au thickness across the interface is ~ 2000 Å which correlates with the 2000 Å total thickness of Au deposited. The two arrows point to regions of the interface where the Ge bridges cross the interface. Increasing the magnification to x19k, figures 2.31 and 2.32 show details of similar Ge bridges. SAD of the Ge bridges indicated both good crystallinity and a (110) orientation. The high magnification (x100k) BF micrograph of a Ge bridge in figure 2.33 indicates they are continuous across the interface. This is supported by HRTEM as shown in figure 2.34, where homoepitaxial growth of Ge through the interface is seen indicating the misorientation is less than 1°.

From the data presented, it is interesting to note that eutectic epitaxial bonding of Ge with Au initial thicknesses of 500 Å/side or less produced faceted Au aggregates. As mentioned before, Au agglomerates have been seen during Au liquid mediated homoepitaxial film growth of Ge.[Xiong, et al., 1991, 110] They have also been seen in annealed Ge-Au/Au bilayers.[Ba, et al., 1995, 4; Zhang, et al., 1992, 112] Numerous studies of Ge-Au ohmic contacts on GaAs have mentioned the problem of Au agglomeration and the addition of Ni to prevent it.[Edwards, et al., 1972, 20; Heime, et al., 1974, 29; Iliadis and Singer, 1983, 36; Poate, et al., 1978, 79; Procop and Sandow, 1986, 82] The fact that Au precipitates formed, rather than a continuous layer of Au film, suggests that lateral diffusion of both the Au and Ge occurred in the liquid during epitaxial growth (solidification). The driving force for such a mechanism could be that the surface tension of Au in the liquid increases as the temperature decreases. However, since the

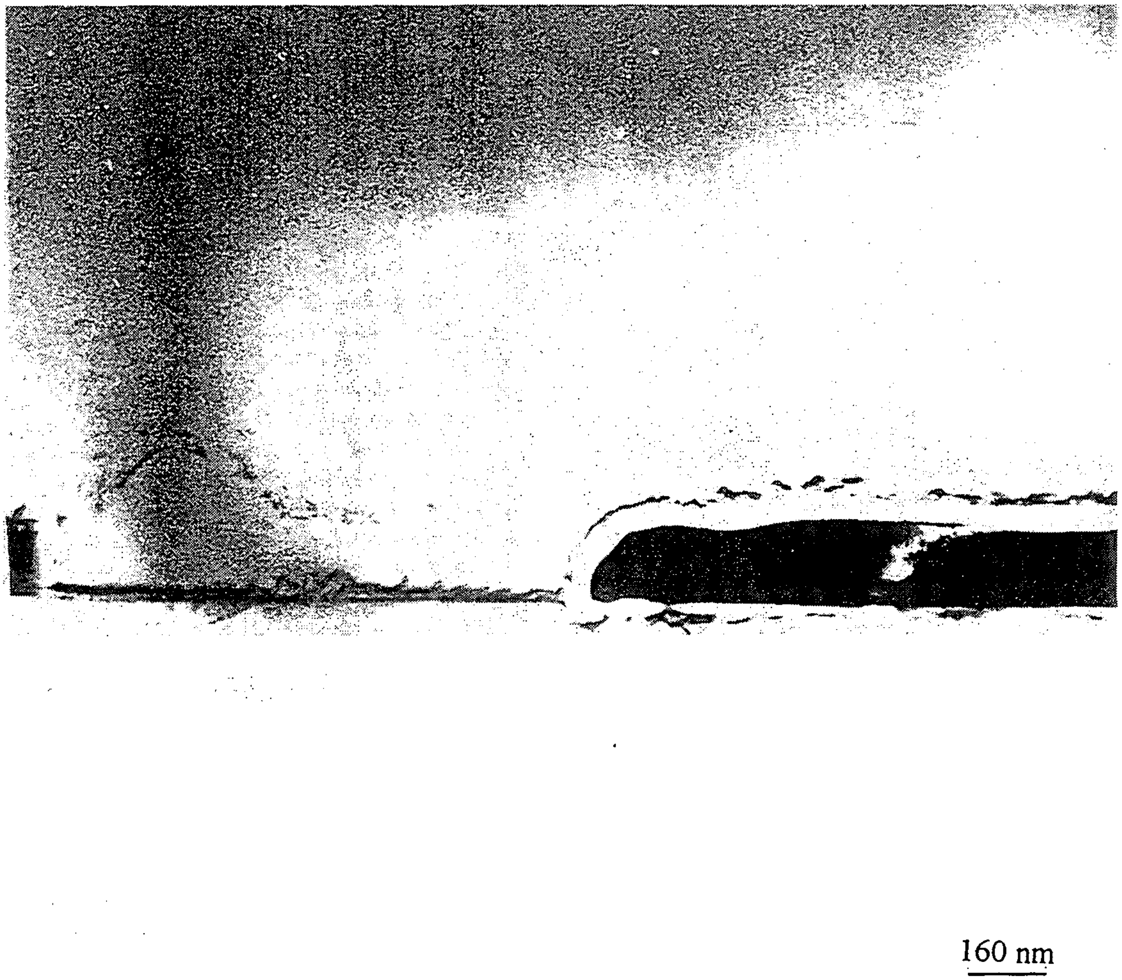

Figure 2.31: BF TEM micrograph showing a Ge bridge across the eutectic interface.

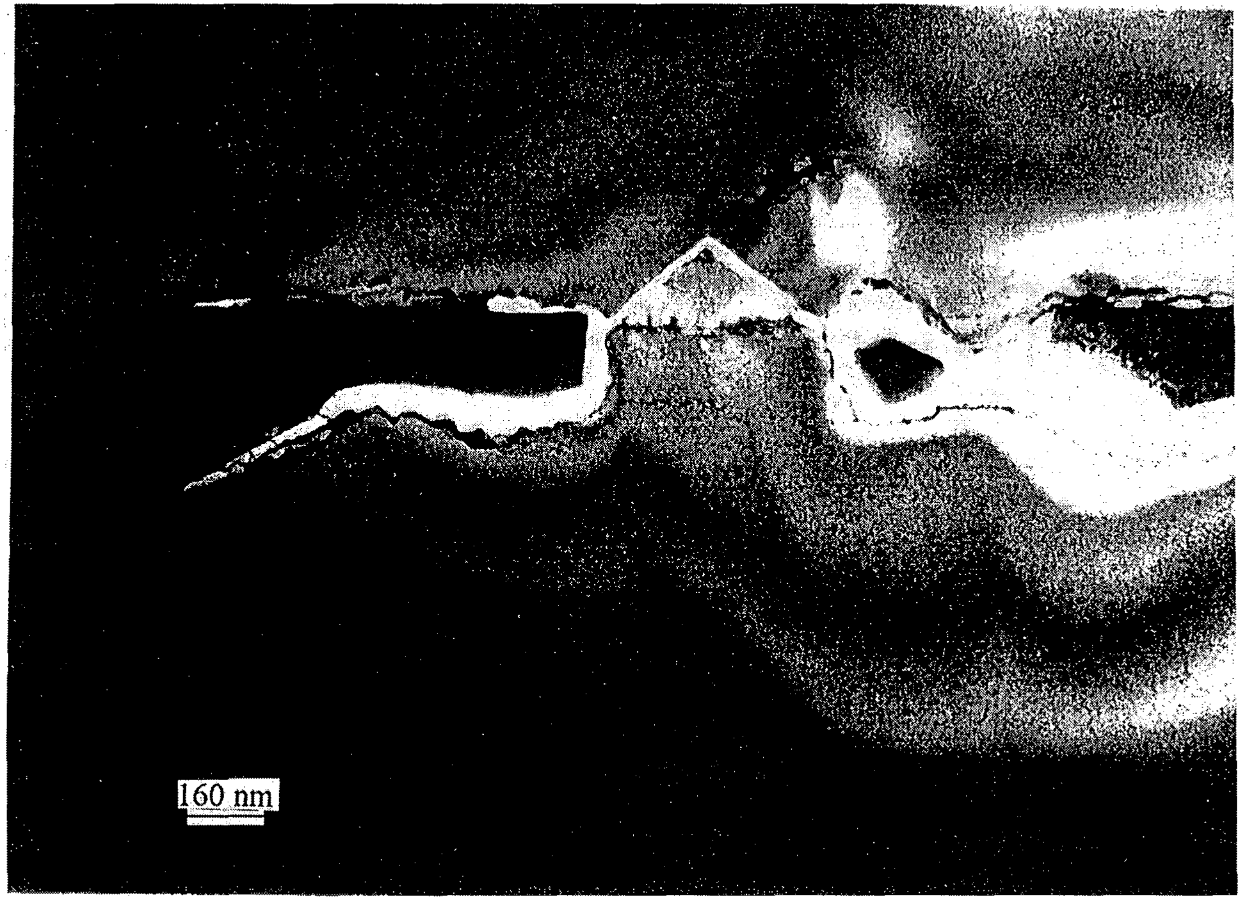

Figure 2.32: BF TEM micrograph showing another Ge bridge across the eutectic interface.

Figure 2.33: High magnification (x100k) BF TEM micrograph of Ge bridges indicating lattice continuity across the eutectic interface.

Figure 2.34: HRTEM (x530k) micrograph showing homoepitaxial growth of Ge bridges across the eutectic interface. The interface is shown by the arrows.

composition of the liquid at the eutectic point consists of 28 at. % Ge, the Ge surface tension should also be considered. Figure 2.35 is a plot of the surface tension of liquid Au and Ge as a function of temperature. Note that as the temperature decreases, the surface tension increases for both the Au and Ge. Therefore, surface tension may play a role in Au agglomeration. Yet, the eutectic temperature is lower than the temperature range indicated. Hence, to use the information in the plot, the assumption is made that Au in the liquid eutectic will follow the same trend as Au in a pure liquid. To evaluate this assumption, the regular solution model can be used.[Gaskell, 1981, 27; Porter and Easterling, 1981, 81] The regular solution model gives a first order approximation of the extent that a solution deviates from ideality (i.e., ideal solution). In this case, the regular solution model can predict (to first order) to what extent Ge and Au will interact in the liquid phase. However, the time required to properly treat this problem is too extensive to do so in this thesis.

The formation of Au precipitates rather than a continuous layer may occur if the density of Au decreases as the temperature decreases and approaches the eutectic temperature. The likelihood of this occurring increases if the density of liquid Ge also decreases as a function of temperature. However, the density of both Ge and Au does not decrease. This can be seen in figure 2.36 in which a plot of liquid Au and liquid Ge densities as a function of temperature is shown. Both the Au and Ge liquid densities increase as the temperature decrease. Upon solidification, the density of Ge decreases, since Ge undergoes a volume contraction upon melting.[Hansen and Haller, 1992, 28] However, the density of Au increases upon solidification. The density of pure Au increases from 17.36 g/cm^3 at its melting point to 19.3 g/cm^3 at room temperature. Since

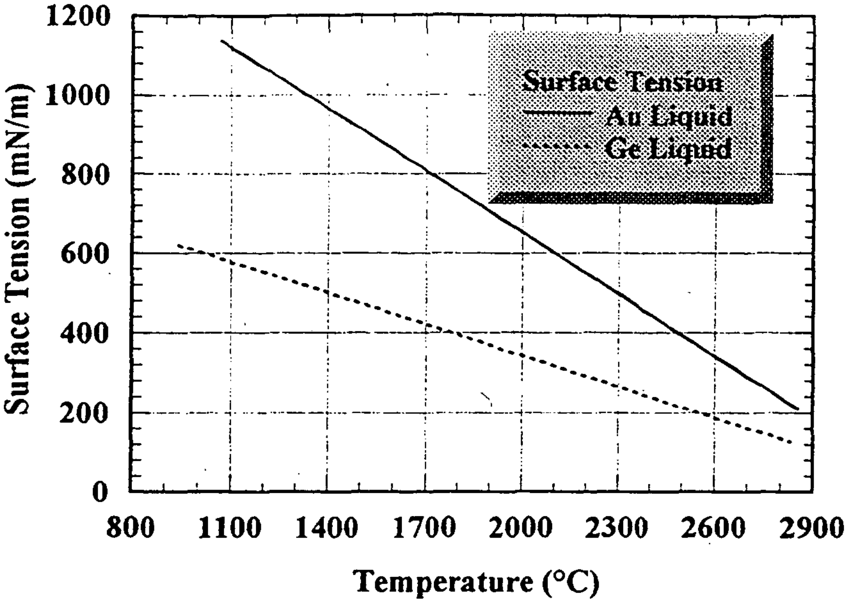

Figure 2.35: Surface tension as a function of temperature for Au and Ge liquid.

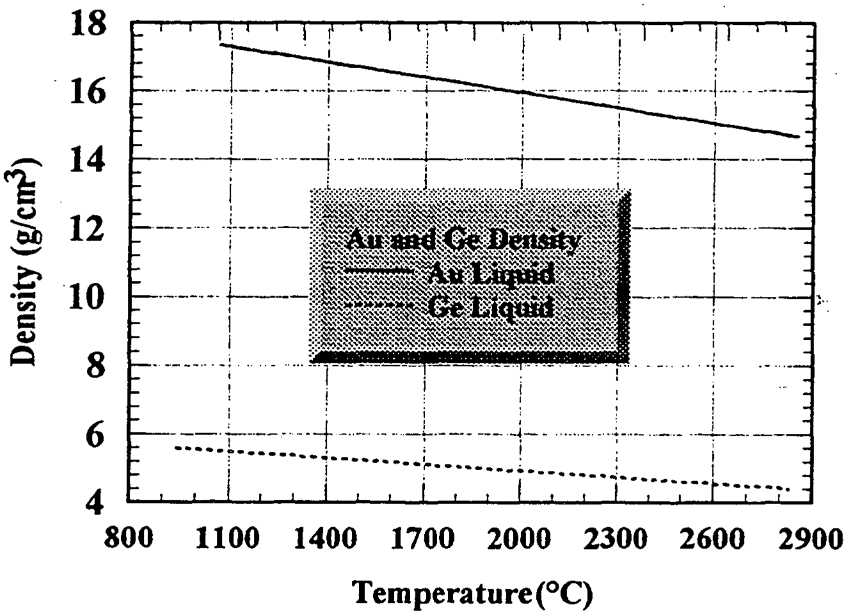

Figure 2.36: Density as a function of temperature for Au and Ge liquid.

density is the inverse of a normalized volume, then the volume of Au should decrease upon solidification. Thus, the driving force for Au precipitation may be correlated to density. However, the plots show densities of pure elements, so the interaction between Ge and Au in the liquid is assumed not to occur. Again, regular solution theory would need to be used to determine if interaction between Ge and Au atoms does not occur in the liquid phase.

Faceting of the Au precipitates suggest that heteroepitaxial growth was occurring due to oriented growth. Furthermore, the faceting indicates that the eutectic solidification was anomalous in nature. However, covalent materials facet much more readily than do metals, so it is most likely that Ge is faceting rather than the Au precipitates.[Hellawel, 1970, 30]

It should be mentioned that not all the interfaces examined showed epitaxial continuity through the interface. In those samples which did not, the interface contained amorphous Ge with epitaxial Au agglomerations. The amorphous Ge suggests that either impurities (e.g., dust) or misorientation of the bonding pairs hindered epitaxial growth. Stress could also be a factor, since as stated above, Ge undergoes a volume expansion during the liquid to solid phase transformation.

3. Interface Phonon Transmission Studies

The purpose of this chapter is to describe phonon focusing and imaging and their application in the characterization of Ge-Au-Ge eutectically bonded interfaces. The first section is devoted to an overview of phonon physics, the second to nonequilibrium phonon theory, the third to the sample processing, fabrication, and the experimental procedures used in phonon transmission studies, and the fourth to the discussion of the obtained results.

3.1 Phonons

3.1.1 Introduction

A phonon is a quantum of lattice vibrations. It can also be thought of as an energy quantum propagating through a cystal lattice. One way energy can be dissipated in a solid is by the formation of phonons (i.e., the displacement of the atoms in the solid). The source of energy can be a laser impinging on a solid surface, a neutron impacting a nucleus of an atom, or electromagnetic radiation (e.g., gamma ray) interacting with the electrons of atoms. The lattice of a particular solid will have a number of natural patterns of vibrations termed *normal modes.* They are analogous to normal modes of a vibrating string fixed at both ends or an air column with standing longitudinal waves (e.g., a pipe organ or flute). Each mode has a characteristic frequency. The modes in the crystal are determined using Newton's Second Law otherwise known as the *equation of motion* given by:

$$\sum \bar{F} = m\bar{a} \qquad [3.1]$$

where $\bar{F}$ is the applied force, m is the mass of the atom and $\bar{a}$ is the acceleration of the atom.

The wave and particle duality of phonons is analogous to that of photons. Photons are quantized light waves, and phonons are quantized lattice vibrations. Quantum mechanically, a phonon is a quantum or wave packet of lattice vibrations existing where the atoms of the lattice are periodically displaced from their equilibrium position.[Blakemore, 1985, 8] The wave quantum is identified by its momentum vector ($\bar{k}$), energy (E($\bar{k}$)), phase velocity ($v_p(\bar{k})$) of the wave packet, and group velocity ($v_g(\bar{k})$) of the plane waves within the wave packet. The energy of a phonon is given by:

$$E(\bar{k}) = \hbar\omega \qquad [3.2]$$

where ω is the phonon angular frequency. The phase velocity of the waves in a wave packet is written as:

$$v_p = \frac{\bar{n} \cdot E(\bar{k})\omega}{\hbar|\bar{k}|} = \bar{n} \cdot \frac{\hbar\omega}{\hbar|\bar{k}|} = \bar{n} \cdot \frac{\omega}{|\bar{k}|} \qquad [3.3a]$$

where

$$\bar{k} = \frac{2\pi}{\lambda} \qquad [3.3b]$$

and

$$\bar{n} = \frac{\bar{k}}{|\bar{k}|} \qquad [3.3c]$$

is the unit vector of $\bar{k}$.

The group velocity of a quantum of lattice waves is the quotient of the gradient of the phonon energy and $\hbar$ and is expressed as:

$$v_g = \frac{\nabla E(\bar{k})}{\hbar} = \frac{\frac{\partial(\hbar\omega)}{\partial\bar{k}}}{\hbar} = \frac{\partial\omega}{\partial\bar{k}} \qquad [3.4]$$

In the following sections, the equation of motion (equation 3.1) is applied to several models to predict the modes of vibrations. The first case, phonons within the elastic regime, shows that if only small atomic displacements occur, then the lattice may be modeled as an isotropic medium. This result will be important in this study. The next model describes the harmonic oscillator which lays the foundation for the final model. This model attempts to predict modes of vibrations in a two-atom basis monatomic media such as Ge. The result is then compared to actual experimental data.

3.1.2 Phonons in the Elastic Regime

When an applied force displaces an atom in a crystal, the atom's bonds resist. This resisting or restoring force can be approximated from the potential energy of the bonds. The plot of potential energy versus distance from the atom's core is shown in figure 3.1 The potential energy for the bonds between atoms is seen to be quadratic in form for small

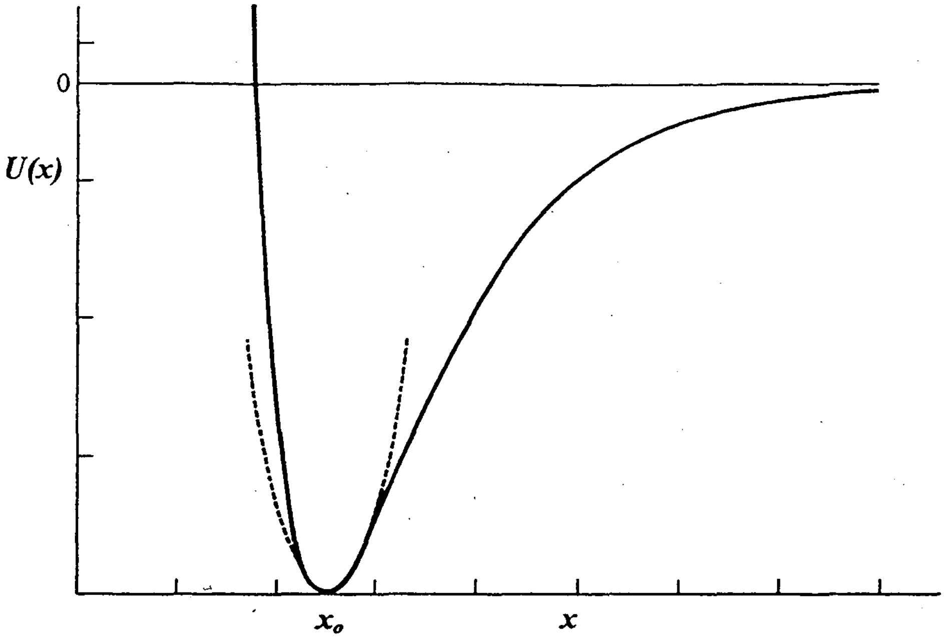

Figure 3.1: The potential energy versus displacement of a molecular bond. The dashed line represents a harmonic oscillator for small displacements.[McQuarrie, 1983 #293]

displacements, x, from the equilibrium position, x_o. Hence, the potential energy, u, can be approximated by the potential energy of a harmonic oscillator,

$$u = \frac{1}{2}Kx^2 \qquad [3.5]$$

where K is force constant of the bonds and x is the displacement of the atom. Equation 3.5 assumes that the atomic displacement is small for the atoms. The consequences of this assumption will be discussed later.

The derivative of energy with respect to the displacement is equal to the applied force.[Feynman, et al., 1963, 25] Hence, by taking the derivative with respect to x on the right side of equation 3.5, the displacement force can be derived such that:

$$F = \frac{du}{dx} = Kx \qquad [3.6]$$

Therefore, the force to displace an atom is proportional to the displacement of the atom. This equation is a specific case of *Hooke's Law*. If the displacement x corresponds to some reference length l, and the force is applied over a cross sectional area A, then equation 3.6 can be written as:

$$\sigma = E\varepsilon \qquad [3.7]$$

where

$$\sigma = stress = \frac{F}{A} \qquad [3.8]$$

$$\varepsilon = strain = \frac{x}{l} \qquad [3.9]$$

and E, Young's Modulus, is a force constant related to the bonding strength of the solid. A more general form of Hooke's Law, given by equation 3.7, can be written as the following constitutive relation:

$$\sigma_{ij} = C_{ijlm}\varepsilon_{kl} \qquad [3.10]$$

where stress and strain are both second rank tensors and C_{ijlm}, called the elastic or stiffness constants, form a fourth rank tensor.[Kelly and Groves, 1970, 43; Nye, 1957, 74] This equation is used extensively in continuum mechanics where the assumption is made that the media is assumed to be continuous rather than comprised of discrete matter. This assumption is similar to the previous assumption of small atomic displacements. In other words, atomic bonds are not being broken, hence elastic atomic displacements are occurring. Any deformation of the lattice is reversible as long as the stress and strain relation of equation 3.7 does not stray from the elastic regime. That is, the relationship is linear. For this reason, when in the elastic regime, discrete matter can be modeled as continuous media. It is in this regime, as mentioned in the introduction, that this study was conducted.

3.1.3 Vibrational Modes of the Harmonic Oscillator

In the previous section, it was shown that small atomic displacements can be described in terms of continuous isotropic media in the elastic regime. To take advantage of this result, the derivation of harmonic motion and its application to phonons in a crystalline lattice is necessary. The formulation of an alternative and more useful equation of motion begins by equating equation 3.1 to 3.6 such that:

$$ma = -Kx \qquad [3.11]$$

This is the equation of *harmonic* motion. The negative sign denotes an opposing force to the atom's displacement, consequently it is a restoring force. Since acceleration is the second derivative of displacement with respect to time, equation 3.11 can be written as:

$$m\frac{d^2x}{dt^2} = -Kx \qquad [3.12]$$

It can be seen that atomic harmonic displacements are time dependent. Equation 3.12 is a homogeneous linear second order differential equation.[Nagle and Saff, 1989, 65] It can be written as:

$$\frac{d^2x}{dt^2} = -\frac{K}{m}x \qquad [3.13]$$

The general solution of a differential equation of this type (equation 3.13) is a function whose second derivative is the product of itself and a constant. Such a function is the exponential function of the form:

$$x(t) = e^{\pm ibt} \qquad [3.14]$$

where b is a constant to be determined later and i is the *imaginary unit* (i.e., $\sqrt{-1}$). Taking the second derivative of equation 3.14 with respect to time gives:

$$\frac{d^2x}{dt^2} = -b^2x \qquad [3.15]$$

By equating the right hand sides of equation 3.15 and 3.13, one obtains:

$$-b^2x = -\frac{K}{m}x \qquad [3.16]$$

From the physics of harmonic motion, one remembers that the ratio of K to m is the square of the angular frequency, ω.[Feynman, et al., 1963, 25] Therefore, b^2 is the angular frequency, ω. Hence, equation 3.13, written in terms of angular frequency, is:

$$\frac{d^2x}{dt^2} = -\omega^2x \qquad [3.17]$$

which is the formal equation of harmonic motion.

Multiplying both sides of equation 3.16 by m and dividing through by x gives:

$$\omega^2 = \frac{K}{m} \qquad [3.18]$$

Solving for ω, two roots are found:

$$\omega = \pm\sqrt{\frac{K}{m}} \qquad [3.19]$$

The relationship between ω and K in terms of fractions of m is plotted in figure 3.2.

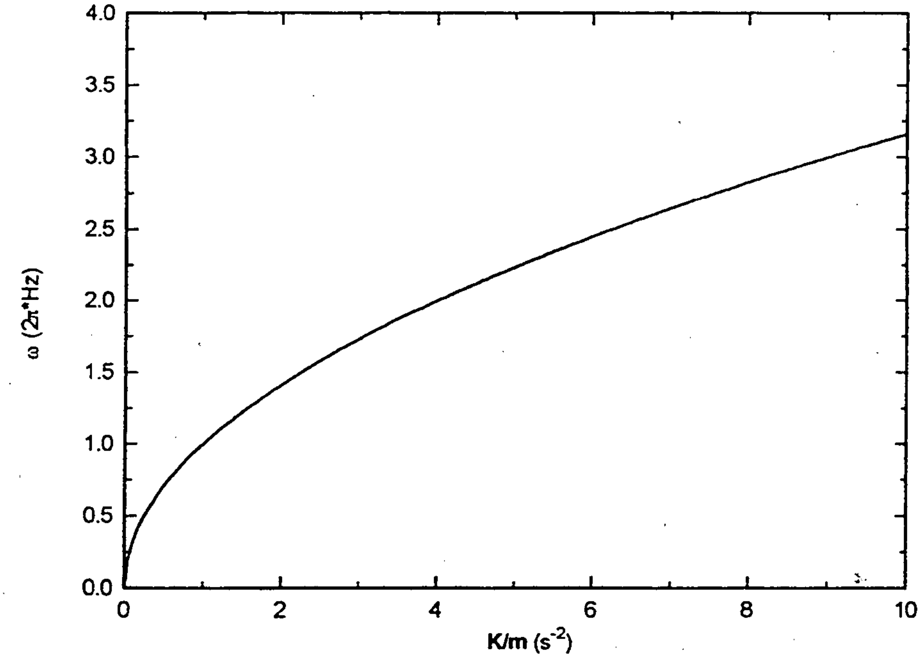

Figure 3.2: Dispersion relation for a harmonic oscillator of mass m and spring constant K.

3.1.4 The Coupled Harmonic Oscillator in a One Dimensional Lattice

In this section, the harmonic oscillator is extended to the system of coupled harmonic oscillators. Furthermore, coupled harmonic motion is applied to a one dimensional Ge lattice. In this case, the <100> direction in Ge will be used. This is convenient for two reasons: first, Ge is monatomic thus only a single mass, m, has to be used (true for any direction), and secondly, for this crystallographic direction, only one spring constant, c, is needed. The other crystallographic directions will be discussed at the end of this section.

In this example, consider a linear chain of atoms (with each atom in its own plane) oriented such that the plane of each atom is perpendicular both to this page and to the chain. Therefore, the distance between each atom is the distance between each plane. Only nearest neighbor interactions within the chain are considered. Atomic displacements are out of plane for a longitudinal wave and in plane for a transverse wave, as shown in figure 3.3. Since the basis of Ge contains two atoms, both atoms have to be considered in terms of displacements relative to their nearest neighbors. An equation of motion is written for each. The displacement in Hooke's Law, given as x in equation 3.6, is actually the difference between the atom's displacement position and its equilibrium position. Hence, x is really Δx, or x_{final}-$x_{\text{equilibrium}}$. In this model, the displacements are given relative to the basis atoms' positions, x_{2r} and x_{2r+1}. Because the basis contains two atoms, the subscript 2 denotes that the basis repeats every other atom. The subscripts, $2r$ and $2r+1$, denote the positions of the first and second basis atom, respectively. The nearest neighbor atomic displacements have the form x_{2r+p}. The subscript, p, designates the number of atoms a specific atom is from the first basis atom's position. Since nearest neighbor interactions, relative to the basis atoms, are only considered here, p is either 2, 1, 0, or -1 as illustrated in figure 3.3. The nearest neighbors of the first basis atom are *2r+1* and *2r-1* while *2r+2* and *2r* are the second basis atom's nearest neighbors. The equations of motion for the given displacements written in the form of equation 3.12 are:

$$m\frac{d^2x_{2r}}{dt^2} = -\left[c(x_{2r} - x_{2r+1}) + c(x_{2r} - x_{2r-1})\right] \qquad [3.20a]$$

$$m\frac{d^2x_{2r+1}}{dt^2} = -\left[c(x_{2r+1} - x_{2r}) + c(x_{2r+1} - x_{2r+2})\right] \qquad [3.20b]$$

where c is the spring or force constant of Ge bonds. Substituting the right hand side of equation 3.17 for the second derivative of x_{2r} with respect to time of equations 3.20a and 3.20b gives:

$$m\omega^2 x_{2r} = -\left[c(x_{2r} - x_{2r+1}) + c(x_{2r} - x_{2r-1})\right] \qquad [3.21a]$$

$$m\omega^2 x_{2r+1} = -\left[c(x_{2r+1} - x_{2r}) + c(x_{2r+1} - x_{2r+2})\right] \qquad [3.21b]$$

Factoring c from the right hand side of the latter equations and combining like terms simplifies equations 3.21a and 3.21b such that:

$$m\omega^2 x_{2r} = c(x_{2r} - x_{2r+1} - x_{2r-1}) \qquad [3.22a]$$

$$m\omega^2 x_{2r+1} = c(2x_{2r+1} - x_{2r} - x_{2r+2}) \qquad [3.22b]$$

Recall that the general solution for a homogeneous linear second order differential equation is a function for which the second derivative is the product of the function and a constant (equation 3.14). In this case, the general solution includes a time dependent and a periodic function. The periodic function introduces, for each interacting plane, the periodicity of the lattice with respect to the lattice vector and the distance between planes. The periodic function has the form:

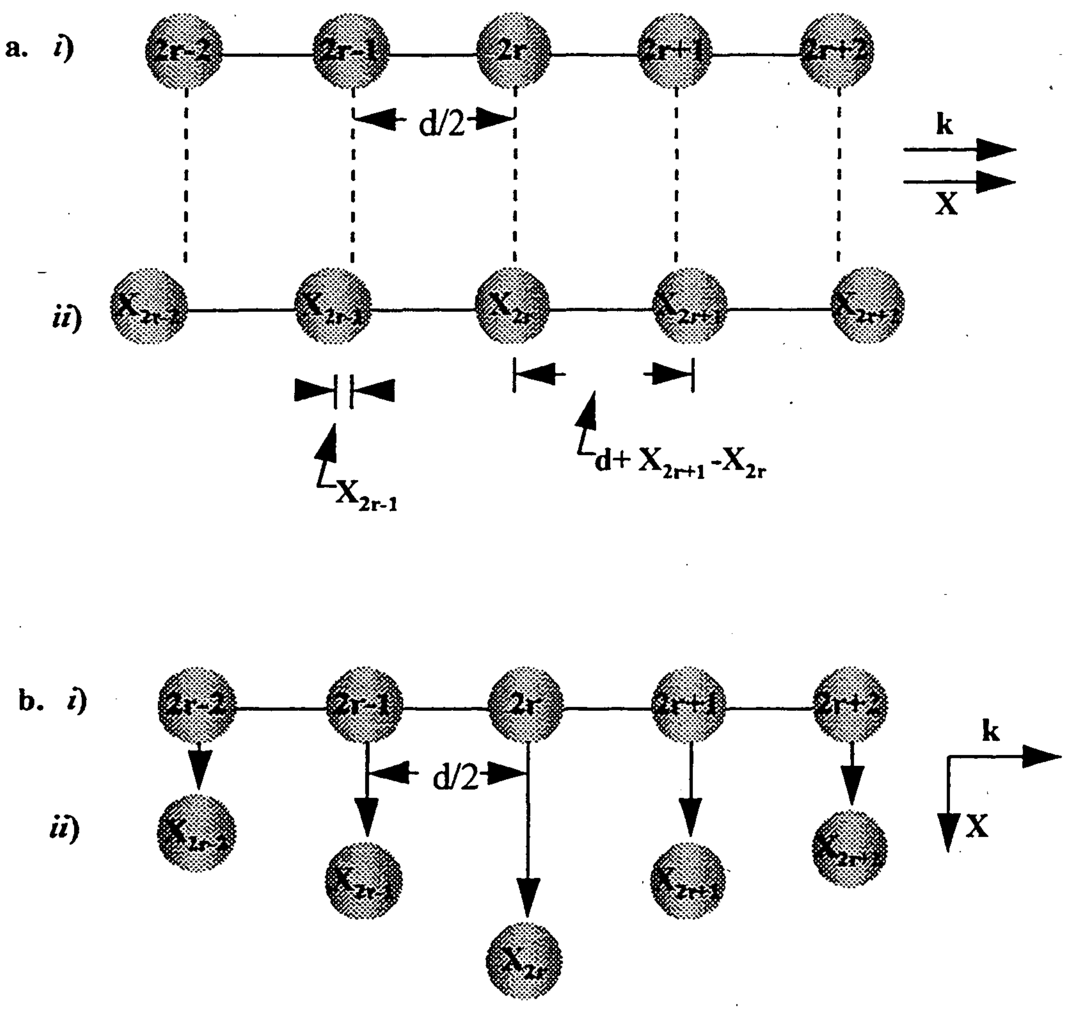

Figure 3.3: **a)** Longitudinal wave displacement is shown as a horizontal shift where ***i)*** shows the equilibrium positions of the atoms and ***ii)*** illustrates the atomic displacements given by $x_{2r\pm p}$. Note that the wave vector $\bar{k}$ is parallel to the displacements $x_{2r\pm p}$. **b)** A transverse wave displacement is shown here where the atoms are vertically displaced relative to the equilibrium positions. The equilibrium atom positions are illustrated by ***i)*** while the atomic displacements are shown by ***ii)***. The wavevector $\bar{k}$ is perpendicular to the displacements $x_{2r\pm p}$.

$$f\left(\bar{k},d\right) = e^{i(2r\pm p)\bar{k}d} \qquad [3.23]$$

where $\bar{k}$ is the reciprocal lattice vector for the traveling wave and d is the distance between planes. The exponential function, given by equation 3.23, is known as a *plane wave*. The general solution, which contains both the time dependent and periodic functions given by equations 3.14 and 3.23, exclusively, is:

$$x_{2r\pm p} = Zxe^{i(2r\pm p)kd} \qquad [3.24]$$

where x is equivalent to equation 3.14. The amplitude, Z, is basis dependent. Thus, the general solutions for x_{2r} and x_{2r+1} are:

$$x_{2r+p} = \alpha xe^{i2rkd}, \ \text{for } p = 0,\ \pm 2 \qquad [3.25a]$$

$$x_{2r+p} = \beta xe^{i(2r+1)kd}, \ \text{for } p = \pm 1 \qquad [3.25b]$$

where α and β are the amplitudes of their corresponding equations, since each plane has its own amplitude.[Kittel, 1986, 44] Substituting equation 3.25a and 3.25b into equations 3.22a and 3.22b, respectively, the following equations are obtained:

$$\begin{aligned} m\omega^2 \alpha xe^{i2rkd} &= c\left(2\alpha xe^{i2rkd} - \beta xe^{i(2r+1)kd} - \beta xe^{i(2r-1)kd}\right) \\ &= cxe^{i2rkd}\left[2\alpha - \beta\left(e^{ikd} + e^{-ikd}\right)\right] \qquad [3.26a] \end{aligned}$$

$$\begin{aligned} m\omega^2 \beta xe^{i(2r+1)kd} &= c\left(2\beta xe^{i(2r+1)kd} - \alpha xe^{i(2r+2)kd} - \alpha xe^{i2rkd}\right) \\ &= cxe^{i(2r+1)kd}\left[2\beta - \alpha\left(e^{ikd} + e^{-ikd}\right)\right] \qquad [3.26b] \end{aligned}$$

The factors xe^{i2rkd} and $xe^{i(2r+1)kd}$ are divided through equations 3.26a and 3.26b, respectively, leaving:

$$m\omega^2\alpha = c\left[2\alpha - \beta\left(e^{ikd} + e^{-ikd}\right)\right] \qquad [3.27a]$$

$$m\omega^2\beta = c\left[2\beta - \alpha\left(e^{ikd} + e^{-ikd}\right)\right] \qquad [3.27b]$$

Using the identity, $2\cos(kd) = e^{ikd} + e^{-ikd}$, these equations reduce to:

$$m\omega^2\alpha = c\left[2\alpha - 2\beta\cos(kd)\right] \qquad [3.28a]$$

$$m\omega^2\beta = c\left[2\beta - 2\alpha\cos(kd)\right] \qquad [3.28b]$$

Combining α and β terms:

$$\alpha\left(2c - m\omega^2\right) - 2c\beta\cos(kd) = 0 \qquad [3.29a]$$

$$2c\alpha\cos(kd) - \beta\left(2c - m\omega^2\right) = 0 \qquad [3.29b]$$

The latter two simultaneous equations in α and β can be solved using the secular equation:

$$\begin{vmatrix} \left(2c - m\omega^2\right) & -2c\ \cos(kd) \\ 2c\ \cos(kd) & -\left(2c - m\omega^2\right) \end{vmatrix} = 0 \qquad [3.30]$$

Taking the determinant of equation 3.30 gives:

$$-\left(2c - m\omega^2\right)^2 + 4c^2\cos^2(kd) = 0 \qquad [3.31]$$

By expanding this equation, one obtains:

$$\omega^4 - \frac{4c}{m}\omega^2 + \frac{4c^2}{m^2}\left[1 - \cos^2(kd)\right] = 0 \qquad [3.32]$$

Using the trigonometric identity, $\sin^2(kd) = 1 - \cos^2(kd)$, equation 3.32 becomes:

$$\omega^4 - \frac{4c}{m}\omega^2 + \frac{4c^2}{m^2}\sin^2(kd) = 0 \qquad [3.33]$$

Hence, the two roots for ω^2 are:

$$\omega^2 = \frac{\frac{4c}{m} \pm \sqrt{\left(\frac{4c}{m}\right)^2 - 4\frac{4c^2}{m^2}\sin^2(kd)}}{2} \qquad [3.34]$$

Factoring and simplifying gives:

$$\omega^2 = \frac{2c}{m} \pm \frac{2c}{m}\sqrt{1-\sin^2(kd)} \qquad [3.35]$$

At k=0, equation 3.35 becomes:

$$\omega^2 = \begin{cases} \dfrac{4c}{m}, \text{ optical branch} \\ 0, \text{ acoustic branch} \end{cases} \text{or} \qquad [3.36].$$

At the edge of the first Brillouin zone (k=π/2d), equation 3.35 becomes:

$$\omega^2 = \frac{2c}{m} \qquad [3.37]$$

for both the acoustic and optical branches. The physical nature of these branches is illustrated in figure 3.5. A comparison of the harmonic oscillator model to the model of one dimensional lattice (i.e., coupled harmonic oscillator) with a two-atom basis shows a definite similarity. The frequency dependence on the square root of the ratio of the force constant and mass (as seen in equations 3.19 and 3.37) differs only by a factor of 2. However, the comparison cannot be extended because the harmonic oscillator lacks spatial periodicity which is intrinsic to the coupled harmonic oscillator.

To determine the validity of the model used to derive the dispersion relation shown in figure 3.4, a comparison of figure 3.4 with experimental data is appropriate. In figure 3.6a, experimental data determined by Nilsson and Nelin is shown.[Nilsson and Nelin, 1971, 67] Using inelastic neutron scattering, they measured the dispersion relation of Ge at 80K in several specific high symmetry crystallographic directions as given on the $\bar{k}$ axis and defined by the first Brillouin zone (BZ) for the diamond cubic lattice shown in figure 3.6b. The model predicted that an acoustic and optical phonon branch from the zone

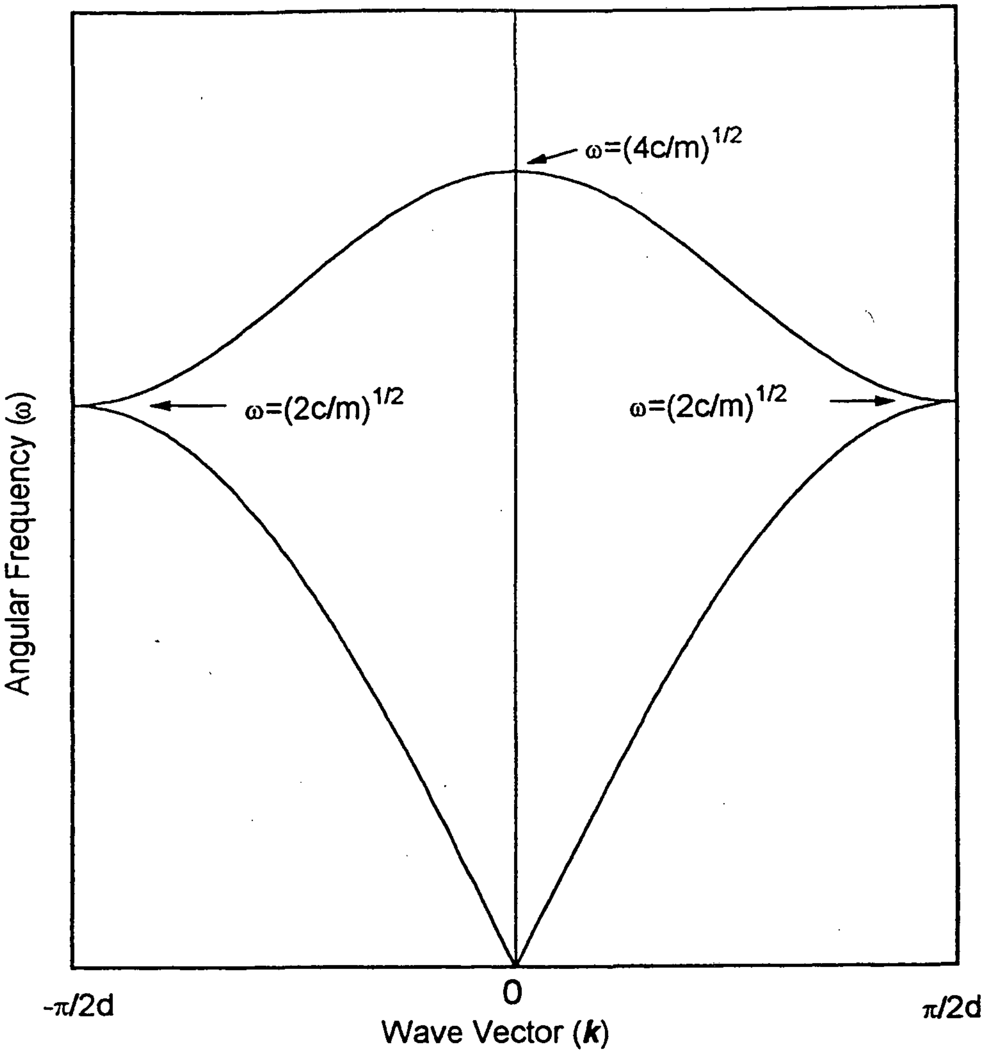

Figure 3.4: Dispersion relation, ω versus k, modeled using nearest neighbor interactions for a monatomic, two-atom basis, cubic crystal lattice in the <100> direction. The crystal structure is diamond cubic.

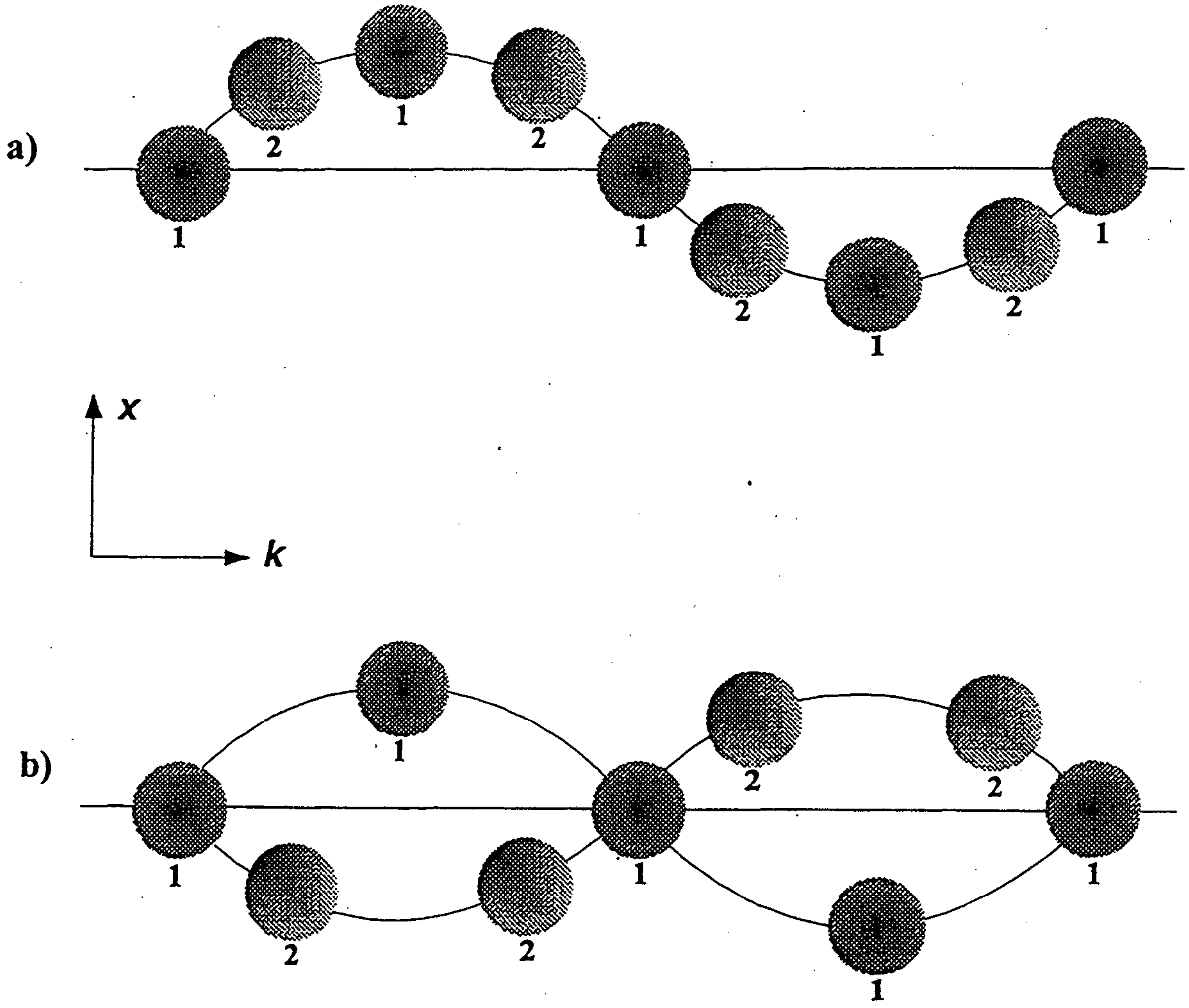

Figure 3.5: The propagation of a transverse wave along a two-atom basis monatomic linear chain. The displacement of the atoms is normal to the wave vector. **a)** Transverse acoustic (TA) phonon mode recognized by the minimum displacement between nearest neighbors. **b)** Transverse optical (TO) phonon mode identified by the opposite displacements between nearest neighbors. The displacements between nearest neighbors is greater for the TO than the TA modes generally leading to a higher frequency range for the TO modes. (fig3_5a.sgx)

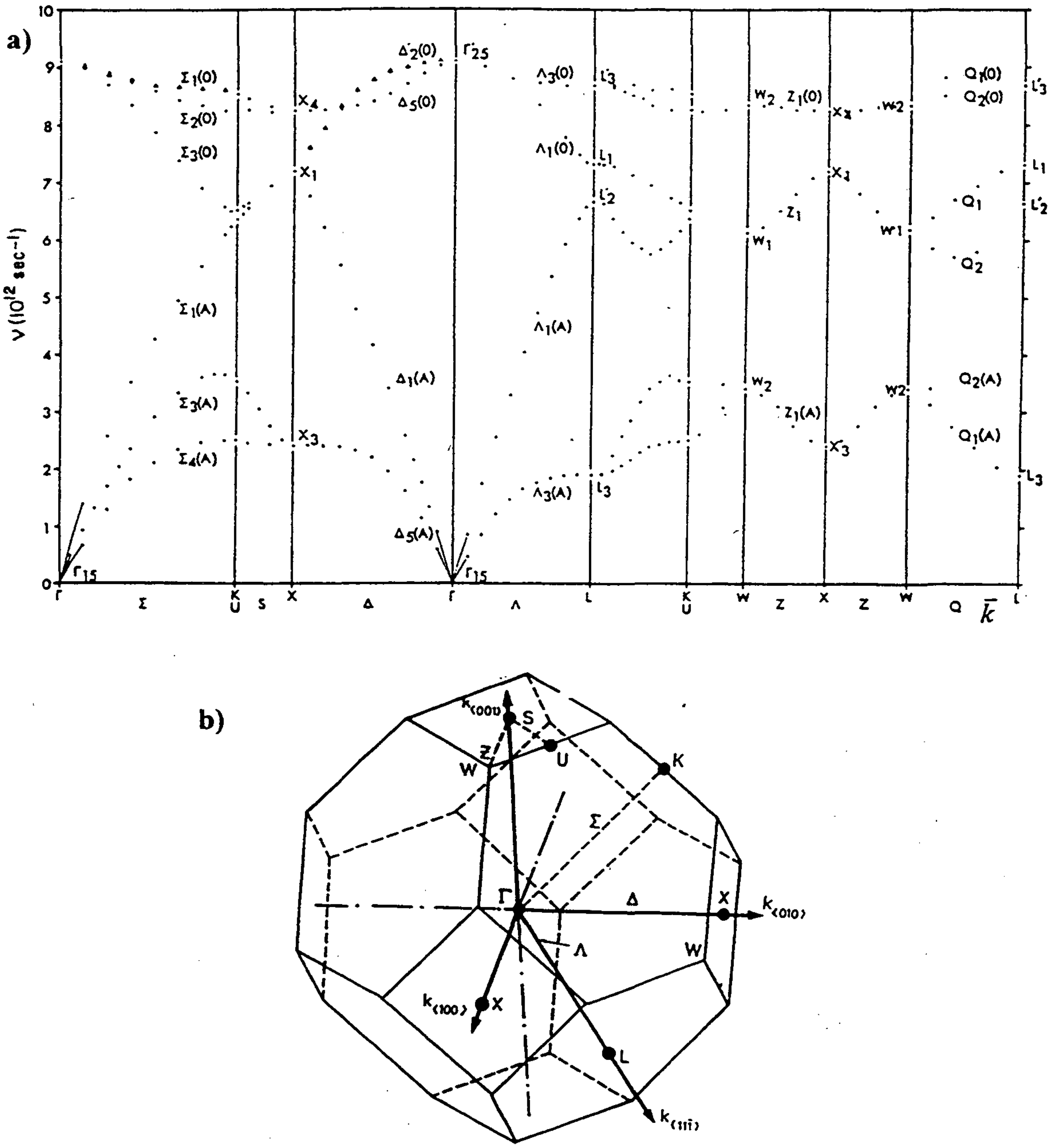

Figure 3.6: **a)** Dispersion relation of phonons in Ge at 80K measured by neutron scattering inelastic. The three principle crystallographic points in the first Brillouin zone are Γ at the zone center, X=2π/a(100), L=2π/a(½½½), and K=U=2π/a(110) where *a* is the lattice constant. The three principle crystallographic symmetry directions are Δ=<100>, Σ=<110>, and Λ=<111>.[Nilsson and Nelin, 1971, 67] **b)** The first Brillouin zone of the diamond cubic lattice showing the principle crystallographic directions, points, and lines. Between monatomic, two-atom basis, diamond cubic lattice model and actual fast neutron dispersion relation of Ge.[Seeger, 1991, 87]

3.1.5 Phonon Scattering Mechanisms

In this study, phonons are used as a probe to determine the amount of phonon transmission through a Ge-Au-Ge eutectic interface. Any impedance (i.e., scattering) to phonon propagation *to* or *from* (<u>not</u> *at*) the interface would diminish the accuracy of the transmission measurement. Hence, phonon scattering mechanisms should be discussed. The dispersion relation, given by figure 3.4, illustrates the allowed frequencies in a perfect crystallographic lattice with a two-atom basis. Any imperfection in the lattice causes a phonon to scatter. Frequency depends on mass, wavevector, lattice spacing and force constant as shown by equation 3.35. Any change in these parameters will cause phonon scattering. Point defects such as vacancies, differing isotopes, and substitutional and interstitial impurities will change the mass and force constant. Lattice imperfections such as dislocations will alter the lattice spacing. Also, crystal boundaries and interfaces will modify the lattice periodicity. Any of the defects just described will also change the wavevector. Phonon-phonon interaction will also change the wavevector. Although both lattice imperfections and phonon scattering mechanisms conserve energy, only phonon-phonon interaction conserves the superposition of the wavevector (i.e., the momentum).[Levinson, 1986, 49] In this thesis, Umklapp processes, that is phonon-phonon interactions that do not conserve momentum, are not considered.[Blakemore, 1985, 8] The temperatures at which phonon experiments are conducted in this study allow the assumption that Umklapp processes are absent.[Blakemore, 1985, 8; Kittel, 1986, 44] In all cases, the above mentioned lattice imperfections and phonon-phonon interaction cause phonons to scatter.[Ashcroft and Mermin, 1976, 3; Ziman, 1972, 113]

3.2 Non-equilibrium Phonon Theory

3.2.1 Introduction

In order to examine the phonon transparency of the eutectic interfaces, the production, use, and imaging of nonequilibrium phonons are necessary. It is therefore substantive to understand the methods by which nonequilibrium phonons are created, the manner in which they propagate, the way they interact in a crystalline lattice, and the means by which they can be imaged. Furthermore, conceptualization of nonequilibrium phonon interaction with the lattice, defects, equilibrium phonons, and interfaces is essential to the analysis and comprehension of the data to be presented.

In this section, several aspects of non-equilibrium phonon phenomena is discussed. Nonequilibrium phonon creation and propagation with respect to lattice interactions is introduced in the first two sections. The effects of crystalline anisotropy on nonequilibrium phonon propagation will follow. In the succeeding section, phonon interfacial scattering is covered. Discussion in the final section centers on phonon imaging.

3.2.2 Nonequilibrium Phonon Excitation Methods

The propagation of nonequilibrium phonons is directly affected by the manner in which nonequilibrium phonons are produced and excited. Nonequilibrium phonon excitation occurs by either indirect or direct methods.[Levinson, 1986, 49]

The direct excitation method utilizes light, $E=\hbar\omega > E_g$, or electrons impinging directly onto the semiconductor surface.[Northrop and Wolfe, 1984, 72] The method of using light produces hot electron-hole pairs near the surface. The relaxation of the hot electron-hole pairs generate nonequilibrium optical and acoustic phonons which have superthermal frequencies. The corresponding energy is much larger ($\hbar\omega_O \gtrapprox 20\,\mathrm{kT}$) than the equilibrium phonon temperature (i.e., bath temperature) which is on the order of ~kT (k=Boltzmann constant).[Bron, 1987, 13; Galkina, 1987, 26; Kazakovtsev and Levinson, 1979, 41; Kazakovtsev and Levinson, 1987, 42] These phonons are known as high excitation-produced nonequilibrium phonons. Temperatures at which experiments are normally conducted (liquid helium temperatures) are low. The amount of equilibrium occupation for these very high frequency phonons is small at these temperatures.[Kazakovtsev and Levinson, 1979, 41] Therefore, the high energy phonons down convert spontaneously to lower frequency phonons.[Levinson, 1980, 48] This is known as *spontaneous decay*. [Bron, 1986, 12; Levinson, 1980, 48; Levinson, 1986, 49] During the down conversion, the nonequilibrium phonons slowly propagate into the bulk. Consequently, highly excited nonequilibrium phonons evolve in both the spatial and frequency domains. As the dynamics of the process reaches a steady state, that is, when either the density of phonon states is large enough to sustain the high energy phonon population, or the nonequilibrium phonon energy is of the order of the equilibrium phonon energy, down conversion subsides. Propagation of nonequilibrium phonons produced by the high excitation method using light occurs by "nonclassical" phonon propagation modes.[Levinson, 1986, 49]

Recently, a direct excitation method using electrons was found to be a low excitation method.[Huebener, et al., 1990, 34] In this method, "classical propagation" of phonons occurs. Both the classical and nonclassical phonon propagation modes are explained in the following paragraph.

The indirect excitation method involves the excitation by electric current through or laser impinging on a metal film evaporated on the semiconductor surface.[Hensel and Dynes, 1977, 31; Hensel and Dynes, 1979, 32; von-Gutfeld and A.H. Nethercot, 1964, 101] Depending on the density of the power transferred to the film, the nonequilibrium phonon frequency (i.e., energy) can either be slightly or significantly above the bath temperature. The latter case involves high excitation-produced nonequilibrium phonons and was explained previously. In the former case, low excitation nonequilibrium phonons are produced. They evolve spatially but not in the frequency domain. Low excitation nonequilibrium phonons propagate by "classical" propagation modes.[Kazakovtsev and Levinson, 1979, 41; Levinson, 1986, 49] At liquid helium temperatures and below, the pulsed metal film reaches a temperature in the range of 5K to 10K. The phonons emitted from the metal film are incoherent and show a Planck energy distribution with the peak slightly lower than the metal temperature.[Hensel and Dynes, 1977, 31; Northrop and Wolfe, 1980, 71; Northrop and Wolfe, 1984, 72; Weis, 1969, 104]

3.2.3 Nonequilibrium Phonon Modes of Propagation

To determine the degree of phonon interfacial transparency, phonon scattering before and beyond the interface must be minimal. If an extensive amount of scattering were to occur by means other than the interface, the amount of scattering via the interface can not be easily determined. As discussed in section 3.1.5, phonon scattering is caused by lattice imperfections and other phonons. Since the amount of phonon scattering dictates phonon propagation, the type of phonon propagation present during the experiment is important. Therefore, a discussion of phonon propagation modes is warranted.

Low level and high level excitations create classical and nonclassical phonon propagation modes, respectively. In the experiments described in this thesis, the generated nonequilibrium phonons propagate mainly by the classical modes which will be described in detail. Several nonclassical propagation modes will be briefly discussed.

Ballistic, *diffusion*, *heat conduction*, and *second sound* modes are the four types of classical propagation modes.[Beck, et al., 1974, 6; Kazakovtsev and Levinson, 1979, 41; Levinson, 1986, 49] These modes are best described by scattering time which is the time period between scattering events. The phonon-phonon scattering time, τ_p, varies by the inverse of frequency to the fifth power. The lattice imperfection scattering time, τ_i, (i.e., time taken for propagation modes to be scattered by lattice imperfections) varies with the inverse of frequency to the fourth power. τ_p and τ_i can be expressed by the following equations:

$$\tau_p = \gamma\omega_D\left(\frac{\omega}{\omega_D}\right)^{-5} \qquad [3.38b]$$

$$\gamma \approx \frac{\omega_D}{M_o v_p^2} \qquad [3.38b]$$

$$\tau_i = \eta\omega_D\left(\frac{\omega}{\omega_D}\right)^{-4} \qquad [3.39a]$$

$$\eta = Na_o^3\delta \qquad [3.39b]$$

where ω_D is the Debye frequency, M_o is the unit cell mass, v_p is the phonon phase velocity, a_o^3 is the unit cell volume, and ω is the nonequilibrium phonon frequency.[Kazakovtsev and Levinson, 1987, 42; Levinson, 1980, 48; Maris, 1990, 56] The density of impurities is denoted by N where Na_o^3 is the fraction of imperfect unit cells and δ is the amount of unit cell distortion due to an impurity.

Scattering which occurs at the interface must be detectable to determine the degree of interface transparency. Additionally, phonon scattering on either side of the interface (i.e., in the bulk) must be minimal in order to measure interfacial scattering. Therefore, the scattering times are compared to the travel times from phonon source to eutectic interface, t_e, and interface to detector, t_d. To simplify the description, assume that t_e=t_d and t_e is given by:

$$t_e = \frac{L}{v} \qquad [3.40]$$

where L is the distance from the point source to the eutectic interface. The parameter, v, is called either the average phase velocity or the group velocity of the propagating phonon mode, depending on the reference.[Bron, 1986, 12; Bron, 1987, 13; Levinson, 1986, 49]

Phonons that propagate without being scattered in the bulk are called *ballistic*. Both the phonons which reach the interface unhindered and those that depart the interface and arrive at the detector unhindered are therefore *ballistic* phonons (disregarding interfacial scattering). Thus, t_e is much less than both τ_p or τ_i. For the ballistic case, the condition is:

$$t_e << \tau_p, \tau_i \qquad [3.41]$$

Propagation of phonons is *diffusive* if the phonons are scattered many times before they reach the eutectic interface by impurities (Rayleigh scattering) but not by other phonons. The condition for the diffusive propagation mode is:

$$\tau_i << t_e << \tau_p \qquad [3.42]$$

The classical phonon propagation mode termed *second sound* occurs if phonon-phonon interaction is predominant. Hence, the second sound case is the opposite of the diffusive case and is given by the condition:

$$\tau_p << t_e << \tau_i \qquad [3.43]$$

For the *heat conduction* propagation mode, scattering is dominated by either phonons or impurities depending on crystal purity. For "pure" crystals, phonon scattering dominates which gives the condition that:

$$\tau_p << \tau_i << t_e \qquad [3.44]$$

If the crystal is impure, impurity scattering dominates over phonon scattering and the following condition holds:

$$\tau_i << \tau_p \qquad [3.45]$$

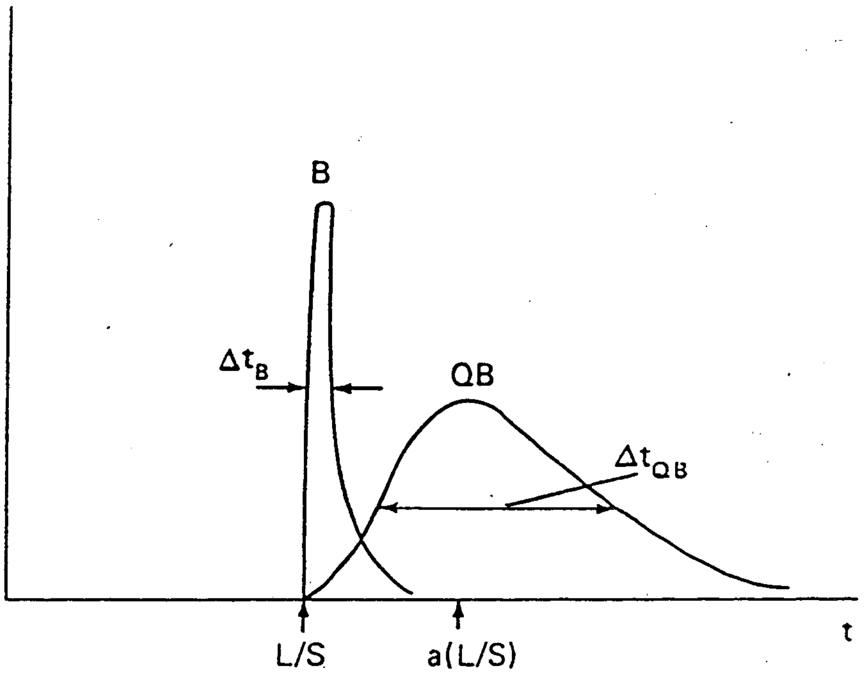

Figure 3.7: Known as "time of flight" spectra, this would not be possible without the ability to do heat pulse experiments. The detector signal labeled B is for the ballistic case while QB is for the quasiballistic case. The ballistic signal length, Δt_B, is small and determined by the detector size and response time (i.e., detector resolution). The quasiballistic signal, Δt_{QB}, is proportional to the arrival time, L/s, where *s* is the phonon velocity. The constant of proportionality, *a*, depends on what point the pulse is monitored (e.g., pulse peak or leading edge half-height).[Levinson, 1986, 49]

However, the relation between the phonon scattering time, τ_p, and the propagation time from phonon source to interface, t_e, varies. They can either be similar or one can dominate over the other.

In the regime of high excitation by direct means, several nonclassical propagation modes exist. However, to keep the subject within the realm of this thesis, only two propagation modes are briefly mentioned. In the case of high excitation, spontaneous decay occurs. If, in the case of low excitation where ballistic propagation exists and high excitation occurs, ballistic propagation is accompanied by spontaneous decay. This is referred to as *quasiballistic* propagation and is illustrated in figure 3.7.[Levinson, 1986, 49]

The other high excitation produced propagation mode is called *quasidiffusion*. If the condition of propagation by diffusion is apparent for low excitation, then diffusion propagation is accompanied by spontaneous decay during high excitation. This is quasidiffusion.[Bron, 1984, 11; Kazakovtsev and Levinson, 1979, 41; Levinson, 1986, 49] Although the quasidiffusion regime of phonon propagation is not disputed, there is some question as to the validity of several assumptions made to develop this propagation model.[Maris, 1990, 56; Shields, 1992, 89] However, this is beyond the scope of this thesis and will not be discussed here.

3.2.4 Phonon Focusing

As a consequence of heat pulse methods,[Pomerantz and Gutfeld, 1968, 80; von-Gutfeld, 1968, 100; von-Gutfeld and A.H. Nethercot, 1964, 101] time of flight experiments (see figure 3.7) performed at liquid helium temperatures in pure single crystals give rise to ballistic phonon propagation where the condition given by equation 3.41 holds. Moreover, the scattering length of phonons is at least as long as L described in equation 3.40. At such low temperatures, phonon frequencies are in the linear region of the acoustic modes. It is in this environment that phonon focusing arises, and it is in this temperature region where phonon experiments in this study were performed. Therefore, in order to understand the experimental results in this study, the phenomenon of *phonon focusing* must be comprehended.

First described by Taylor *et al.*, phonon focusing is an effect due to the anisotropy of a crystalline solid.[Taylor, et al., 1969, 94] Unlike the isotropic distribution of energy during heat conduction in a solid, the energy flux of ballistic, quasiballistic, and quasidiffusive phonons are channeled or *focused* in specific directions. The focusing of phonons is seen because the amount of phonon scattering does not diffuse and randomize the phonon energy flux, and so the anisotropic effects are seen.

There are several ways to conceptualize that phonon focusing is due to anisotropy. Consider the solution of the dispersion relation for a two-atom basis, monatomic, linear chain which depends on the lattice plane spacing, d (see equation. 3.35). For a cubic crystal lattice, d is given by:

$$d = \frac{a}{\sqrt{h^2 + k^2 + l^2}} \qquad [3.46]$$

where a is the lattice constant, (hkl) are the Miller indices, and the denominator is proportional to the magnitude of the vector normal (only in cubic systems) to the plane.[Cullity, 1978, 18] The vector gives the direction of the planes. The phonon frequency, ω, is dependent on the lattice spacing, d (see equation 3.35). The group and phase velocities are a function of ω (equations 3.3 and 3.4). Therefore, the phonon velocities are dependent on the crystallographic direction. Since the group velocity is fundamentally the gradient of the energy in k-space and their vectors are collinear, it follows that the energy flux is also dependent on the crystallographic direction. This means the energy flux will be increased or focused in certain directions and reduced in other specific directions.[McCurdy, et al., 1970, 58; Taylor, et al., 1969, 94; Taylor, et al., 1971, 95] Consequently, as alluded to at the beginning of this section, for a spherical distribution of wavevectors ($\bar{k}$) emitted by a phonon source, the group velocity (v_g) generally does not directionally coincide with the wavevector or the phase velocity (v_p). [Taylor, et al., 1969, 94] This is depicted in figure 3.8. As can be seen, the group velocity vectors are generally not collinear with the spherically distributed wavevector.

Similar to a Wulff plot, a constant frequency or $\omega(\bar{k})$ plot is shown in figure 3.9a. This is a cross sectional slice of a three dimensional plot of the slow transverse mode in (100) Ge. The boundary or surface is called a sheet.[Northrop and Wolfe, 1984, 72] Since there are three polarizations, longitudinal acoustic (LA), fast transverse acoustic (FTA), and slow transverse acoustic (STA), there are three corresponding sheets. Figure 3.9a shows that the frequency distribution varies with a spherical distribution of the

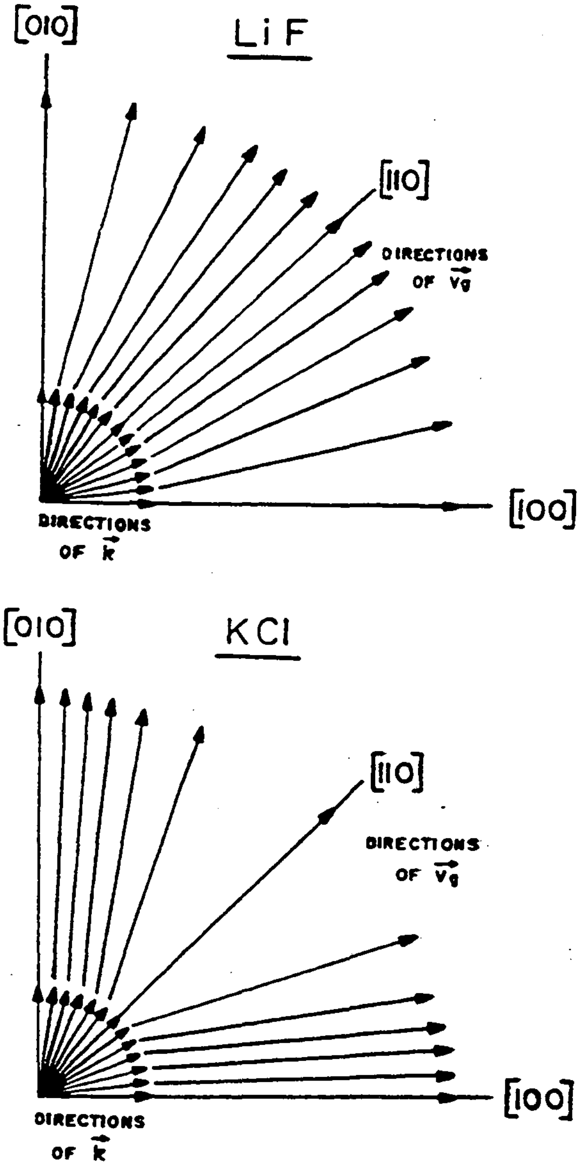

Figure 3.8: The phonon focusing effect for both LiF and KCl. Each shows a isotropic distribution of $\vec{k}$ not necessarily parallel with the corresponding v_g vectors.[Taylor, et al., 1969, 94]

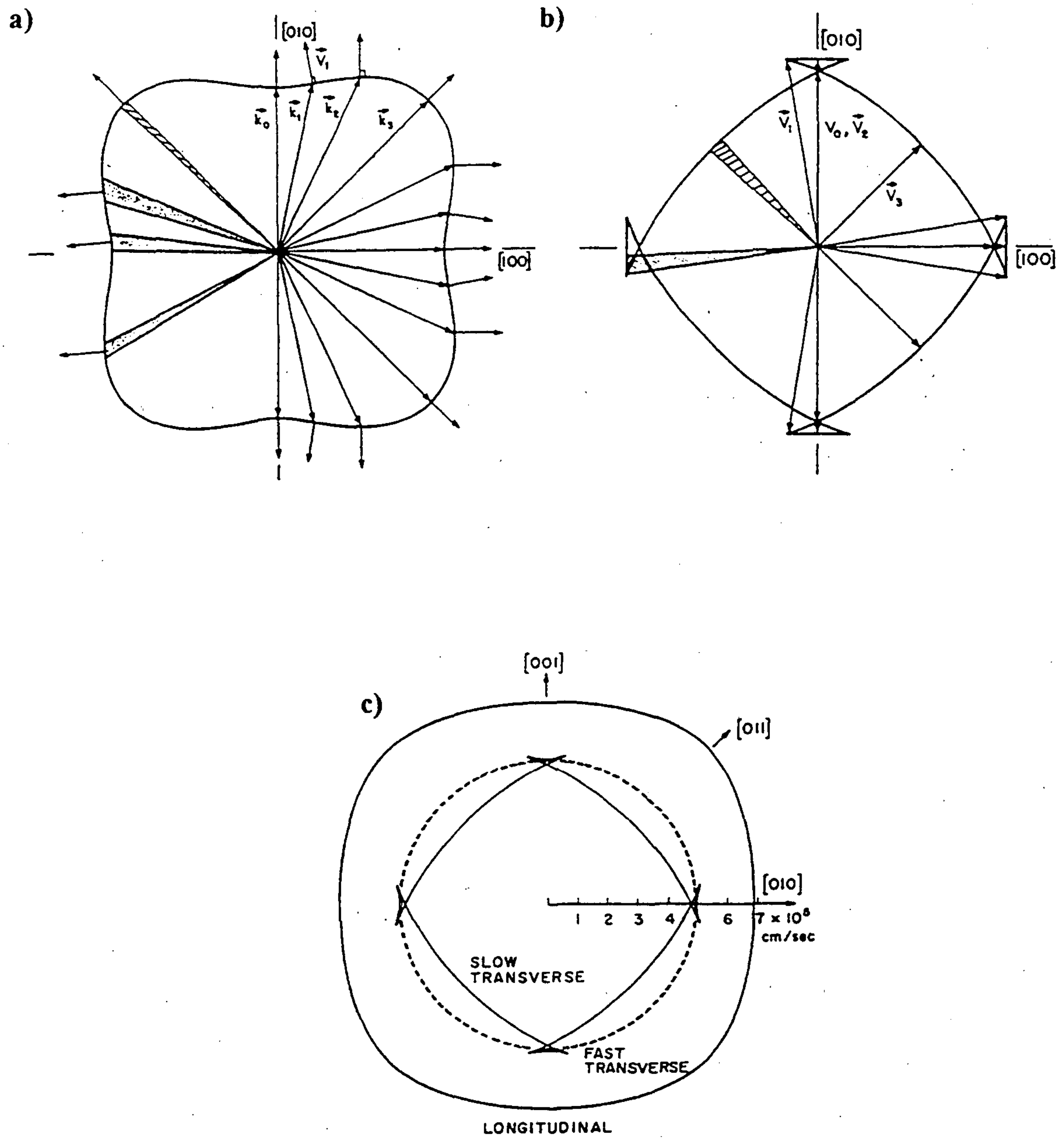

Figure 3.9: **a)** A cross section of the constant frequency surface for the slow TA mode in the (001) plane of Ge. **b)** The corresponding group velocities for the $\vec{k}$ vectors given in (a).[Northrop and Wolfe, 1980, 71] **c)** A cross section of the group velocity surface of (100) LiF. Note the different velocities for the three polarizations.[Taylor, et al., 1971, 95]

wavevectors. However, the magnitudes of $\bar{k}$ varies with direction. Furthermore, the group velocity is perpendicular to the constant frequency surface. This again illustrates the fact that often $\bar{k}$ and v_g are not collinear.

To analytically describe phonon focusing, continuum elasticity theory, which assumes small atom displacements, must be revisited. Suppose that nonequilibrium phonons are produced by a low excitation method (see sec. 3.2.2). The phonons are near the bath temperature. If the bath temperature is between 1K and 4K, the nonequilibrium phonon frequency is between 100 GHz and 1 Thz.[Kittel, 1986, 44] For germanium, the dispersion relation (figure 3.6) indicates that these frequencies are near $\bar{k}=0$. From section 3.1.1, the magnitude of $\bar{k}$, k, is $2\pi/\lambda$; consequently, $\lambda=2\pi/k$. From figure 3.6a, 1 THz in the <111> (along the Λ direction) corresponds to about $0.2k_{max}$. Hence, the wavelength is $40d$ (equation 3.46). Therefore, the phonon wavelengths are much larger than d. This result gives rise to the relation:

$$\lambda>>d \tag{3.47}$$

which is known as the *long wavelength approximation*. In this approximation, the medium is assumed to be continuous. Therefore, elasticity theory or continuum mechanics can be used and the lattice vibrations can be treated as elastic waves.[Maris, 1971, 54]

Additionally, in the long wavelength approximation as in the Debye approximation, the velocity of sound is assumed to be constant for each polarization type (i.e., transverse or longitudinal).[Kittel, 1986, 44] Since $k=\dfrac{2\pi}{\lambda}$, then:

$$kd\to 0 \tag{3.48}$$

The acoustic solution of the dispersion relation can now be written as:

$$\omega \approx \left| \frac{kd}{2} \right| \qquad [4.49]$$

Accordingly, the angular frequency is directly proportional to the magnitude of the wavevector. That is, the group velocity, given by equation 3.4, is constant, as is the phase velocity. This is easily seen by examining the dispersion relation in the range of 1 Thz and below. In this range, the dispersion curve is linear. The group velocity, which is the change in angular frequency with respect to the wavevector, is just the slope of the line. The slope is constant, therefore the group velocity is constant.

Classical elastic continuum theory, by virtue of the long wavelength approximation, allows one to model media as continuous but anisotropic; moreover, lattice vibrations can be treated as elastic waves.[Wolfe, 1980, 109] Usually when a medium is assumed to be continuous, it is also assumed to be isotropic. For measurements of thermal conductivity, this assumption is valid because phonons propagate diffusively (see section 3.2.3), so the scattering length is much shorter than the sample size.[Little, 1959, 51] But in the ballistic regime, the scattering length is of the order of the sample dimensions and phonons will travel without scattering.

The nonspherical symmetry of the $\omega(\bar{k})$ plot, depicted in figure 3.9a and also known as the *slowness surface*, illustrates that the phase velocity (ω/k) is anisotropic. The concave regions of the constant ω surface "focuses" the energy flux (and $\boldsymbol{v}_g$) in the <100> directions. Two $\boldsymbol{v}_g$ vectors exist on either side of the <100> directions which focus onto the same point in space. Where the curvature is small, the energy flux is enhanced.

The energy flux also differs for each polarization because the group velocity will vary according to the polarization.[Taylor, et al., 1971, 95] The gradient of the slowness surface is shown in figure 3.9c. This cross section of the v_g-surface of {100} LiF shows the v_g of each polarization.

Maris developed an analytical expression to quantify the enhancement of the energy flux.[Maris, 1971, 54; Maris, 1986, 55] He called this term the *enhancement factor* which can be described as the ratio of a solid angle in k-space to a solid angle in v_g-space. Suppose a phonon detector whose center's perpendicular unit vector, $\boldsymbol{n}$, is directed toward a phonon point source. If the detector is subtended by a solid angle $\Delta\Omega_d$, as shown in figure 3.10a, then, for an isotropic solid, the wavevectors of elastic waves from the source lying within this solid angle will arrive at the detector. The solid angle $\Delta\Omega_d$ is equal to $(\delta k/k)^2$.

The following condition:

$$\bar{v}_g\left(\bar{k}j\right)\|\bar{n} \qquad [3.50]$$

must be added and satisfied for an elastic wave with polarization j to propagate in an anisotropic rather than isotropic medium. If this condition is true for several elastic waves produced by the phonon source (i.e., $\bar{k}$ is parallel to $\boldsymbol{n}$), then the wavevectors of those elastic waves will be within the solid angle $\Delta\Omega_k$ and will reach the detector. Hence, the enhancement factor compares the number of wavevectors in the solid angle between an isotropic versus an anisotropic solid and is given by:

$$A = \frac{\Delta\Omega_k}{\Delta\Omega_d} \qquad [3.51]$$

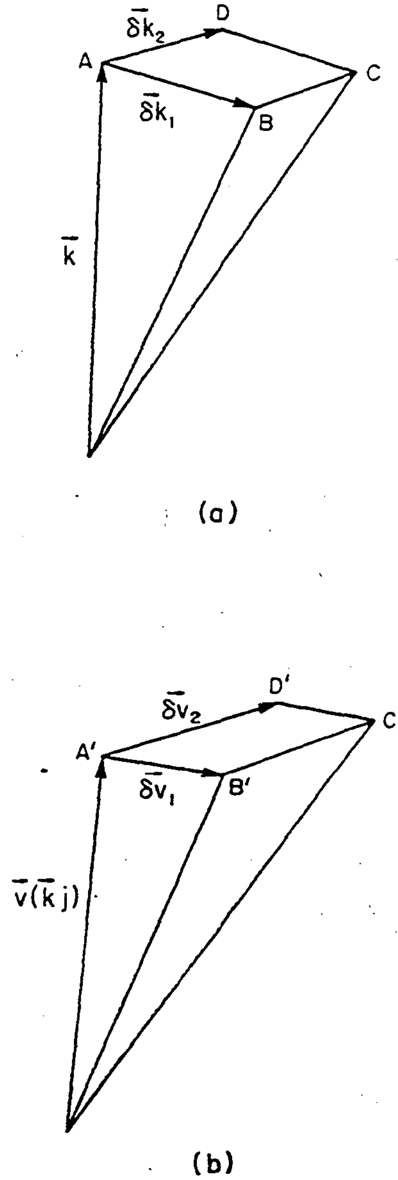

Figure 3.10: **a)** The k-space solid angle is $\Delta\Omega_k$ and is defined as infinitesimal. ABCD is a parallelogram. The $\delta\bar{k}$'s are much smaller than $\bar{k}$ where $\delta\bar{k}_1=\delta k \boldsymbol{n}_1$ and $\delta\bar{k}_1=\delta k \boldsymbol{n}_1$. The solid angle $\Delta\Omega_k$ can be mapped to $\boldsymbol{v}_g$-space. **b)** The $\boldsymbol{v}_g$-space solid angle is $\Delta\Omega_v$. [Maris, 1971, 54]

For example, the solid angle $\Delta\Omega_k$ is shown as three solidly shaded wedges or areas in figure 3.9a. The three $\Delta\Omega_k$'s map to v_g-space as only one solid angle $\Delta\Omega_v$, shown in figure 3.9a, because $\Delta\Omega_v$ crosses the constant v_g surface three times. Hence, in this direction, the energy flux is enhanced (A~1) as a result of the concavity and asymmetry of the constant $\omega(\bar{k})$ surface. An example of defocusing is shown in figures 3.9a and 3.9b as the hatch-marked wedges. Only one $\Delta\Omega_k$ maps to one $\Delta\Omega_v$, so $\Delta\Omega_v$ crosses the constant v_g plot only once so $A<1$.

As mentioned in the beginning of this section, due to the long wavelength approximation, phonons can be treated as elastic waves in an anisotropic medium. Consequently, anisotropic phonon propagation has been mathematically treated using classical elastic continuum theory.[Miller and Musgrave, 1956, 60; Musgrave, 1954, 61; Musgrave, 1954, 62; Musgrave, 1959, 63] The following discussion connects elasticity theory with the enhancement factor (A). The core of the discussion follows that of Northrop and Wolfe.[Northrop, 1982, 69; Northrop and Wolfe, 1980, 71]

The constitutive relation (equation 3.10) is the essence of elasticity theory. The fourth rank elastic constant tensor, C_{ijlm}, can be reduced from 81 independent constants to just 21 for any crystal using symmetry arguments and indices transformations.[Nye, 1957, 74] In crystals with cubic symmetry, the number of independent constants can be further reduced. If the axes of reference are chosen to be parallel to the crystal axes x_1, x_2, and x_3, which are respectively parallel to [100], [010], and [001], then the following relations occur:

$$C_{11} = C_{22} = C_{33},\ C_{12} = C_{23} = C_{31},\ C_{44} = C_{55} = C_{66} \quad [3.52]$$

giving rise to just 3 independent constants.[Kelly and Groves, 1970, 43] They are generally written as C_{11}, C_{12}, and C_{44}.

If the vector of a displaced atom's position is $r(\bar{x}) \equiv (r_x, r_y, r_z)$ where the equilibrium position is denoted by the vector $\bar{x} = (x_1, x_2, x_3) = (x, y, z)$, the affiliated strain is:

$$e_{lm} = \frac{\partial r_l}{\partial x_m} \qquad [3.53]$$

where $\varepsilon_{lm}=½(e_{lm}+e_{ml})$, and the indices are the same as in equation 3.10.[Kelly and Groves, 1970, 43] Similar to the derivation performed in section 3.1.4, by taking the gradient of stress, the determination of the equation of motion for an elastic wave is:

$$\rho \frac{\partial^2 r}{\partial x^2} = \frac{\partial \sigma_{ij}}{\partial x_j} = C_{ijlm} \frac{\partial^2 r}{\partial x_j \partial x_m} \qquad [3.54]$$

Rather then using the mass of an atom as was done in equation 3.20, the crystal density ρ is used. The general solution to this equation of motion is the same as that given by equation 3.24. In this case, the phonon polarization, $\bar{\chi}$, replaces the wave amplitude, and the vector $\boldsymbol{x}$ replaces d: The general solution is given by:

$$\bar{r} = \bar{\varepsilon} r e^{i(\bar{k} \cdot \bar{x})} \qquad [3.55]$$

where r (equation 3.14) is $e^{-i\omega t}$. By substituting equation 3.55 into 3.54 and following the method to solve simultaneous equations of motion given in section 3.1.4, an eigenvalue equation is produced with the form:

$$\left(C_{ijlm} k_j k_m - \rho \omega^2 \xi_{il}\right) \chi_l = 0 \qquad [3.56]$$

By dividing by $\rho|\bar{k}|^2$ and using the definition of the unit vector of $\bar{k}$ and the magnitude of the phase velocity (v_p) both given in equation 3.3, equation 3.56 reduces to:

$$\left(D_{ij} - v_p^2 \xi_{il}\right)\chi_l = 0 \qquad [3.57a]$$

$$D_{ij} = \frac{C_{ijlm} n_j n_m}{\rho} \qquad [3.57b]$$

Equation 3.57a is the Christoffel equation where D_{ij} are the Christoffel elastic coefficients (i.e., the Christoffel tensor). [Every, 1979, 21; Musgrave, 1954, 61; Musgrave, 1954, 62; Musgrave, 1970, 64; Northrop and Wolfe, 1980, 71] This can be solved in terms of the phase velocity by using the form of the secular equation as shown in equation 3.30. The expansion of the secular equation will give a cubic equation in v_p. Each root is associated with an acoustic polarization. Since there are three roots, there will be three orthogonal polarizations for each value of $\bar{k}$. The polarizations are generally identified as LA, FTA, and STA.

The frequency of an elastic wave is given by:

$$\omega = v_p(\theta_k, \phi_k)k \qquad [3.58]$$

for a given wavevector direction $\bar{k} = (k, \theta_k, \phi_k)$. By differentiating equation 3.58, the group velocity, given by equation 3.4, is derived in the following form:

$$\bar{v}_g = \nabla_k \omega = \left(v_p - \bar{n} \cdot \frac{\partial v_p}{\partial \bar{n}}\right)\bar{n} + \frac{\partial v_p}{\partial \bar{n}} \qquad [3.59]$$

where $\frac{\partial v_p}{\partial \bar{n}}$ can be found by implicit differentiation of the secular equation of equation 3.57.[Every, 1979, 21]

The direction of the energy flux depends on $\left(\theta_{v_g}, \phi_{v_g}\right)$. As mentioned previously, the direction of the energy flux is parallel to (θ_k, ϕ_k), which is the direction of $\boldsymbol{v_g}$. In order to map $\boldsymbol{v_g}$-space, $\left(\theta_{v_g}, \phi_{v_g}\right)$, to $\bar{k}$-space, (θ_k, ϕ_k), the following transformation is used:

$$\cos\left(\theta_{v_g}\right) = f(\cos\theta_k, \phi_k) \text{ and } \phi_{v_g} = g(\cos\theta_k, \phi_k) \qquad [3.60]$$

The Jacobian of the functions f and g, which are obtained from the components of $\boldsymbol{v_g}$, is given by:

$$d\Omega_v = d\left[\cos\left(\theta_{v_g}\right)\right] d\phi_{v_g} = Jd\left[\cos(\theta_k)\right] d\phi_k = Jd\Omega_k \qquad [3.61]$$

which is the ratio of the product of differentials in the two spaces. Also:

$$J \equiv \det\begin{vmatrix} \dfrac{\partial f}{\partial[\cos(\theta_k)]} & \dfrac{\partial f}{\partial\theta_k} \\ \dfrac{\partial g}{\partial[\cos(\theta_k)]} & \dfrac{\partial g}{\partial\theta_k} \end{vmatrix} \qquad [3.62]$$

Equation 3.62 gives rise to the enhancement factor, A, given by equation 3.50. The enhancement factor is just the inverse of the magnitude of $\boldsymbol{J}$:

$$A \equiv \left|\frac{\Delta\Omega_k}{\Delta\Omega_k}\right| = \frac{1}{|J|} \qquad [3.63]$$

As stated previously, the enhancement factor can be used to determine the direction in which the energy flux intensity is focused or defocused. According to Rösch and Weis, the enhancement factor can be mathematically infinite in certain directions, but it is integrable. The inflection point an a constant frequency plot is one of those directions. For example, A diverges at such a point in figure 3.9a shown by the intersection of $\bar{k}_1$ and v_{gl} on the (001) Ge slowness surface cross section.

3.2.5 Phonon Spectroscopy and Imaging in Ge

With the advent of heat pulse experiments at low temperatures, initially carried out by von Gutfeld and Nethercot in 1964, phonon spectroscopy was established.[Pomerantz and Gutfeld, 1968, 80; von-Gutfeld, 1968, 100; von-Gutfeld and A.H. Nethercot, 1964, 101] In the heat pulse method, electrical or laser pulses, on the order of 10^{-7} s, are incident on a metal film deposited on a dielectric crystal surface.[Viswanathan, 1987, 99] The sample configuration is shown in figure 3.11.

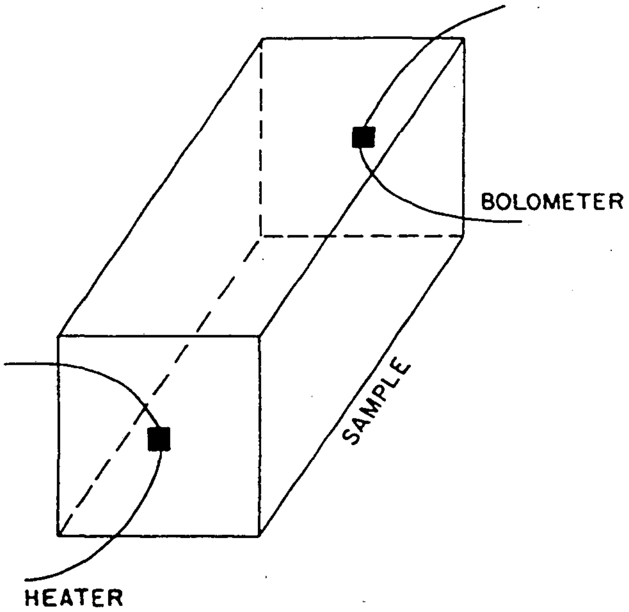

Figure 3.11: Sample configuration for the heat pulse method. (p.7) [Bron, 1984, 11]

The amount of phonon excitation occurring in the metal film during heat pulsing is low; subsequently, only nonequilibrium phonons just above the bath temperature are produced (see section 3.2.2). If the scattering length is on the order of the distance, *L*, from the metal film to the detector, then the mode of propagation is ballistic. The detector, typically a transition edge detector, produces spectra as shown in figure 3.12a. If diffuse propagation is prevalent (the condition given by equation 3.42), then the scattering length is shorter than *L*. In this case, the heat pulse spectrum looks similar to the spectrum in figure 3.12b. Figure 3.13a shows the effect of varying the excitation levels. Isotope scattering occurs for the higher frequency phonons produced by higher excitation. Heat pulses in dislocation free and dislocated LiF produce spectra shown in figure 3.13b illustrating the difference between ballistic and diffuse phonon propagation where the latter results from scattering caused by deformation. Another example of phonon spectroscopy is illustrated in figure 3.13c where heat pulses in pure NaF at various temperatures demonstrate the result of second sound. For the second sound condition, given by equation 3.43, phonon-phonon interactions are prevalent. In this case, the equilibrium phonons scatter the heat pulse-produced nonequilibrium phonons. These examples illustrate that phonon spectroscopy is a tool which can be used to determine the occurrence and type of scattering.

In 1979, Northrop and Wolfe extended the idea of acquiring one spectrum of bolometer intensity versus time after one heat pulse from a fixed phonon source.[Northrop and Wolfe, 1979, 70] They did so by making the previously fixed phonon source mobile. Rather than electrically pulsing a metal film, they rastered a pulsing laser across a metal

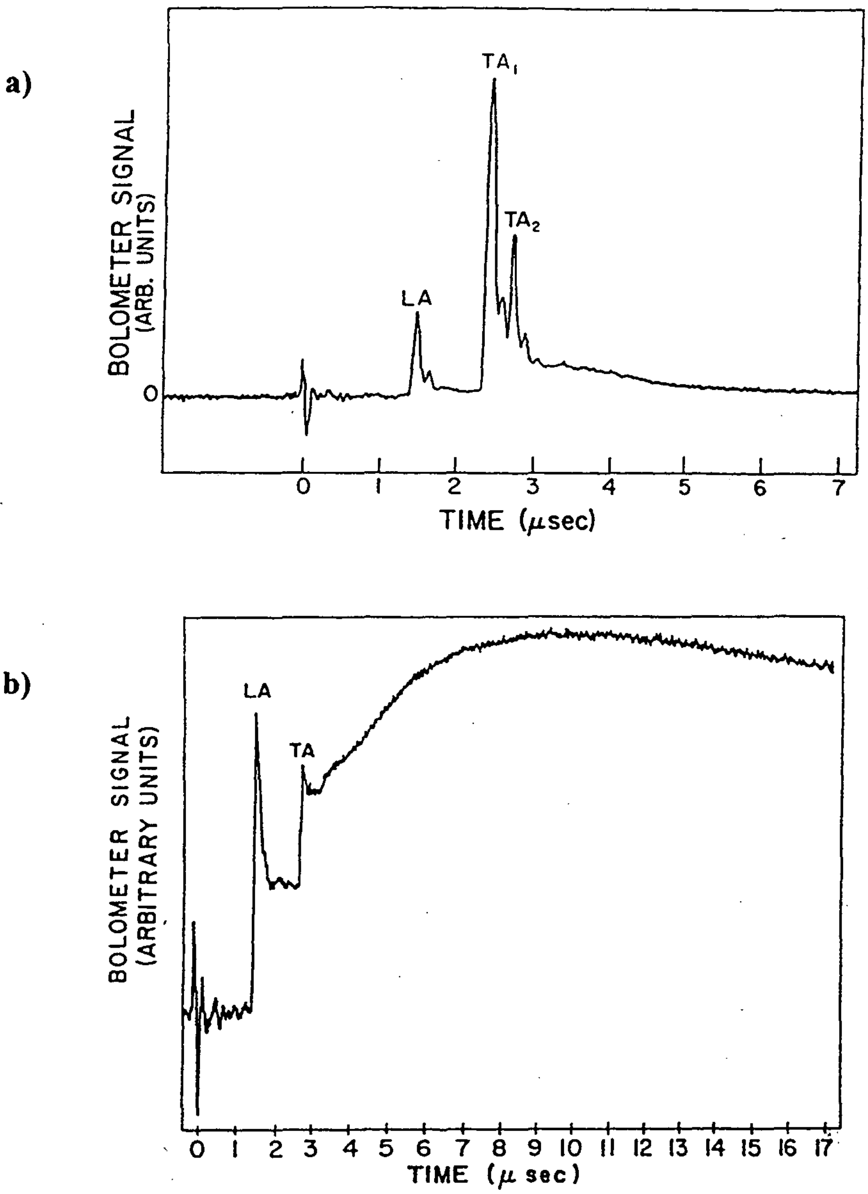

Figure 3.12: **a)** Ballistic time of flight spectrum from a heat pulsed pure crystalline Al_2O_3. TA_1 is the slow transverse acoustic mode while TA_2 is the fast transverse acoustic mode. **b)** The time of flight spectrum is diffusive because of impurity vanadium cations interacting with the nonequilibrium phonons. [Bron, 1984, 11]

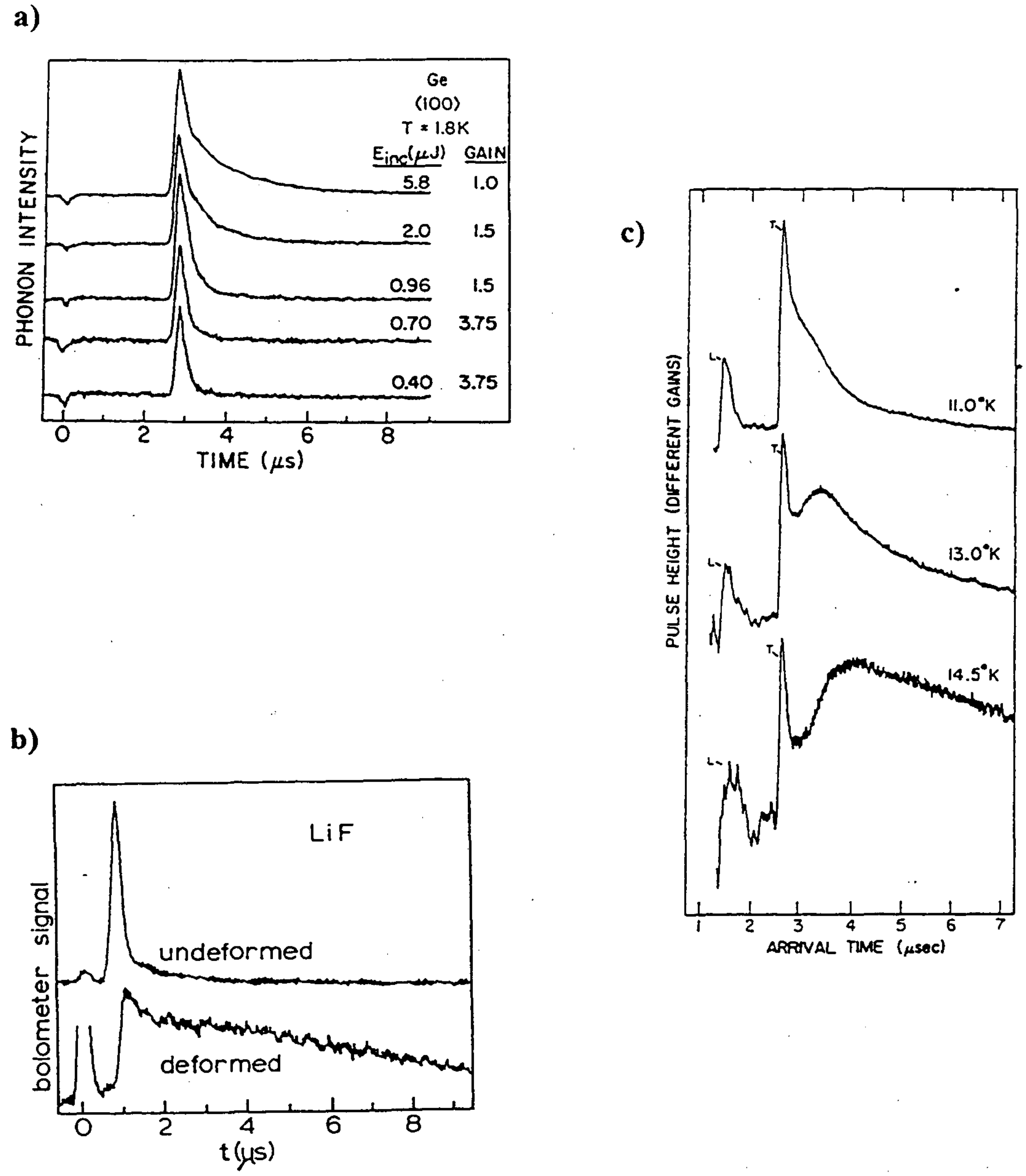

Figure 3.13: a) Phonon spectra from heat pulses in Ge showing that higher excitation-produced nonequilibrium phonons will be isotopically scattered. **b)** The upper phonon spectrum is from ballistic phonon propagation in dislocation free LiF. The lower spectrum shows the effect of scattering by deformation in LiF from dislocations. [Northrop and Wolfe, 1984, 72] **c)** Phonon spectra showing the condition of second sound by varying the temperature. Therefore, equilibrium phonons are the cause of scattering.[Jackson and Walker, 1971, 40]

film, producing a map of phonon intensities in two dimensions. This map is analogous to a sum of many time of flight spectra in terms of phonon intensities, since one pulse is, in actuality, a time of flight spectrum. By yielding two dimensional phonon intensities depicting both spatial anisotropy and flux directions, ballistic phonon imaging can be thought of as a quasi-three dimensional view of the sum of many time of flight spectra. The results and predictions of the enhancement factor, A, and the constant $\omega(\mathrm{k})$ and v_g plots are seen in ballistic phonon mapping, since the mapping yields two dimensional phonon intensities.

Ballistic phonon imaging requires a sophisticated experimental setup. A detector with high solid angle resolution is desired. Therefore, the detector area must be minimized. To determine the phonon intensity relative to the propagation direction, a laser is pulsed at 5 kHz where the pulse time is on the order of 10^{-7} s. A boxcar integrator samples the phonon intensity for each laser pulse at each position. The boxcar gate or time window is large enough to record all three polarizations. A computer is used for laser control and data acquisition. The laser is scanned in a 256X256 array which is comparable to having a 256X256 array of fixed detectors. A computer is then used to average and display the two dimensional array of phonon intensities.

The results of phonon imaging are shown in figure 3.14 for a (100) Ge crystal. Figure 3.14a shows the phonon intensities for the TA modes. Each line represents a horizontal scan as integrated by the boxcar gate. The actual ballistic phonon image is shown in figure 3.14b. The image is just the detector. The surface represents the (100) plane. The bright regions correspond to high energy fluxes of the TA modes while the dark areas are regions of low energy flux. Other modes can be seen by changing the

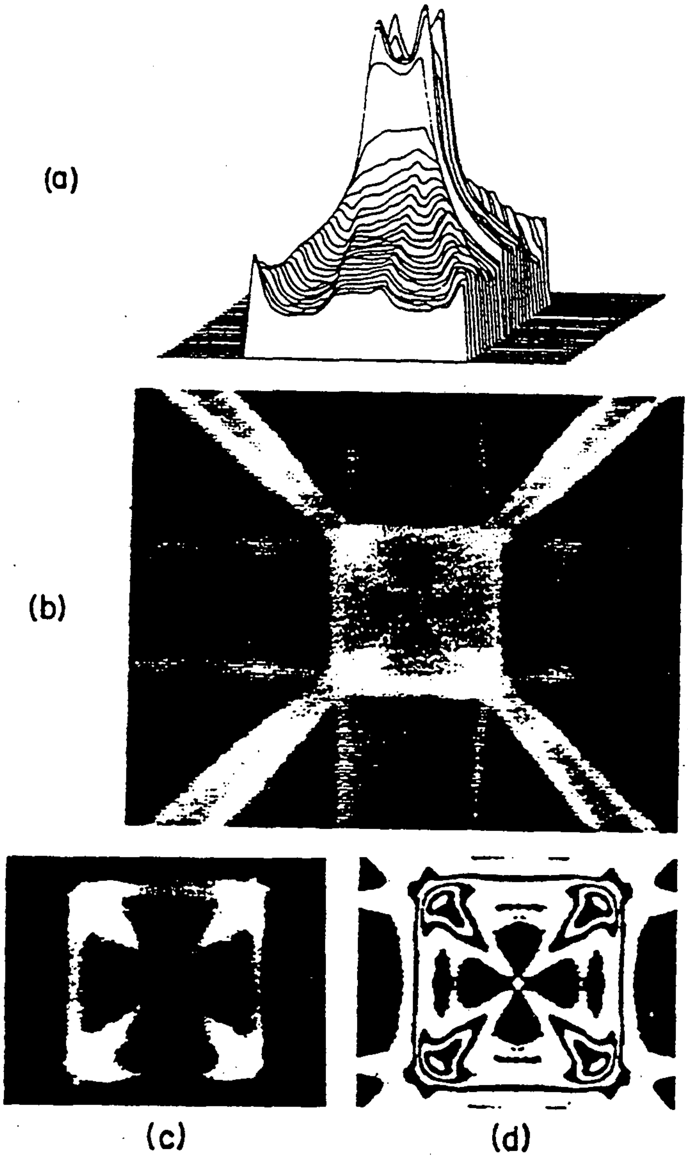

Figure 3.14: **a)** The lines depict successive horizontal scanning and show boxcar integrated TA phonon intensities. . **b)** Ballistic phonon imaging of a (100) Ge crystal. **c)** The enlargement of the central square region of the phonon image. **d)** Constant intensity contour map of fig. 3.14c.[Northrop and Wolfe, 1979, 70]

boxcar gate times. The bright patterns resembling an "X" and a wide "+" lie in the <110> and <100> directions, respectively. The central bright square, which corresponds to the detector center, along with the bright "+" or vertical columns are associated to the STA modes and corresponds to the inner split peak ridge in figure 3.14a.. The bright "X" or diagonal columns correlate with the FTA phonons and the outer two diagonal ridges in figure 3.14a.

Reducing the scan rate enlarges the central region which is shown in figure 3.14c. In figure 3.14d, a phonon intensity contour map is shown. It is generated by alternating black and white bands to separate curves of constant intensity.

The complexity of the ballistic phonon image is explained using the results of the enhancement factor, A, derived in section 3.2.4. It has been found that the sign of the Jacobian (i.e., the inverse of A), given by equation 3.62, is especially effective in deciphering the phonon energy flux pattern.[Maris, 1986, 55; Northrop and Wolfe, 1979, 70] The Gaussian curvature of the constant-energy surface, for a given direction (θ_k, ϕ_k) defined in section 3.2.4, determines whether J is zero, positive, or negative. A value of zero for J gives rise to a strong flux enhancement. Table 3.1 gives the constant energy curvature and shape and corresponding J value. A connection between J and the Gaussian curvature, K, which may shed light on the information tabulated in table 3.1, is given by the following equation:

$$J=K|\bar{k}|^2cos(\Theta) \qquad [3.64]$$

where Θ is the angle between $\bar{k}$ and v_g.

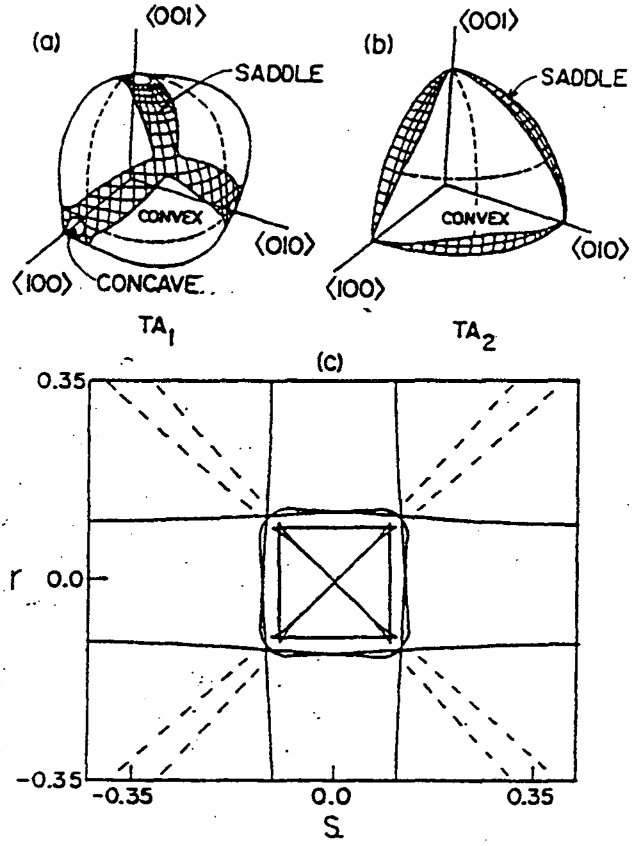

Figure 3.15: **a)** Calculated constant energy surface for the STA mode. **b)** Calculated constant energy surface for the FTA mode. **c)** Locus of J=0 points mapped onto a curve in v_g-space. [Northrop and Wolfe, 1979, 70]

Table 3. 1: Constant energy surface curvature and corresponding Jacobian sign.[Northrop and Wolfe, 1979, 70]

Gaussian Curvature (*K*)	Jacobian (*J*) Sign
concave	positive
convex	positive
saddle region	negative
border between pos. & neg. J	zero

The relationship between J and the constant-energy surfaces are exemplified by the computational results for both TA modes in Ge shown in figure 3.15. The TA_1 mode in figure 3.15a is the STA mode. In figure 3.15b, the TA_2 mode is the FTA mode. The borders of the shaded region is where J is zero. The borders correlate to mathematically infinite enhancement. The regions of negative J are the shaded areas of the plots. The transformation of equation 3.60 maps the locus of J=0 points to $\mathbf{v}_g$-space giving rise to figure 3.15c. The lines denote the locus of J=0 points. The solid lines represent the STA mode. The solid lines within and forming the inner square correspond to the J=0 curve between the saddle and concave regions. The outer solid lines are associated with the J=0 curve which lie between the convex and saddle regions. The dashed lines are also the locus of J=0 points. The axes in figure 3.15c are given by:

$$r = -\tan(\theta_v)\sin\left(\theta_v - \frac{\pi}{4}\right) \qquad [3.65]$$

$$s = \tan(\theta_v)\cos\left(\theta_v - \frac{\pi}{4}\right) \qquad [3.66]$$

where (θ_v, ϕ_v) is the propagation angle (see section 3.2.4).[Northrop and Wolfe, 1980, 71]

3.2.6 Nonequilibrium Phonon Interfacial Scattering

When a material is placed in contact with liquid helium and a metal and liquid helium interface is formed, a thermal resistance is created at the boundary. This phenomenon was observed by Kapitza in 1941 and subsequently called the *Kapitza* resistance.[Anderson, 1980, 2] Kapitza resistance also occurs at the interface of two solids. This effect is understandable through the use of phonon propagation modes and conditions explained in section 3.2.3. Consider elastic waves (assuming the long wavelength approximation) traveling through a continuous medium and coming upon a boundary between the present medium and an opposite medium. As mentioned in section 3.1.5, interfaces will cause elastic waves to scatter. This is because of the mass and chemical bonding differences causing diffuse scattering which occurs under the condition and scattering rate given by equations 3.42 and 3.39. The scattering of an elastic wave by an interface will cause a fraction of the initial wave to transmit into the second medium as a refracted elastic wave, and the remaining fraction will be reflected back into the first medium. Both the reflected and refracted waves' polarization will differ from the polarization of the incident elastic wave. In other words, the initial polarization will undergo a mode conversion.[Weis, 1969, 104] The treatment of phonon scattering at the interface of two media in terms of reflection and refraction is described by two models. The most noted or referenced model is called the *acoustic mismatch model*, while the other is termed, in this thesis, the *atomic scale mismatch model*. Both models attempt to derive the reflection and transmission coefficients of the incident elastic wave. The purpose of this section is to briefly introduce each model such that familiarity of each is attained.

In the *atomic scale mismatch model*, the purpose is to develop a model in which interfacial scattering can be treated for phonons that do and do not fall within the long wavelength approximation. Derived by Steinbrüchel, the approach used in this model is to define the interface as a linear chain of atoms, which is very similar to the approach used to develop the dispersion relation in section 3.1.4.[Steinbrüchel, 1976, 91] Both linear chain models use the concept of a linear chain of atoms attached by bonds with a given force constant. In Steinbrüchel's model, one half of the linear chain is made up of medium 1 while the remaining half is made up of medium 2. Therefore, in the simplest case, there are two masses and three force constants which need to be considered. These are the masses and force constants of medium 1 and 2 and the force constants between medium 1 and medium 2. Equations of motion are then developed to describe elastic waves propagating through the linear chain. The equations are solved in terms of the angular frequency, ω. Also, the amplitudes of the equations of traveling waves, analogous to Z in equation 3.24, are solved for boundary conditions relative to the interface. The interest in the wave amplitudes at the interface is due to the fact that the square of the wave amplitudes are the probabilities of reflection and transmission. The problem is very similar to solving the probability of an electron tunneling through an energy barrier. The sum of the squares of the amplitudes is one. The power transmission coefficient can be calculated by multiplying the ratio of momentum in medium 1 to medium 2 by the probability of transmission (i.e., square of the transmission amplitude).

There are several limitations in this model. First, phonon reflection and transmission coefficients for each polarization cannot be calculated unless the model is derived for the three dimensional case. Also, as was mentioned in section 3.1.4, additional force constants need to be introduced when considering crystallographic orientations in which not just one distance between atoms exists (i.e., <111> in diamond cubic structures). Nevertheless, the approach of this model is noteworthy because phonon scattering at the microscopic level is considered. To this author's knowledge, validation of this model with experimental data has not been investigated.

The more widely referenced model used to describe interfacial phonon scattering is the *acoustic mismatch model*. First applied by Little to describe Kapitza resistance at low temperatures between isotropic solid-solid interfaces, it was also utilized in this manner by others.[Little, 1959, 51; Rösch and Weis, 1976, 84; Rösch and Weis, 1976, 85; Weis, 1969, 104] Rösch and Weis then applied the model to interfaces in which one medium was isotropic while the other medium was anisotropic.[Rösch and Weis, 1977, 86] The model was finally applied by Weis to interfaces bound by two anisotropic media.[Weis, 1979, 105; Weis, 1986, 106; Weis, 1987, 107]

The essence of the acoustic mismatch model lies in the long wavelength continuum assumption and the use of Snell's Law to determine the reflection and refraction of elastic waves. Snell's law, which states that the wavevector component parallel to the interface is conserved, is given by:

$$k_{\|} = k_{\chi 1} \sin\theta_{\chi 1} = k_{\chi 2}^{1} \sin\theta_{\chi 2}^{1} = k_{\chi 2}^{2} \sin\theta_{\chi 2}^{2} \qquad [3.67]$$

for two anisotropic crystalline materials confining an interface where the variables are defined in table 3.2.[Höss, et al., 1990, 33; Weis, 1987, 107]

Table 3.2: A description of Snell's law variables[Höss, et al., 1990, 33; Weis, 1987, 1

Variable	Description of Variable
$k_{\|}$	Component of wavevector of incident wave parallel to interface
$\chi 1$	Polarization of incident wave
$\chi 2$	Polarization of reflected or transmitted wave
$k_{\chi 1}$	Wavevector of incident wave in medium 1 with polarization $\chi 1$
$k_{\chi 2}^{1}$	Wavevector of reflected wave
$k_{\chi 2}^{2}$	Wavevector of transmitted wave
$\theta_{\chi 1}$	Angle of incident wave
$\theta_{\chi 2}^{1}$	Angle of reflected wave
$\theta_{\chi 2}^{2}$	Angle of transmitted wave

Figure 3.16 gives a geometrical view of Snell's law as applied to an interface bound by two crystalline materials. To simplify the diagram, the two crystals are identical but rotated. Hence, the interface is actually a grain boundary. As can be seen in figure 3.16, six waves are excited with the incident wave: three reflected and three refracted. It

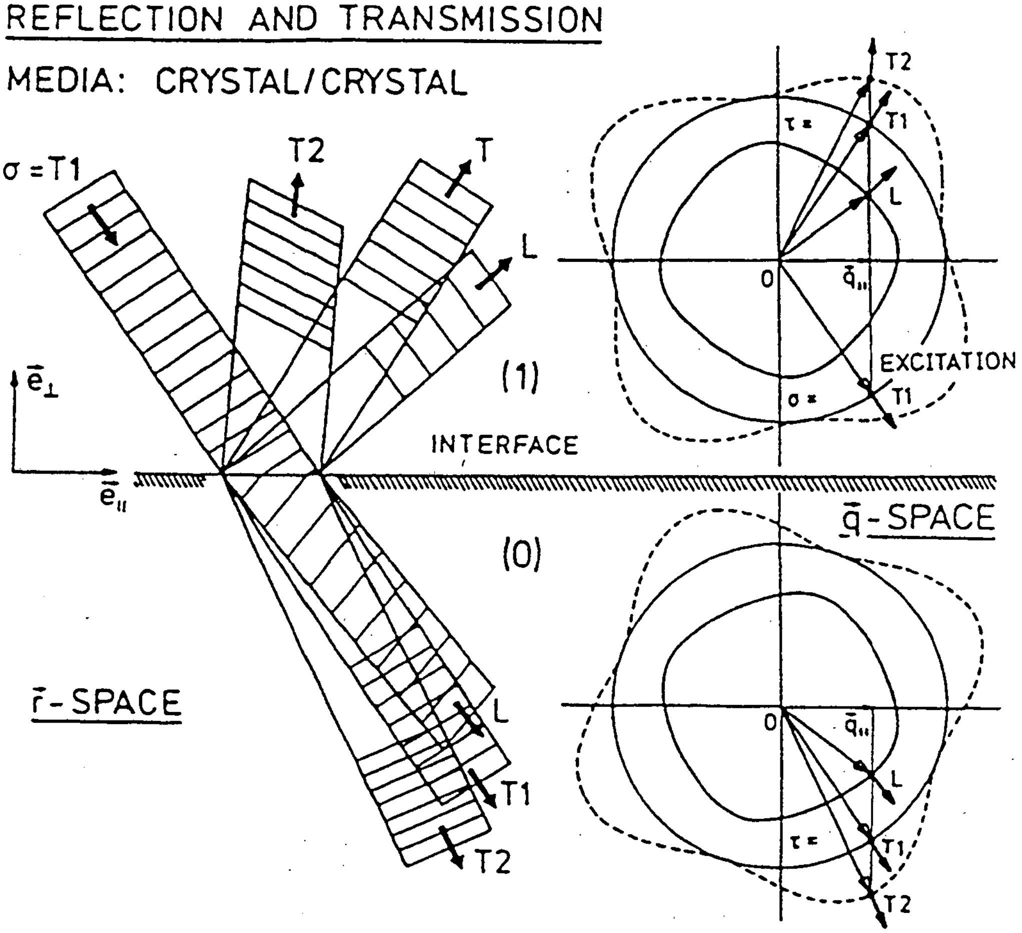

Figure 3.16: A geometrical representation of Snell's law. To simplify the illustration, the interface is bound by two equivalent but rotated crystals and is also a mirror plane. The incident wave is a transverse acoustical wave. The reflected and refracted excited waves are fast and slow transverse and longitudinal acoustic waves.[Weis, 1987, 107]

turns out that this configuration is the maximum number of waves that can be excited in both mediums by the incident waves.[Feuchtwang, 1967, 23; Feuchtwang, 1967, 24; Weis, 1987, 107] Furthermore, as a consequence of Snell's law, the excited waves can be decaying exponentials as well as constant plane waves.

The acoustic mismatch model is derived using similar methods to derive the enhancement factor in phonon focusing section, 3.2.4. Equation 3.10, the constitutive relation of elasticity theory, is utilized to develop the Christoffel tensor given by equation 3.57. Furthermore, several field vectors associated with the incident plane wave are defined to develop the model.[Weis, 1979, 105] The displacements fields of the incident wave are distinguished using a displacement vector, $s(\bar{r},t)$, which is related to the strain field, $\varepsilon(\bar{r},t)$, such that:

$$\varepsilon(\bar{r},t) = \varepsilon_{lm}(\bar{r},t) = \left[\frac{s_{lm} + s_{ml}}{2}\right] \qquad [3.68]$$

A time dependence is shown since the displacement fields are caused by an elastic wave propagating in both the space and time domain. A mechanical "Poynting vector", which is the mechanical energy flux of the incident wave, is introduced and is given by:

$$\bar{S}(\bar{r},t) = -\sigma(\bar{r},t) \cdot \nabla_t \bar{s}(\bar{r},t) = u(\bar{r},t) \cdot \bar{v}_g(\bar{k}) \qquad [3.69]$$

where σ is the stress field defined by equation 3.10, the time gradient of the displacement field is the particle velocity field, v_g is the group or energy velocity, and $u(\bar{r},t)$ is the energy density.[Weis, 1986, 106] Utilizing these vector fields with the Christoffel equation, the polarizations of the excited waves are determined. The power transmission and reflection factors for each polarization are found using the ratios of the mechanical Poynting vector of each polarization.[Weis, 1979, 105] The transmission and reflection coefficients are derived using the ratios of the displacement fields for each polarization.[Weis, 1979, 105]

Application and validation of the acoustic mismatch model with experimental data has been investigated with varying success. Both Taborek and Goodstein and Marx and Eisenmenger could not correlate their experimental results with the results derived using the acoustic mismatch model.[Marx and Eisenmenger, 1982, 57; Taborek and Goodstein, 1980, 93] It was assumed that the reason for the failure of the acoustic mismatch model was that the morphology of the interfaces was too rough in both the experiments. However, Höss *et al.* showed, by minimizing the interface flaws, their data agreed with the acoustic mismatch model.[Höss, et al., 1990, 33]

3.3 Experimental Procedure

3.3.1 Sample Preparation

The details of Ge processing and Ge sample preparation through eutectic bonding have been previously discussed. The extra processing steps involved with fabricating eutectically bonded samples for phonon transmission and imaging studies are discussed here.

Samples fabricated for phonon transmission studies require an extra processing step prior to eutectic bonding. After the lapped and polished Ge wafers were diced to form bonding pairs, the top substrate was cut in half. The cleaning, etching, and metallization procedures were the same. Before mounting the substrates into the eutectic bonding apparatus, the half-length substrate was placed on the top and to one end of the longer bottom substrate. Therefore, simultaneous phonon imaging of the sample with and without an eutectic interface was performed on one sample. In this configuration, the sandwiched substrates were placed in the eutectic bonding rig and annealed for eutectic bonding.

Once the two substrates were eutectically bonded, the bottom samples' free surface was lapped and optically polished using the procedure explained in section 2.2.3. This step was required to maximize the possibility of adhesion of a thermally evaporated Al superconducting transition edge detector/bolometer which was evaporated onto the surface.[Northrop and Wolfe, 1984, 72] After the bottom free surface had been optically polished, it was masked with a mixture of equal parts picene and bees wax in toluene. The sample was placed in an aqueous solution of KBr for 30 seconds to remove Au from the exposed unbonded interface. The wax was removed by placing the sample in boiling 1,1,1-trichloroethane and then in boiling methanol each for three minutes.

The thickness of the top substrate (½ piece) was reduced to 300 μm by polish-etching. The surface of the top substrate must be both smooth and flat in order to obtain optimum phonon imaging results. The optically polished surface (bottom) was protected from the etchant by adhering mica, using wax, to the optically polished surface. The sample was submerged and agitated in a 7:2:1 solution of HNO_3, HF, and red fuming HNO_3. The etch rate was approximately 254 nm per second. The mica was removed by heating the sample on a hot plate. The wax and other organic contaminants were

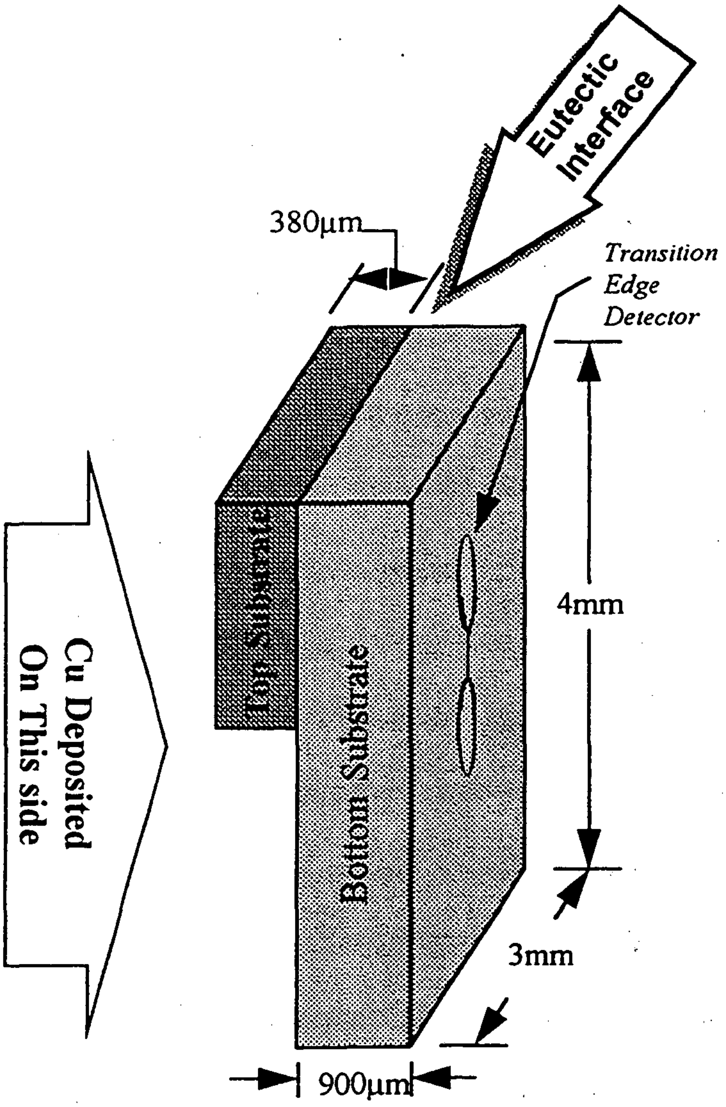

Figure 3.17: Sample configuration for phonon transmission studies. The thicknesses of the two bonded substrates will vary from those given above.

eliminated by placing the sample in boiling 1,1,1-trichloroethane, then in boiling acetone, and finally in boiling methanol each for three minutes.

Copper was deposited (2000 Å) onto the polished-etched side using electron beam deposition. Copper was used in this experiment to absorb the laser pulses. In laser heat pulse techniques, a metal film is used to ensure low energy nonequilibrium phonon excitation (see section 3.2.2).

The next processing step was the fabrication of an Al transition edge detector (bolometer). The bolometer was constructed via evaporation of Al in an oxygen ambient onto the bottom of the Ge sample surface. The Ge surface was patterned using photolithography techniques. First, positive photoresist was spun onto the sample at 900 RPM. The sample was then soft baked at 90°C for 15 minutes. The sample was covered by a photolithographic mask and exposed to ultraviolet radiation. Following UV exposure, the sample was immersed in a developing solution to remove the exposed photoresist. [Knowlton, 1989, 45] The masked sample was placed into a thermal evaporator. The evaporator was ambient-evacuated to a base pressure of $6x10^{-6}$ Torr. Oxygen gas was released into the chamber until $7x10^{-5}$ Torr was reached. Al was thermally evaporated in the oxygen ambient thereby forming Al.

The final processing step was the formation of contacts to the bolometer and attachment of wire leads to the contacts. Indium was pressed onto the ends of the bolometer to form the contacts and Au wire was indium soldered to the contacts.

The sample configuration is shown in figure 3.17. The indium contacts and bonded wires are not yet on the sample. Note that the bolometer is on the opposite side of the Cu film. This information is important to the conceptualization and comprehension of the phonon imaging data to be shown latter.

3.3.2 Experimental Methods and Apparatus

Phonon imaging involves laser pulsing and scanning of the sample cooled in a helium dewar. The pulses range from tens of nanoseconds up to the microseconds. To ensure low excitation of nonequilibrium phonons, the laser was pulsed onto a metal film, typically called the *heater*, which covers the Ge surface (see section 3.1.2). The propagating phonons were detected by a bolometer on the opposite side of the sample. A boxcar (gated) integrator sampled the signal and then sent the phonon intensity signal (z) for a particular laser position (x,y) to a computer.. The boxcar integrated the heat pulse signal over a specified gate time, Δt, which was on the order of a microsecond. The initial gate time was just prior to the heat pulse while the final gate time was just following the heat pulse. The boxcar integrator sent the time-resolved data to a computer which accumulated in a 256x256 array. The spatial phonon images were derived from this data. To acquire a time of flight spectrum (i.e., the velocity) for a particular (x,y) position, the gate was substantially reduced to a few nanoseconds and scanned over the incoming bolometer signal. Also called constant-velocity scanning, this method of integration essentially integrates the bolometer signal. The resulting data from both integration methods will be shown in the following section.

The phonon imaging system described above consisted of the laser, helium dewar, bolometer, boxcar integrator, and computer. A schematic of the phonon imaging system is shown in figure 3.18. A brief synopsis of the system is discussed below. The intricacies and details of the system are explained elsewhere. [Northrop and Wolfe, 1980, 71; Northrop and Wolfe, 1984, 72]

The sample was cooled by immersion into superfluid helium contained in an optically accessed helium dewar. The temperature was controlled by using a vacuum system and manostat to regulate the helium vapor pressure. The temperature was adjustable in 0.01K increments within a range from 1.4 K to 4.2 K.

The laser was a Spectra Physics model 164 argon ion laser. The pulse length used during imaging was 15 ns at full width at half maximum. The peak power was 1 watt with a wavelength of 0.514 μm. The time between laser pulses was 40 μs. The laser beam spot size impinging on the sample was about 100 μm. An "x" mirror and "y" mirror control the scanning of the laser beam. The x-mirror controls the x position by rotating horizontally (i.e., changing the yaw), while the y-mirror controls the y-position by changing the mirrors pitch. Galvanometers drive the mirrors which raster-scan the laser beam across the sample.

The bolometer was an Al transition edge detector as mentioned in section 3.3.1. Figure 3.19 shows both the dimensions and resistance versus temperature characteristics of the bolometer. The thin wire-like region is approximately 12 μm wide. The temperature of the sample was kept in the range where $\frac{dR}{dT}$ was linear and maximized. This provided optimal sensitivity and output linearity.

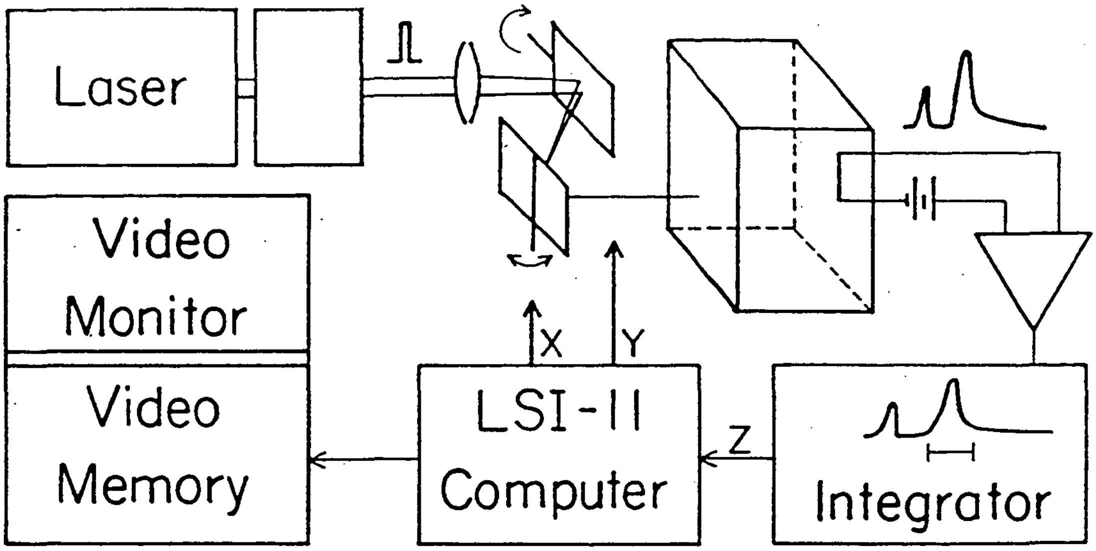

Figure 3.18: A schematic of the phonon imaging system.[Northrop, 1982, 69]

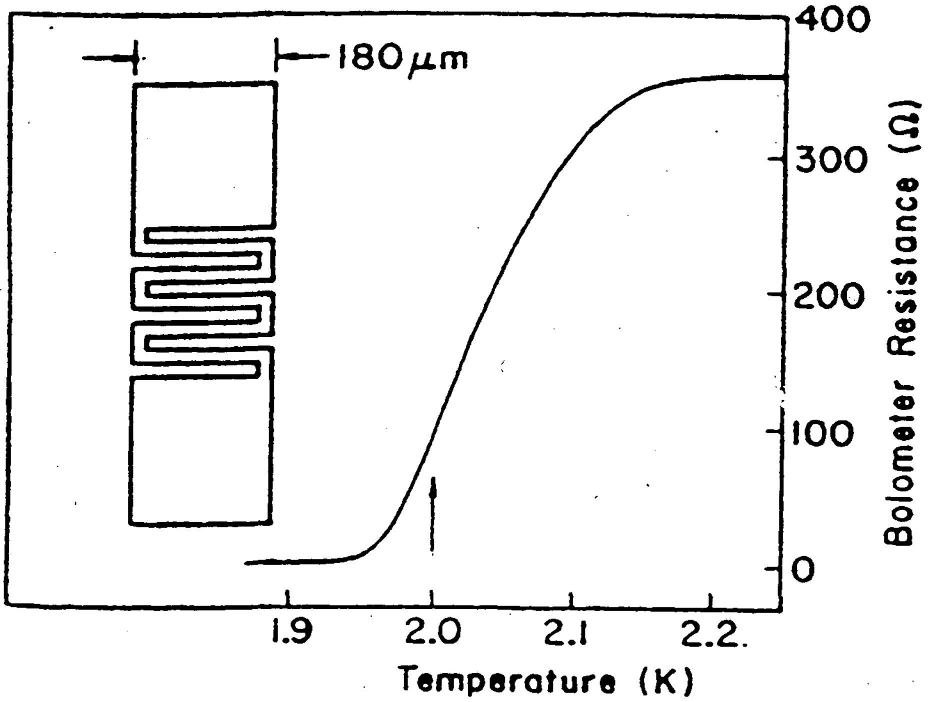

Figure 3.19: Al bolometer schematics and resistance versus temperature characteristics.[Northrop and Wolfe, 1984, 72]

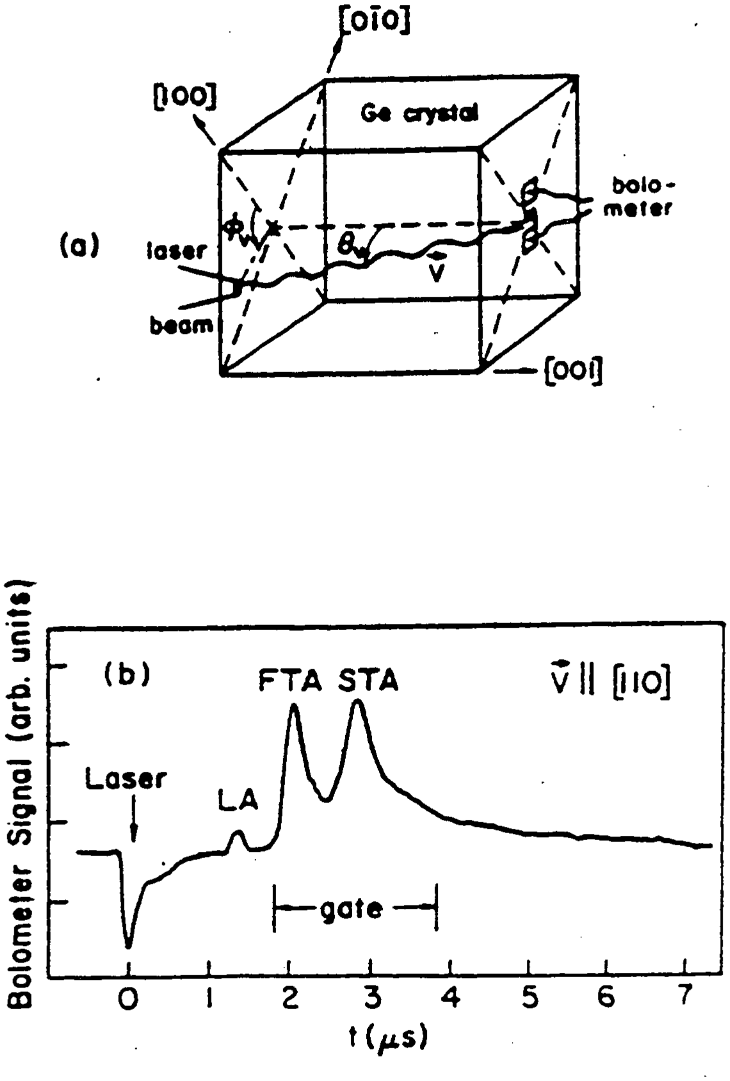

Figure 3.20: **a)** A schematic of a Ge sample showing the propagation direction of a laser pulse-created phonon. On the face being pulsed are dashed lines with arrows and directions in Miller indices format. The dashed lines on this face correspond to the lines, both solid and dashed, in figure 3.15c. As mentioned in section 3.2.4, the direction (θ_v,ϕ_v) in v_g-space. **b)** The bolometer signal showing a "time of flight" spectra for the [110] propagation direction in (100) Ge. The length depicting the gated region is the value Δt.[Northrop and Wolfe, 1984, 72]

Figure 3.20a illustrates the geometrical relationship between the propagating phonon produced by the laser pulse and the bolometer on the sample. The dashed and solid lines seen in figure 3.15c correspond to the dashed lines on the face where the laser was pulsed. The phonon propagation direction in v_g-space, given by (θ_v,ϕ_v), can be conceptualized in this illustration where v is v_g. In figure 3.20b, a time of flight spectrum is shown for the [110] direction in (100) Ge. The region marked shows how the gate can be adjusted within the boxcar integrator so that the signal can be sampled at various points. In this case, the gate was positioned to sample the acoustic signal but not the longitudinal signal.[Northrop, 1982, 69; Northrop and Wolfe, 1979, 70; Northrop and Wolfe, 1980, 71; Northrop and Wolfe, 1984, 72; Wolfe, 1980, 109]

3.4 Results and Discussion

In studies of phonon scattering by an interface between two different media, a comparison is typically made between the initial laser pulse energy and the amount of energy which reaches the detector. Furthermore, the acoustic mismatch model is used to predict and analyze the amount of phonon transmission and reflection at the interface.[Anderson, 1980, 2; Every, et al., 1984, 22; Höss, et al., 1990, 33; Koos, et al., 1983, 47; Marx and Eisenmenger, 1982, 57; Northrop and Wolfe, 1984, 73; Taborek and Goodstein, 1980, 93]

In this study, the acoustic mismatch model was not used to predict the amount of phonon transmission through the eutectic interface nor analyze the data. Rather, the approach used compares the phonon transmission of a sample without an eutectic interface to that of a sample with an eutectic interface. The goal of this phonon transmission study was to determine the phonon transmission through a Ge-Au-Ge eutectic interface as a function of the initial Au thickness. Therefore, the acoustic mismatch model is not appropriate for the following reasons. First, the acoustic mismatch model assumes the two media bounding the interface are dissimilar. In this study, the two media were the same assuming the effect on phonon propagation by the Au layer was minimal. This assumption is true if the interface was mainly Ge or if the phonon wavelength was longer than the interface width. For initial Au deposition thicknesses of 500 Å or less per sample side, the structure of the eutectic interface was made up of Au aggregates interspersed in a Ge matrix. Thus, this assumption holds fairly well. At initial Au thicknesses greater than 500 Å/sample, especially in the range of 1000 Å per sample side, Au forms a barrier between the two Ge samples with only a few areas where Ge penetrates through the Au. Furthermore, the data for the samples without an interface clearly shows that the phonon propagation mode was ballistic. Hence, the phonon mean free path was at least on the order of the sample thickness ($L \sim 1$ mm). The interface thickness for samples with an initial Au thickness of 1000 Å Au per side is 2000 Å. The phonon mean free path was 99.98 percent larger (or 5000 times larger) than the thickest interface.

In addition, the focus of the study was not to determine the initial versus final energy flux. The goal was to determine the amount of phonon transmission through the eutectic interface. Since the media on either side of the interface was the same, other scattering mechanisms in the media can be ignored; therefore the initial versus the final energy flux problem ceases to be a factor. Hence, the only scattering left to consider is the scattering at the interface.

In phonon focusing and imaging experiments, several boundaries exist that cause phonons to scatter. The boundaries of concern are between the sample and phonon-emitting film and the sample and detector. In this study, the emphasis was on the comparison of phonon transmission between an area in the sample (see figure 3.17) containing an eutectic interface and an area in the same sample not containing an eutectic interface. Because the boundaries between the sample, the samples' phonon-emitting film, and the samples' detector were the same for all samples, than the hindrance of phonon transmission was the same for all samples (excluding the eutectic interface). Since this hindrance of phonon transmission was the same for all samples, it is not a concern. Additionally, the phonon wavelength was greater than the interface thickness; therefore equivalent boundary conditions can be used eliminating the need to consider scattering caused by interface roughness.[Every, et al., 1984, 22]

Three types of data are graphically presented in this section: phonon imaging intensities in two dimensions, time of flight spectra (TOF), and line scan spectra. The phonon imaging spectra is the bolometer image which was used to determine the amount of phonon transmission through the interface. The time of flight spectra, where one spectrum represents one point on the phonon image, were used to determine both the phonon propagation mode and, somewhat less accurately, the amount of phonon transmission. The line scan spectra represent one horizontal scan of the phonon image and were used as a comparative means of phonon transmission determination.

The determination of the percentage of transparency or transmission of phonons through an eutectic interface was performed by several methods. For the primary method, measurements were taken of the intensities from specific areas of phonon images. Equal areas were chosen on either side of the boundary separating the regions of sample with and without an eutectic interface so that the region's geometric centers were equidistant from the bolometer's center. Therefore, each area was equivalent to the other relative to the center of the bolometer. The maximum equivalent areas occur when the bolometer center coincides with the boundary separating the noneutectic and eutectic interface regions. Within each area are a number of points. The points are intensities with values ranging between one and ten corresponding to low and high intensities, respectively. The intensity values for all points within the area were summed. The percent transmission through the eutectic interface was determined by the ratio of each area's total intensities such that:

$$T_i = \frac{I_i}{I_t} x100 \qquad [3.70]$$

where T_i is the percent transmission through the interface, I_i was the total intensity of the area with an eutectic interface, and I_t was the total intensity of the area without an eutectic interface. The laser raster-scanned 256 points horizontally and vertically, therefore a total of 65,536 points of phonon intensities were acquired. A maximum of half the number of total points are summed per area if the bolometer's position coincides with the boundary separating the areas with and without the eutectic interface. Because the number of points summed within each area was considerable (as high as 32,768), this method of percent transmission determination through the interface was the most accurate.

The second method to determine the amount of phonon transmission through an interface was accomplished by calculating the ratio of certain areas under the line scan spectrum. The line scan spectrum is comprised of three peaks: the central split peak and one peak on either side of the central peak (figure 3.14a). The central split peak corresponds to the vertical and horizontal center of the bolometer for a horizontal and vertical line scan, respectively. As previously stated, areas were chosen on either side of the boundary separating the region of sample with and without an eutectic region such that their geometric centers were equidistant from the bolometer's vertical or horizontal center depending on the type of line scan. The areas were calculated by integrating the curve in the region of the chosen areas. The percent transmission through the eutectic interface was calculated using equation 3.70 and replacing the intensities with the areas.

The percent transmission of phonons through the interface was also determined from time of flight data similar to the spectra shown in figures 3.13 and 3.20b. Two equivalent points were chosen on either side of the bolometer center. Each point represents a time of flight spectrum. From the equivalent points, the areas of the acoustic peaks in the time of flight data were obtained and compared. Using equation 3.70, where the intensities were replaced by the peak areas, the percent phonon transmission was determined. Because the line scan data set was 256 times smaller than the phonon imaging data set, and the TOF data only represents one intensity point on the phonon imaging plot, the percentage of phonon transmission obtained by either method is not statistically accurate and was only used as a comparison between equivalent points or equivalent areas.

In this study, the first attempt made to determine the amount of phonon transmission through an eutectic interface was performed on a Si-Au-Si eutectic interface configured as shown in figure 3.17. The initial Au deposition layer thickness was on the order of ~ 1000 Å per substrate side. The results are shown in figure 3.21. The view the image is depicting is the (100) sample surface on which the transition edge detector was deposited. This surface is opposite to the surface on which the laser is raster scanned. These and following phonon images correspond to the phonon images in figure 3.14b, c, d, and 3.15b and their descriptions given in section 3.2.5. Again, the central bright region is an outline of the transition edge detector itself and shows the four-fold symmetry of the (100) plane in which the phonons are traveling. The bright "arms", called caustics, jutting out from the central square represent the regions of high phonon energy flux and are the result of phonon focusing. The caustics that resemble a perpendicular cross (i.e., "+") or a diagonal cross (i.e., "x") coincide with the STA mode in the <110> or the FTA mode in the <100> directions, respectively. The boundary separating the sample sections with and without the eutectic interface is distinguished by the dark wide vertical line near the center of the image as indicated by an arrow. By comparing the intensity on the left (i.e., unbonded side) to the intensity on the right (i.e., bonded side), the amount of transmission is seen to be minimal. The percent transmission of phonons through the eutectic interface was calculated to be ~ 4 percent.

The lack of phonon focusing effects (e.g., caustics) on the eutectic interface side of the phonon image suggests the absence of a ballistic phonon propagation mode. Line scan data showed the nonexistence of FTA and STA ridges which accompany ballistic line scan data. The TOF spectra showed that only the diffusive propagation mode existed.

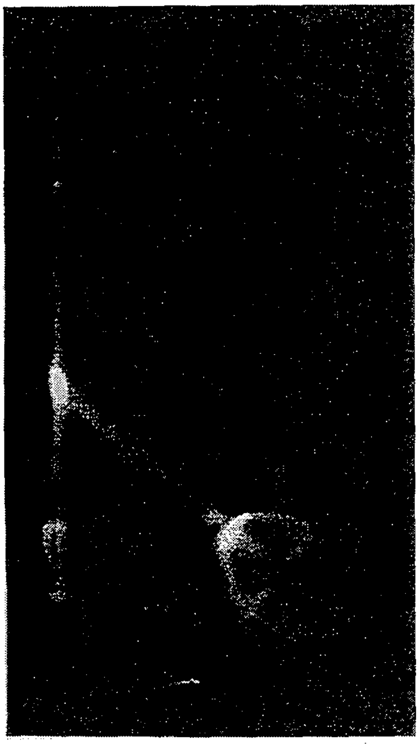

Eutectic Interface Side

No Eutectic Interface Side

Border

Figure 3.21: A bolometer phonon image of a Si-Au-Si eutectically bonded sample with an initial Au thickness of 1000 Å/side. The wide dark vertical line pointed out by the arrow illustrates the boundary between the sample side with and without an eutectic interface. The bright arms are the caustics. The caustics forming an "x" and "+" are the FTA modes in the <100> direction and STA modes in the <110> direction. The intersection of caustics showing 3-fold symmetry is the <111> direction. Only about 4% phonon transmission was calculated for this sample.

In many of following phonon images, the high energy fluxes (caustics) are the dark rather than bright crosses. The only difference between the two caustic colors is the method of digitizing the data.

Phonon imaging studies were next performed on Ge-Au-Ge eutectically bonded samples with varying initial thickness of Au. In figures 3.22 and 3.23, several phonon images are shown of the same eutectic sample. The initial Au deposition layer thickness was 300 Å on each substrate side. The sample configuration are shown schematically in figure 3.17. The eutectic/no eutectic boundary is identified by the faded vertical line near the center of the images signified by an arrow. In figure 3.22, the surface of the sample which was laser pulsed does not have a deposited Cu film. As discussed in the section covering excitation methods (3.2.2), direct photo-excitation of a bare surface will produce hot electron-hole pairs. In this sample, it is likely that electron-hole pairs traveled to and down converted at the interface. Down conversion at the interface creates an interfacial phonon source which gives erroneous percent transmission results. Therefore, the percentage of phonon transmission was not calculated for this image. The indirect excitation method was deemed more reliable; subsequently, the laser pulsed sample surface was covered with a copper film to alleviate the production of hot electron hole carriers.

Figure 3.23 shows the phonon image produced using the indirect excitation method. Notice that the caustics for both the STA mode and the FTA mode are much less smeared than the same caustics in the photoexcited sample. Thus, it was reasonable to assume that hot electron hole pairs, via down conversion, were producing phonons at the interface.

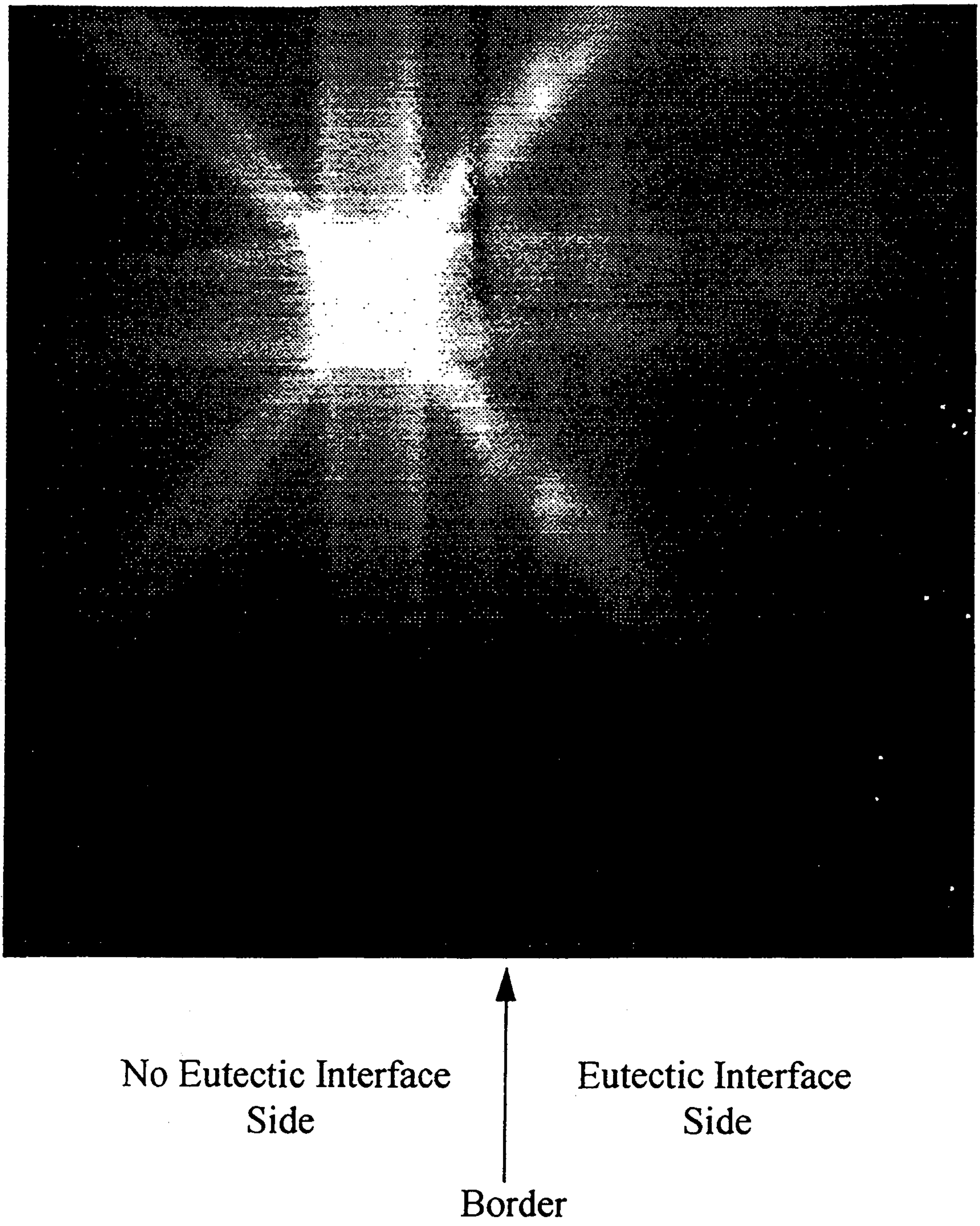

Figure 3.22: A bolometer phonon image of Ge-Au-Ge eutectically bonded sample with an initial Au thickness of 300 Å/side by means of direct excitation. The wide dark vertical line pointed out by the arrow illustrates the boundary between the sample side with and without an eutectic interface.

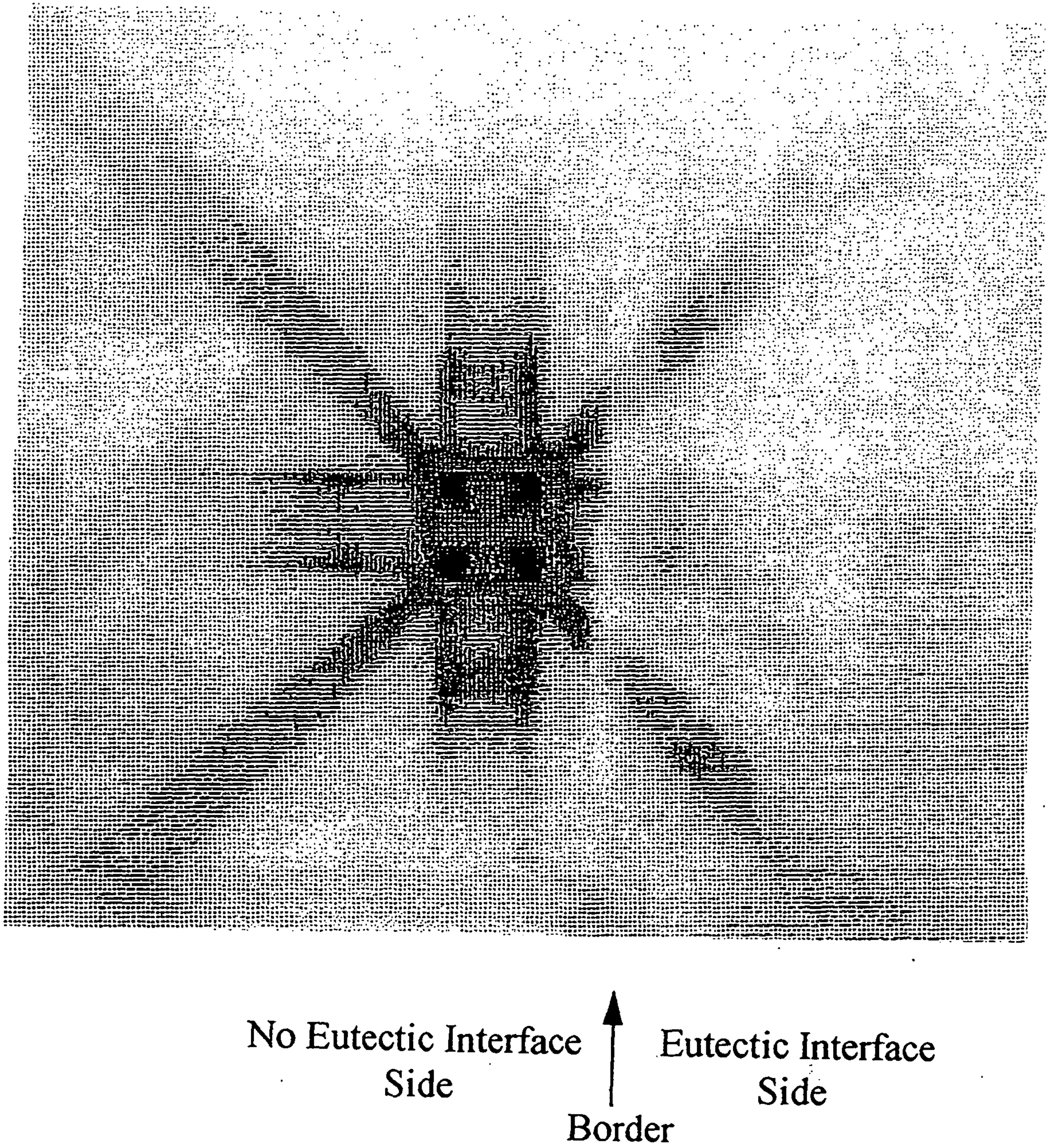

Figure 3.23: A bolometer phonon image of a Ge-Au-Ge eutectically bonded sample with an initial Au thickness of 300 Å/side by means of indirect excitation of a Cu film. The lighter vertical line (near the <110> caustic) pointed out by the arrow illustrates the boundary between the sample side with and without an eutectic interface.

Because the bolometer was deposited just to the left of the boundary separating the eutectic interface region of the sample from the sample region without the interface, the boundary line seen in figures 3.22 and 3.23 was to the right of the central square. Consequently, when calculating the percent of phonon transmission through the eutectic interface, equivalent areas have to be chosen such that they are symmetric with the image and not the boundary. A calculation of the percentage of phonon transmission from the phonon image shown in figure 3.22 gave a value of 70 %.

The line scan data was analyzed to confirm the percent phonon transmission calculated from the phonon images. As mentioned previously, the calculation of percent phonon transmission is less accurate using this method than using the phonon imaging method. The horizontal line scan spectra shown in figures 3.24 and 3.25 were from the phonon image shown in figure 3.23. The eutectic/no eutectic border is indicated by an arrow. The filled areas under the peaks represent equivalent areas of the sample with (right peak) and without (left peak) an eutectic interface. The areas under the filled peaks were found by integrating the curve using zero as the minimum y value. The percent interfacial phonon transmission calculated was 71% and 66%, respectively, which is in close agreement with the phonon image value of 70%. The reason that the bolometer intensity decreases below zero in figure 3.25 in not known.

Phonon imaging of a second sample with an initial Au thickness of 300 Å was performed to determine the reproducibility of the measurement. The resulting phonon image is shown in figure 3.26. The method of excitation was indirect. The arrow illustrates the position of the eutectic/no eutectic border. Interfacial phonon transmission was calculated to be approximately 60% indicating reproducibility.

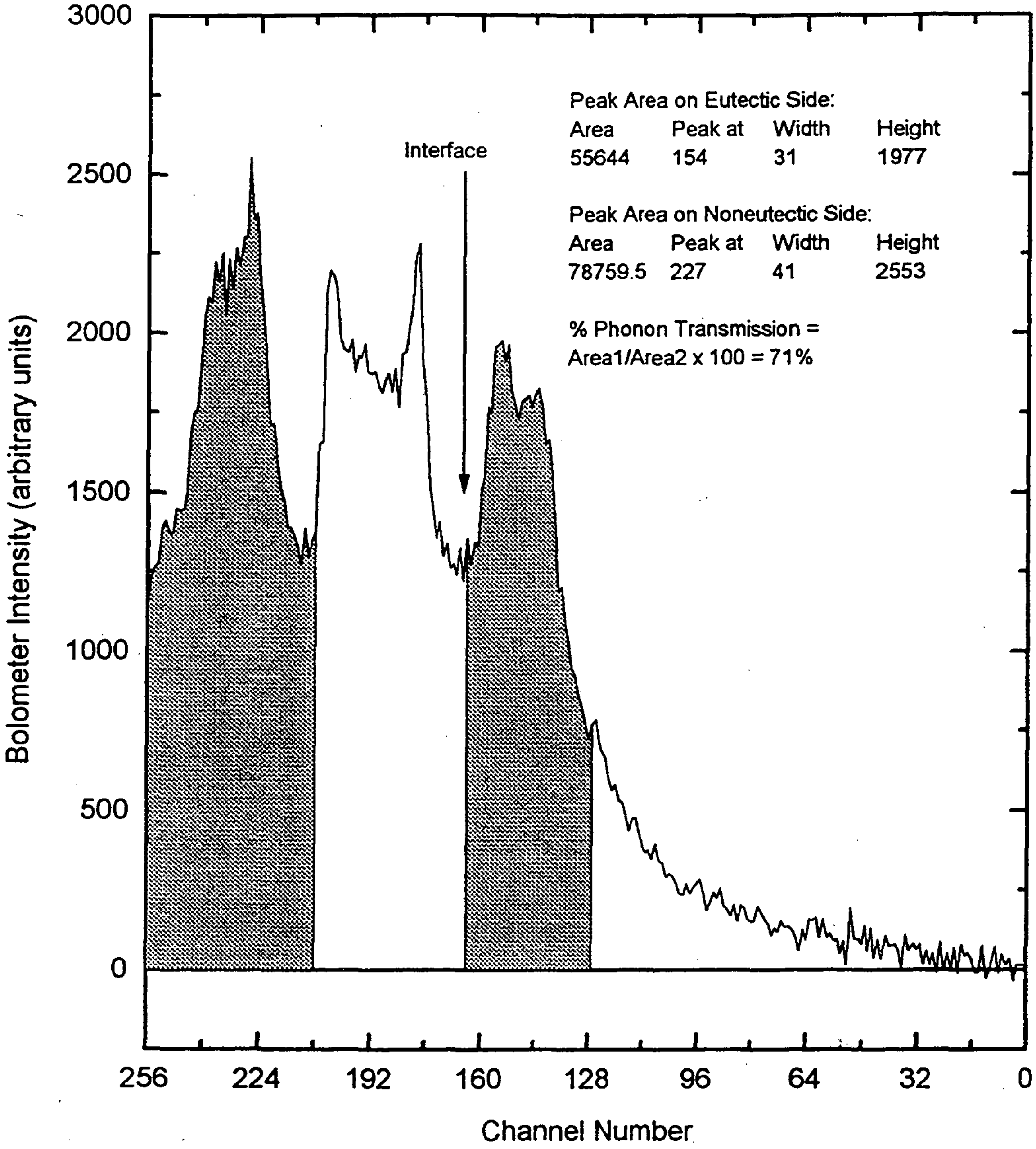

Figure 3.24: Line scan spectrum from a sample with an initial Au thickness of 300 Å per side. The filled areas under the peaks are equidistant from the bolometer center. The boundary between the eutectic/noneutectic sides is pointed out by the arrow. The calculated percent of phonon transmission is 71%.

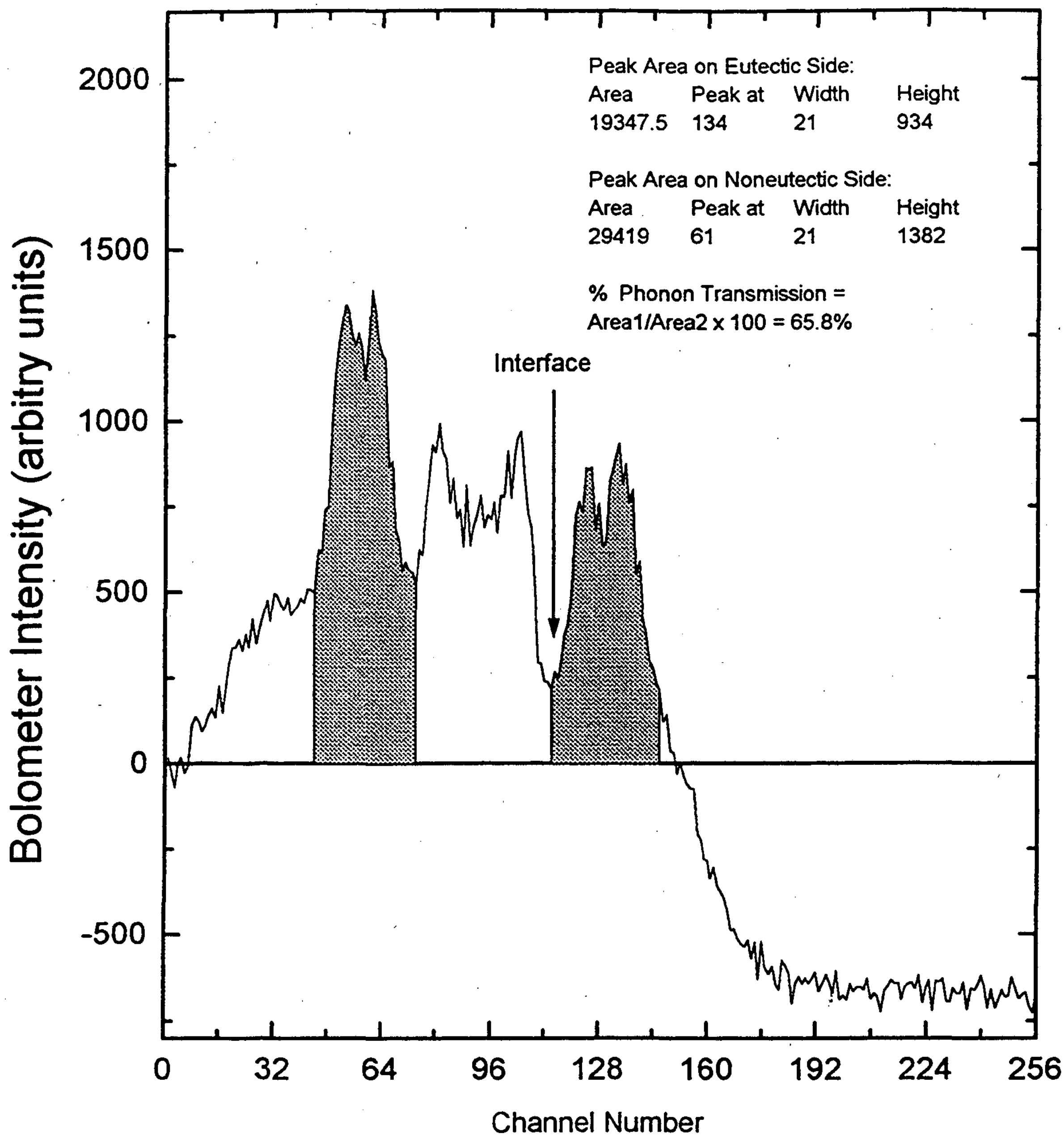

Figure 3.25: Another line scan spectrum from the sample with an initial Au thickness of 300 Å per side, but from another scan position on the sample. The filled areas under the peaks are equidistant from the bolometer center. The boundary between the eutectic/noneutectic sides is pointed out by the arrow. The calculated percent of phonon transmission is 66 %.

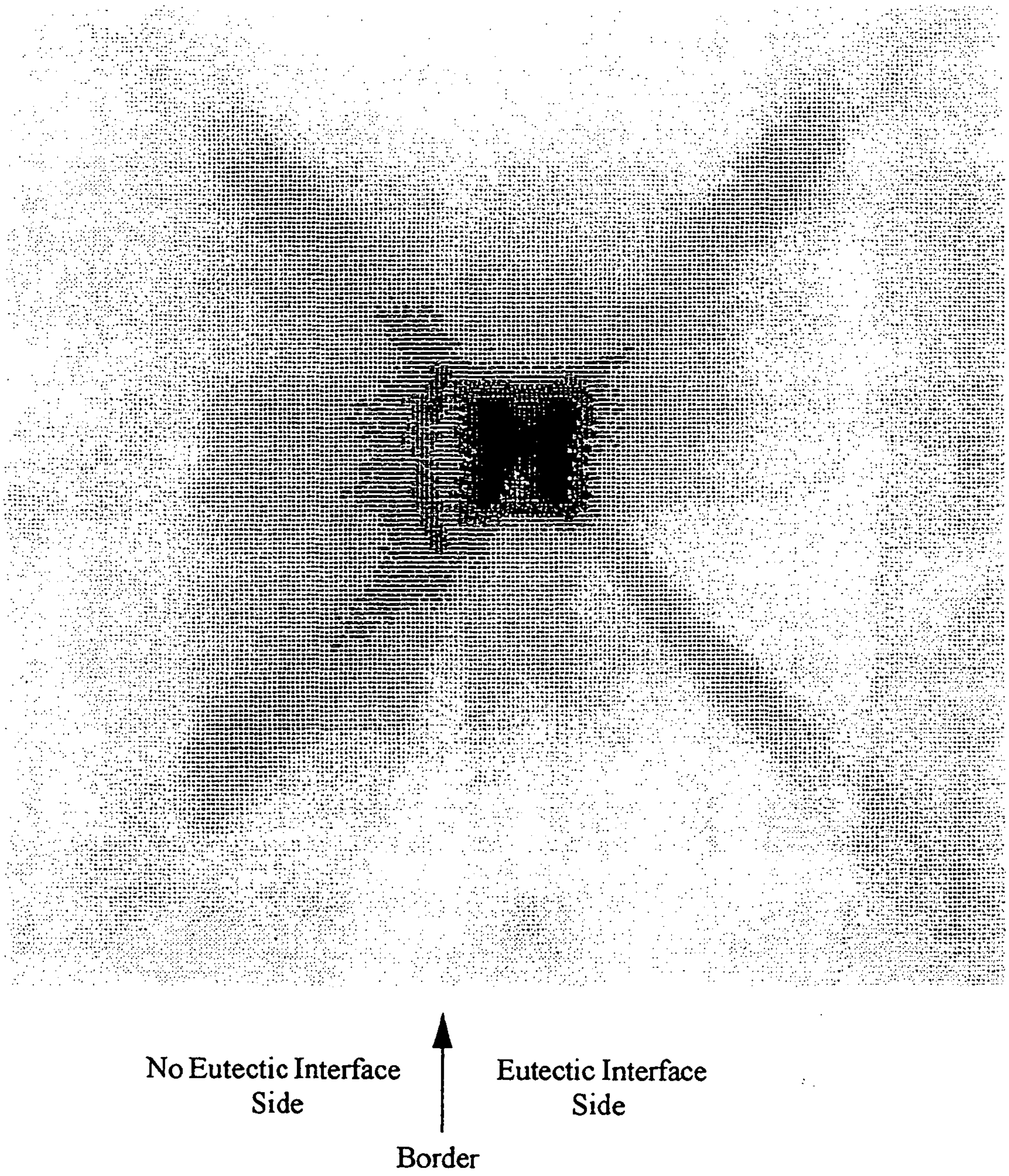

Figure 3.26: A bolometer phonon image of a Ge-Au-Ge eutectically bonded sample with an initial Au thickness of 300 Å/side by means of indirect excitation of a Cu film. The lighter vertical line (near the <1 1 0> caustic) pointed out by the arrow illustrates the boundary between the sample side with and without an eutectic interface.

Eutectic interfacial transmission experiments were carried out on several samples with an initial Au thickness of 500 Å/side. Figure 3.27 show the phonon image of one and figure 3.28 shows the phonon image of another. The bolometer giving rise to the phonon image shown in figure 3.27 was displaced far to the right of the sample boundary shown by the arrow. The bolometer displacement complicates the percent phonon transmission calculation. For the second sample, the bolometer coincides with the boundary. The percent of interfacial phonon transmission was calculated to be 50% and 65%, respectively. Hence, reproducibility was attained.

In figure 3.29, four line scan spectra of the first image are presented. The eutectic/no eutectic boundary is difficult to establish due to the displacement of the bolometer. One of the four line scans (see figure 3.29) is shown in figure 3.30. The calculated percent transmission of phonons through the eutectic interface, indicated by an arrow shown in figure 3.30, from the line scan was ~ 77%; however, this value is suspect because of the bolometer displacement.

Time of flight (TOF) data from the phonon image shown in figure 3.28 was analyzed for three reasons: first, to compare the percentage of phonon transmission through the eutectic interface, second, to determine the phonon propagation mode of the phonons before and after traversing the eutectic interface, and third, to calculate the phonon velocity. A TOF spectrum, such as the spectra shown in figure 3.13, coincides with one intensity point on a phonon image. Depending on where the point was chosen on the image, the resulting TOF spectrum can contain all three acoustic modes (e.g., in the center of the image) or only one of the acoustic modes (i.e., in one of the caustics). Several TOF data corresponding to the phonon image in figure 3.28 were taken from the

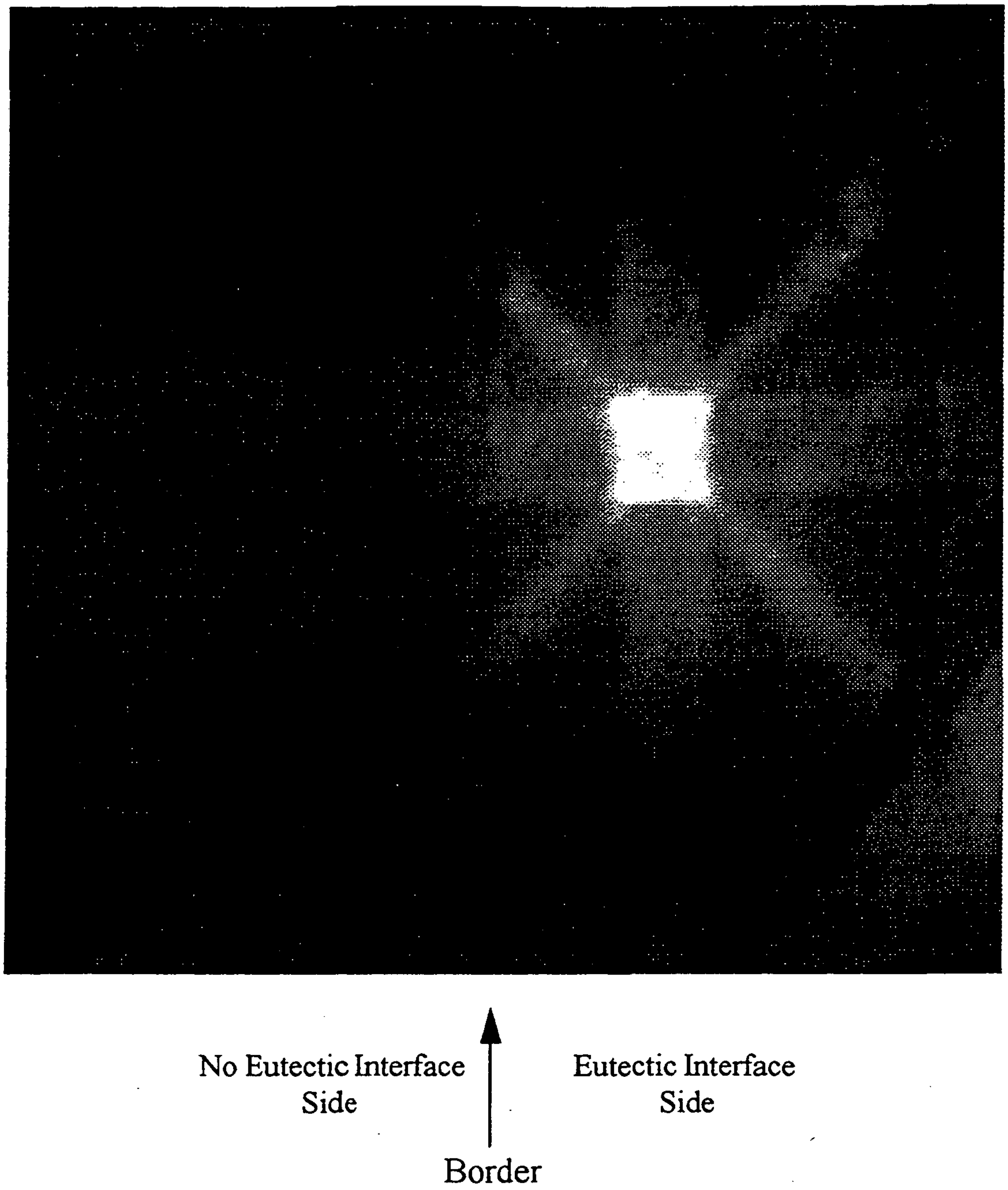

Figure 3.27: A bolometer phonon image of a Ge-Au-Ge eutectically bonded sample with an initial Au thickness of 500 Å/side. The dark vertical line to the far left pointed out by the arrow illustrates the boundary between the sample side with and without an eutectic interface. The boundary is shifted to the left because the bolometer was not deposited symmetrically to the boundary. About 50% phonon transmission was calculated for this sample.

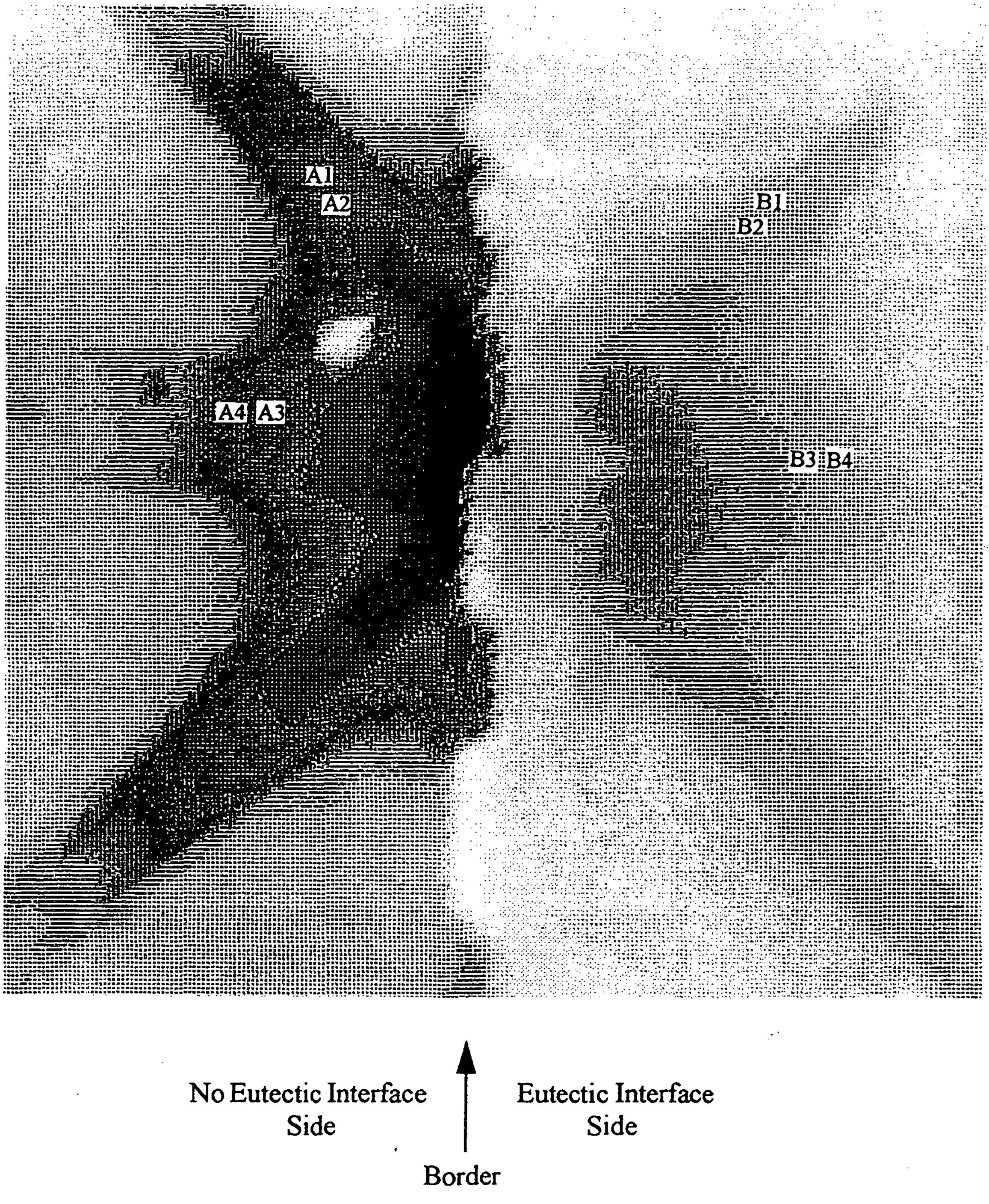

Figure 3.28: A bolometer phonon image of a Ge-Au-Ge eutectically bonded sample with an initial Au thickness of 500 Å/side by means of indirect excitation of a Cu film. The bright vertical line pointed out by the arrow illustrates the boundary between the sample side with and without an eutectic interface. The interface was 65% transparent to ballistic phonons. See the text for a definition of the labels.

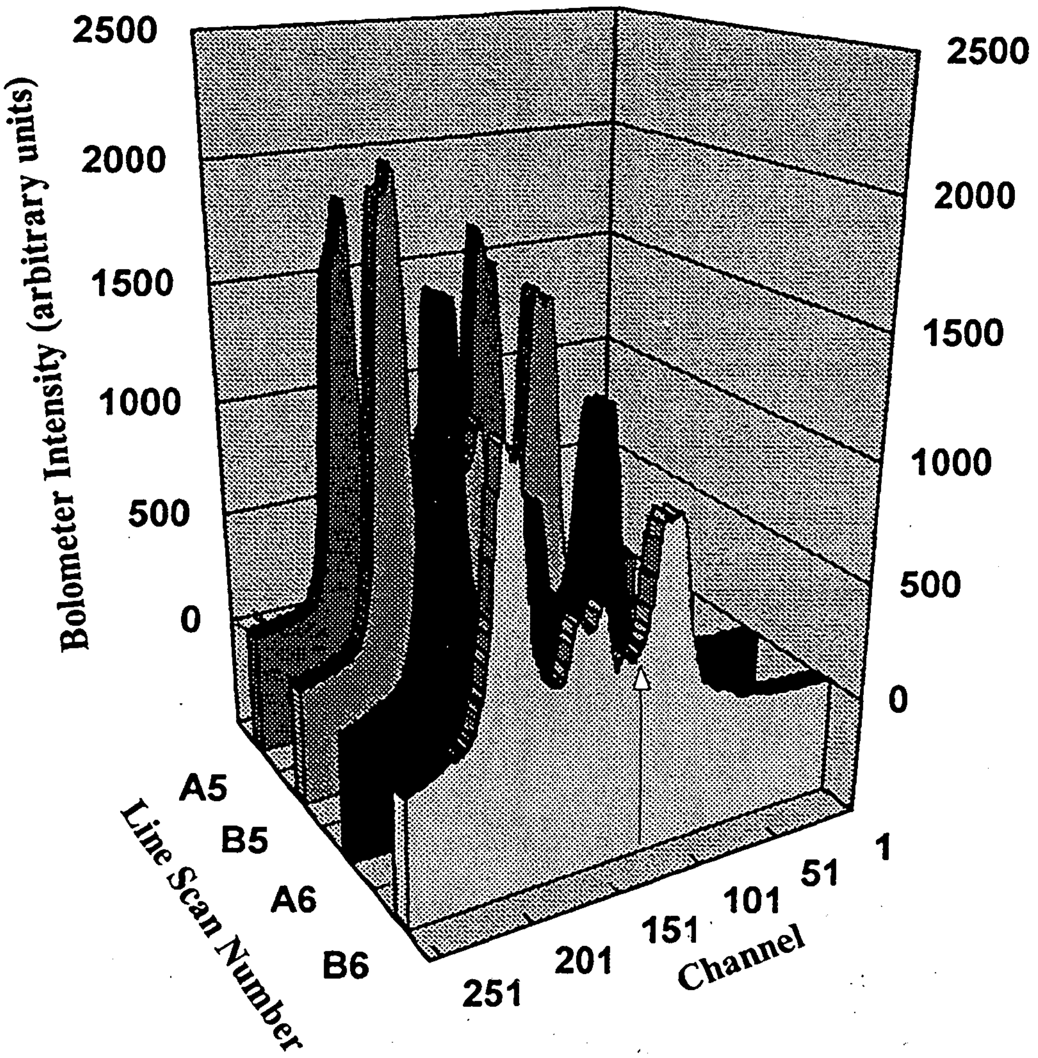

Figure 3.29: Four line scan spectra as shown in figure 3.14a. They were from the phonon image in figure 3.27. The sample had an initial Au thickness of 500 Å per side. The bolometer was displaced from the eutectic interface making the percent of phonon transmission calculation difficult to determine. The filled areas under the peaks are equidistant from the bolometer center. The boundary between the eutectic/noneutectic sides is pointed out by the arrow.

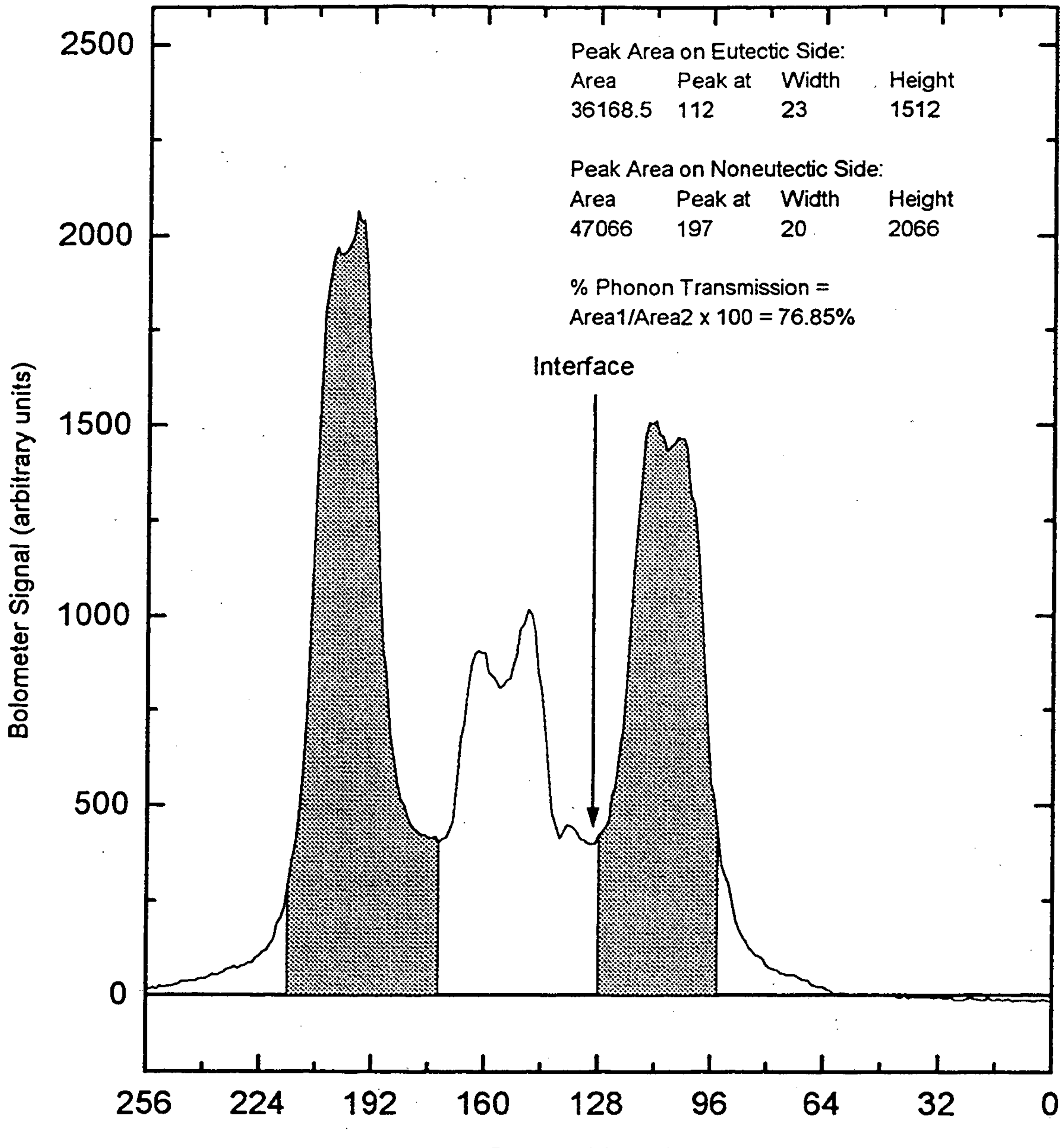

Figure 3.30: Line scan spectrum from the phonon image in figure 3.27. The sample had an initial Au thickness of 500 Å per side. The bolometer was displaced from the eutectic interface making the percent of phonon transmission calculation difficult to determine. The filled areas under the peaks are equidistant from the bolometer center. The boundary between the eutectic/noneutectic sides is pointed out by the arrow. The calculated percent phonon transmission through the eutectic interface was 77%.

sample with an initial Au thickness of 500 Å. On the phonon image, the points on the FTA caustic in the unbonded region labeled A1 and A2 are "equivalent" to the points on the FTA caustic in the bonded region labeled B1 and B2. Similar equivalent points (A3, A4, B3, B4) are labeled on the bonded and unbonded regions of the STA caustics. The FTA TOF spectra are shown in figures 3.31a and 3.31b, while the STA TOF spectra were shown in figures 3.32a and 3.32b with spectrum for each set of equivalent points plotted together for peak comparison. The first peak seen in all the spectra was due to the laser pulse. The larger peaks were from TOF data taken on the interface free sample region, while the smaller peaks were taken from the region with the eutectic interface.

The phonon propagation mode was determined by examining the peak shapes. Comparing phonon produced peaks in this spectra with the spectra resulting from diffusive scattering phenomena (figure 3.13) indicates that diffusive scattering was absent. In figure 3.32, the FTA peaks are sharp with a full peak width at half the maximum peak height (FWHM) of ~ 0.25 μs on the unbonded side and 0.20 μs on the bonded side. If the phonon propagation was ballistic, then the FWHM is equal to Δt_{QB} (see figure 3.7) and is proportional to the arrival time, L/v, where L was the sample thickness traversed by the phonon and v is the phonon velocity.[Levinson, 1986, 49] The arrival time, which is the difference between the time at which the laser was pulsed and the time at which the phonon was detected, is about 0.30 μs. The FWHM for diffusive or quasiballistic peaks are much larger than 0.3 μs, therefore the propagation mode is ballistic. The phonon velocity of each mode was calculated from the longitudinal and acoustic arrival times and the measured sample thickness. For this sample, the LA phonon velocity was

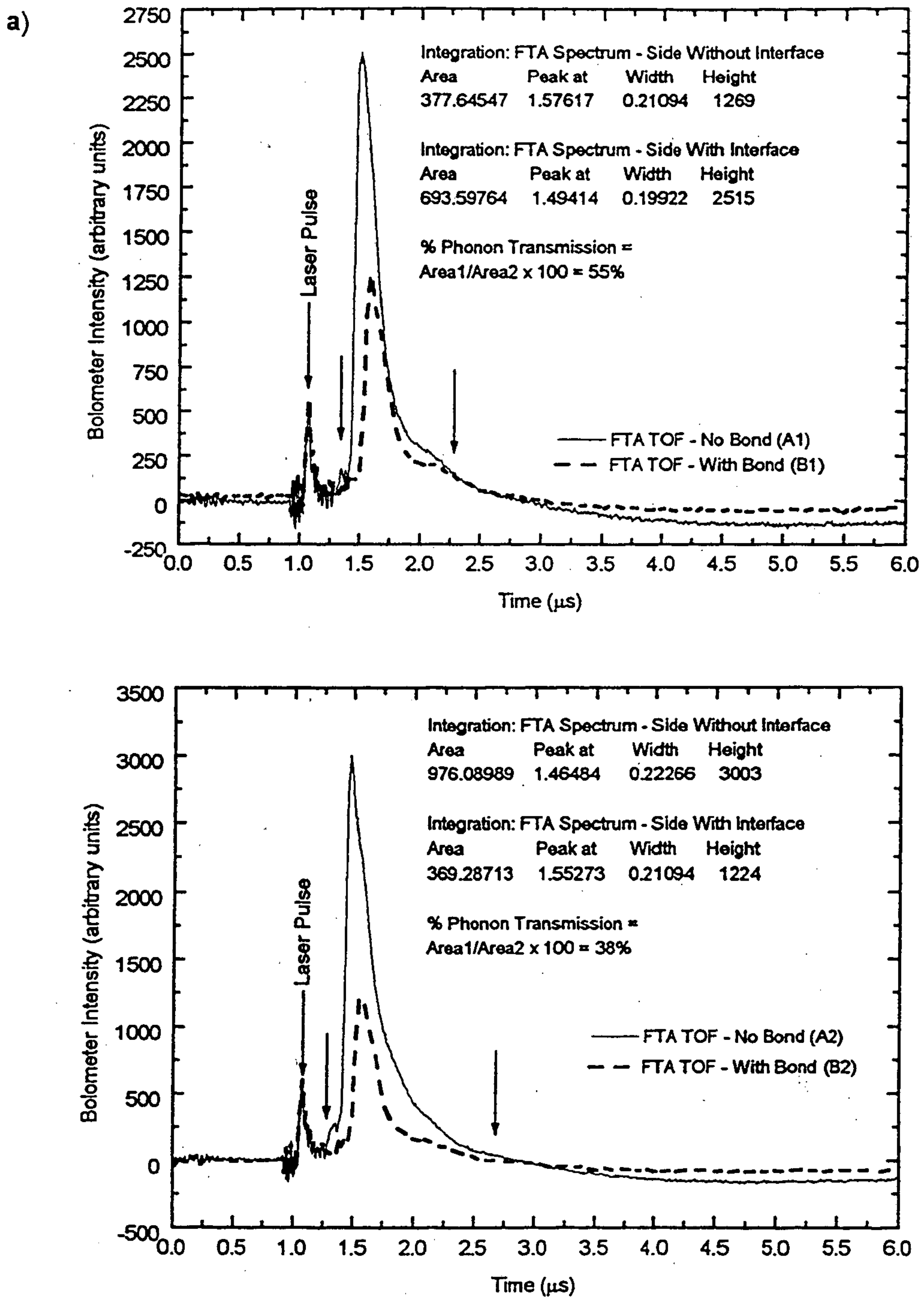

Figure 3.31: **a)** The large and small peaks of the FTA TOF spectra correspond to the bonded and unbonded regions of the sample. The initial bond Au thickness was 500 Å. **b)** This spectra was the same as in a but closer to the boundary or bolometer center, therefore the intensity of the peaks was greater.

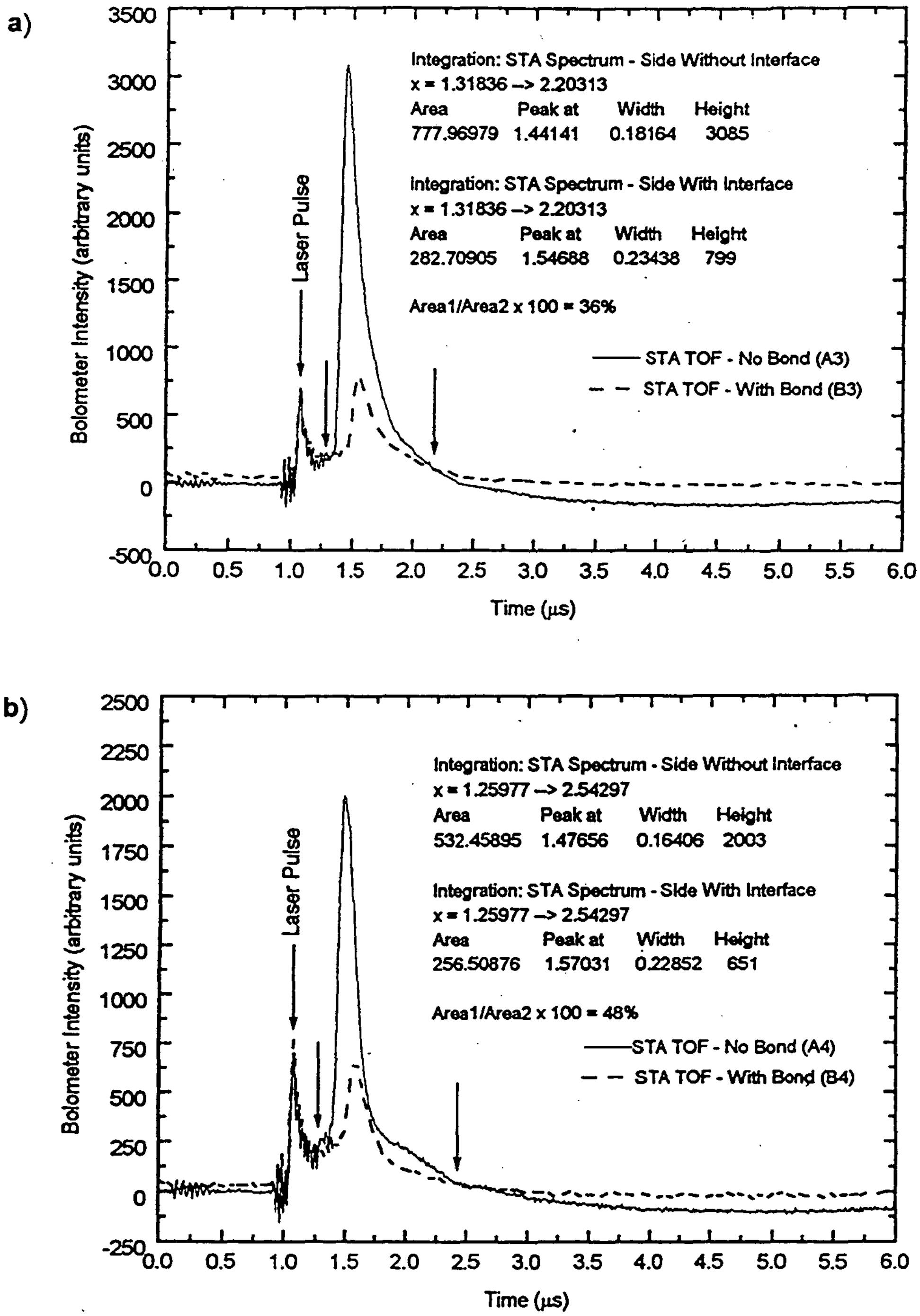

Figure 3.32: **a)** This TOF spectra was the same as in figure 3.31a, but the phonon propagation mode was STA. **b)** This spectra was the same as in figure 3.31b, but the mode was STA. The unlabeled arrows show the limits of integration for the peak are determination.

4.26×10^3 m/s, while the FTA and STA phonon velocities were 2.40×10^3 m/s and 2.31×10^3 m/s, respectively.

Information about the effect of the sample thickness and the eutectic bond on the transmission of phonons can be obtained by comparing the spectra of the bonded region with the unbonded region. The TOF peak pertaining to the bonded region of the sample was slightly shifted to the right. This effect occurs because the bonded side was thickened by the addition of the bonded sample.

The area under the peaks of equivalent points was determined and the percentage of interfacial phonon transmission was calculated using equation 3.70 (the areas replace the intensities). This percent transmission was statistically erroneous since only one point was sampled, however it was only used as an estimate. The percent transmission for the FTA TOF of figures 3.31a and 3.31b were 55% and 38% while the STA TOF of figures 3.32a and 3.32b are 48% and 36%, respectively. In all cases, the percent of phonon transmission is less than the 65% calculated for the phonon image shown in figure 3.28. Additionally, in both the FTA and STA spectra, the TOF data obtained at a point further from the bolometer center gives a more accurate value of percent transmission.

Phonon imaging studies performed on samples with an initial Au thickness of 1000 Å Au per side were performed. The percent transmission of phonons through the eutectic interface was calculated and found to be less than 5%.

It should be noted that the geometry of the sample shape was not considered in the calculations of percent phonon transmission. Since the eutectic region of the sample is thicker than the noneutectic region by approximately 900 μm, a direct comparison of phonon transmission between the eutectic and noneutectic regions may be suspect. A sample was processed in the shape of the samples imaged but without an eutectic interface to look address this issue. Unfortunately, the sample could not be imaged because of funding problems.

Finally, a structural study of the phonon imaged samples was not done. Therefore, the assumption was made that the interface of the phonon imaged samples were structurally similar to the samples which underwent structural examination. The results of this study could be more conclusive if the phonon imaged samples were structurally investigated.

4. Conclusion

This thesis presents a structural analysis and phonon transparency investigation of the Ge-Au-Ge eutectic bond interface. Interface development was intended to maximize the interfacial ballistic phonon transparency to enhance the detection of the dark matter candidate WIMPs. The process which was developed provides an interface which produces minimal stress, low amounts of impurities, and insures Ge lattice continuity through the interface.

Atomically flat and smooth bonding surfaces on (100) Ge were attained. A surface height change of less than 200 Å across a 1 mm wafer interval after chemomechanical polishing was achieved. Scattering centers were minimized due to the increased Ge interface coverage and decreased Au coverage when using thin films less than 500 Å per substrate side. In addition, little stress contrast and low dislocation density at the interface was seen by TEM indicating stress was not a significant factor in interfacial phonon impedance. Heteroepitaxial growth of Au on Ge gave rise to about a 1.55% and 28% lattice mismatch in the [200] and [02]$\bar{2}$ directions, respectively. In sections of the interface, lattice continuity was attained via the [001] homoepitaxial growth of Ge through the interface.

For initial Au thicknesses of greater than 1000 Å Au per substrate side, eutectic epitaxial growth resulted in a Au dendritic structure with 95% cross sectional and 90% planar Au interfacial area coverages. In sections in which Ge bridged the interface, lattice continuity across the interface was apparent. Epitaxial solidification of the eutectic interface with initial Au thicknesses ≤ 500 Å per substrate side produced Au agglomerations thereby reducing the Au planar interfacial area coverage to as little as 30%. The mechanism for Au coalescence was attributed to lateral diffusion of Ge and Au in the liquid phase during solidification.

Phonon transmission studies were performed on eutectic interfaces with initial Au thicknesses of 1000 Å, 500 Å, and 300 Å per substrate side. Phonon imaging of eutectically bonded samples with initial Au thicknesses of 300 Å/side revealed reproducible interfacial percent phonon transmissions from 60% to 70%. Line scan phonon imaging verified the results. Phonon propagation TOF spectra distinctly showed the predominant phonon propagation mode was ballistic. This was substantiated by phonon focusing effects apparent in the phonon imaging data.

The percent of interfacial phonon transmission was reproducible in eutectically bonded samples containing initial Au thicknesses of 500 Å/side. Percent phonon transmission through the eutectic interface from 50% to 65% was validated by phonon imaging line scan data. Phonon imaging established that the classical ballistic propagation mode was predominant following phonon interface transmission in samples with Au thicknesses of 500 Å/side. This was supported by phonon propagation time of flight data.

Only one eutectically bonded sample with an initial Au thickness of 1000Å/ side was tested and had less than 5% transmission of phonons through the eutectic interface. However, a Si-Au-Si eutectically bonded sample with an initial Au thickness of 1000 Å/side attained similar results (~ 4% percent phonon transmission). Moreover, the TOF spectrum showed the prevalence of diffusive rather than ballistic phonon mode propagation.

The degree of interface transparency to phonons and resulting phonon propagation modes correlate with the structure of the interface following eutectic solidification. Structural studies of samples with initial Au thicknesses of 1000 Å/side appear to correspond with the phonon transmission study. The eutectic interface of these samples showed a Au area coverage of 90% and gave rise to less than 5% phonon transmission accompanied by diffusive mode propagation. Phonon imaging of samples with an initial Au thickness of 500 Å/side or less revealed significant amounts of phonon transmission and definite ballistic mode propagation. Structural studies indicated Au agglomeration accompanied by Ge lattice continuity through the interface was critical to enhanced phonon transmission and ballistic mode propagation.

5. References

1. Almazouzi, A., *et al.*, *Diffusion, solubility, and thermodynamic properties of gold in solid germanium studied by means of radio tracer and spreading-resistance analysis*, J. Appl. Phys. **70**, 1345 (1991).
2. Anderson, A.C., *The Kapitza thermal boundary resistance between two solids*, Proceedings of a NATO Advanced Study Institute on Nonequilibrium Superconductivity, Phonons, and Kapitza Boundaries, 1980, (Plenum Press, 1981), **65**, p. 1.
3. Ashcroft, N.W. and N.D. Mermin, Solid State Physics, (W.B. Saunders Company, Philadelphia, 1976), p. 826.
4. Ba, L., *et al.*, *Fractals in annealed Ge-Au/Au bilayer films*, Journal of Applied Physics 77, 587 (1995).
5. Barrett, C. and T.B. Massalski, Structure of Metals: Crystallographic Methods, Principles and Data, (Pergamon Press, Oxford, 1980), p. 654
6. Beck, H., *et al.*, *Phonon hydrodynamics in solids*, Physica Status Solidi (a) **24**, 11 (1974).
7. Bernstein, L., *Semiconductor joining by the solid-liquid-interdiffusion (SLID) Process*, J. of the Electrochemical Society **113**, 1282 (1966).
8. Blakemore, J.S., Solid State Physics, (Cambridge University Press, Cambridge, 1985), p. 506.
9. Bracht, H., *et al.*, *Diffusion and solubility of copper, silver, and gold in germanium*, Physics Review B **43**, 14 (1991).

10. Brandes, E.A. and G.B. Brook, Smithells Metals Reference Book, (Butterworth-Heinemann Ltd, Oxford, 1992), p. 14.

11. Bron, W.E., *Studies of nonequilibrium dynamics in the time domain*, Proceedings of a NATO Advanced Study Institute on Nonequilibrium Phonon Dynamics, 1984, (Plenum Press, 1985), **124**, p. 165.

12. Bron, W.E., in *Nonequilibrium Phonons in Nonmetallic Crystals*, edited by Eisenmenger, W. and A.A. Kaplyanskii (North-Holland Physics Publishing, Amsterdam, 1986), p. 91.

13. Bron, W.E., *Ultrashort transient dynamics of phonons and electrons*, Physics of Phonons, Proceedings of the XXIII Winter School of Theoretical Physics, 1987, (Springer-Verlag, 1987), **285**, p. 236

14. Chang, C.-a., *Ambient effects on thin film interactions*, MRS Proceedings, 1983, (North-Holland, 1984), **25**, p. 111.

15. Chang, C.-A. and G. Ottaviani, *Outdiffusion of Si through gold films: The effects of Si orientation, gold deposition techniques and rates, and annealing ambients*, Applied Physics Letters **44**, 901 (1984).

16. Chang, P.H., *et al.*, *Transmission electron microscopy of gold-silicon interactions on the backside of silicon wafers*, Journal of Applied Physics **63**, 1473 (1988).

17. Cros, A. and C. Canella, *The role of epitaxy in Au-Si eutectic bonding*, Journal of Adhesion Science & Technology **5**, 1041 (1991).

18. Cullity, B.D., Elements of X-Ray Diffraction, (Addison-Wesley Publishing Co., Inc., Reading, 1978), p. 555.

19. Dubey, M., *et al.*, *Growth of single crystal Ge films on GaAs and InGaP and highly oriented Au films on Ge*, Appl. Phys. Letters **64**, 2697 (1994).

20. Edwards, W.D., *et al.*, *Specific contact resistance of ohmic contacts to gallium arsenide*, Solid-State Electronics **15**, 387 (1972).

21. Every, A.G., *General, closed-form expressions for acoustic waves in cubic crystals*, Physical Review Letters **42**, 1065 (1979).

22. Every, A.G., *et al.*, *Ballistic phonon imaging in sapphire: bulk focusing and critical-cone channeling effects*, Physical Review B **29**, 2190 (1984).

23. Feuchtwang, T.E., *Dynamics of a semi-infinite crystal lattice in a quasiharmonic approximation. I. the static equilibrium configuration of a semi-infinite lattice*, Physical Review **155**, 715 (1967).

24. Feuchtwang, T.E., *Dynamics of a semi-infinite crystal lattice in a quasiharmonic approximation. II. the normal-mode analysis of a semi-infinite lattice*, Physical Review **155**, 731 (1967).

25. Feynman, R.P., *et al.*, <u>The Feynman Lectures on Physics</u>, (Addison-Wesley Publishing Company, Reading, 1963), p. 14-2

26. Galkina, T.I., *Generation and propagation of phonons in crystalline and amorphous silicon under optical excitation*, Physics of Phonons, Proceedings of the XXIII Winter School of Theoretical Physics, 1987, (Springer-Verlag, 1987), **285**, p. 410

27. Gaskell, D.R., <u>Introduction to Metallurgical Thermodynamics</u>, (Hemisphere Publishing Corp., New York, 1981), p. 611.

28. Hansen, W.L. and E.E. Haller, in *Encyclopedia of Applied Physics*, edited by Trigg, G.L. (VCH Publishers and American Institute of Physics, Brooklyn, 1992), p. 55

29. Heime, K., *et al.*, *Very low resistance Ni-AuGe-Ni contacts to n-GaAs*, Solid-State Electronics **17**, 835 (1974).

30. Hellawel, A., The Growth and Structure of Eutectics with Silicon and Germanium, (Pergamon Press Ltd, Oxford, 1970), p. 78.

31. Hensel, J.C. and R.C. Dynes, *Interaction of electron-hole drops with ballistic phonons in heat pulses: the phonon wind*, Physical Review Letters **39**, 969 (1977).

32. Hensel, J.C. and R.C. Dynes, *Observation of singular behavior in the focusing of ballistic phonons in Ge*, Physical Review Letters **43**, 1033 (1979).

33. Höss, C., *et al.*, *Total internal reflection of high-frequency phonons: a test of specular refraction*, Physical Review Letters **64**, 1134 (1990).

34. Huebener, R.P., *et al.*, *Ballistic phonon signal for imaging crystal properties*, Materials Science and Engineering **B5**, 157 (1990).

35. Hull, D. and D.J. Bacon, Introduction to Dislocations, (Pergamon Press, Oxford, 1984), p. 257.

36. Iliadis, A. and K.E. Singer, *The role of germanium in evaporated Au-Ge ohmic contacts to GaAs*, Solid State Electronics **26**, 7 (1983).

37. Incorporated, D.O., Operation and Maintenance Manual for the D-305 Interferometer, Davidson Optronics Inc., unknown.

38. Iwanari, S. and K. Takayanagi, *Surfactant epitaxy of Si on Si(111) surface mediated by a Sn layer: I. Reflection electron microscope observation of the growth with and without a Sn layer mediate the step flow*, Journal of Crystal Growth **119**, 229 (1992).

39. Iwanari, S. and K. Takayanagi, *Surfactant epitaxy of Si on Si(111) surface mediated by a Sn layer: II. critical step flow of the growth with and without mediate*, Journal of Crystal Growth **119**, 241 (1992).

40. Jackson, H.E. and C.T. Walker, *Thermal conductivity, second sound and phonon-phonon interactions in NaF*, Physical Review B **3**, 1428 (1971).

41. Kazakovtsev, D.V. and Y.B. Levinson, *Phonon diffusion with frequency down-conversion*, Physica Status Solidi (b) **96**, 117 (1979).

42. Kazakovtsev, D.V. and Y.B. Levinson, *Theory of formation, dynamics and explosion of a phonon hot spot*, Physics of Phonons, Proceedings of the XXIII Winter School of Theoretical Physics, 1987, (Springer-Verlag, 1987), **285**, p. 276

43. Kelly, A. and G.W. Groves, Crystallography and Crystal Defects, (TechBooks, Herndon, 1970), p. 428.

44. Kittel, C., Introduction to Solid State Physics, (John Wiley & Sons, Inc., New York, 1986), p. 646.

45. Knowlton, W.B., Analysis of photolithography procedures as used in $CuInSe_2$/CdS thin film photovoltaic device processing for optimization purposes, National Renewable Energy Laboratory, 1989.

46. Knowlton, W.B., *et al.*, *Ge-Au eutectic bonding of Ge {100} Crystals*, Journal of Low Temperature Physics **93**, 343 (1993).

47. Koos, G.L., *et al.*, *Critical-cone channeling of thermal phonons at a sapphire-metal interface*, Physical Review Letters **51**, 276 (1983).

48. Levinson, Y.B., *Nonlocal phonon heat transfer*, Solid State Communications **36**, 73 (1980).

49. Levinson, Y.B., in *Nonequilibrium Phonons in Nonmetallic Crystals*, edited by Eisenmenger, W. and A.A. Kaplyanskii (North-Holland Physics Publishing, Amsterdam, 1986), p. 91.

50. Li, T.P.L., *et al.*, *AES/ESCA/SEM/EDX studies of die bond materials and interfaces*, Reliability Physics 22nd Annual Proceedings, IEEE, 1984, p. 169.

51. Little, W.A., *The transport of heat between dissimilar solids at low temperatures*, Canadian Journal of Physics **37**, 334 (1959).

52. Loretto, M.H., Electron Beam Analysis of Materials, (Chapman and Hall, London, 1984), p. 210

53. MacDonald, W.D. and T.W. Eagar, in *Annual Rev. Mater. Sci*, edited (Annual Reviews Inc., 1992), p. 23.

54. Maris, H.J., *Enhancement of heat pulses in crystals due to elastic anisotropy*, The Journal of the Acoustical Society of America **50**, 812 (1971).

55. Maris, H.J., in *Nonequilibrium Phonons in Nonmetallic Crystals*, edited by Eisenmenger, W. and A.A. Kaplyanskii (North-Holland Physics Publishing, Amsterdam, 1986), p. 51.

56. Maris, H.J., *Phonon propagation with isotope scattering and spontaneous anharmonic decay*, Physical Review B **41**, 9736 (1990).

57. Marx, D. and W. Eisenmenger, *Phonon scattering at siliconcrystal surfaces*, Zeitschrift für Physik B - Condensed Matter **48**, 277 (1982).

58. McCurdy, A.K., *et al.*, *Anisotropic heat conduction in cubic crystals in the boundary scattering regime*, Physical Review B **2**, 4077 (1970).

59. McQuarrie, D.A., Quantum Chemistry, (University Science Books, Mill Valley, 1983), p. 517.

60. Miller, G.G. and M.J.P. Musgrave, *On the propagation of elastic waves in aeolotropic media: I. media of cubic symmetry*, Proceedings of the Royal Society of London A **236**, 352 (1956).

61. Musgrave, M.J.P., *On the propagation of elastic waves in aeolotropic media: I. general principles*, Proceedings of the Royal Society of London A **226**, 339 (1954).

62. Musgrave, M.J.P., *On the propagation of elastic waves in aeolotropic media: I. media of hexagonal symmetry*, Proceedings of the Royal Society of London A **226**, 356 (1954).

63. Musgrave, M.J.P., *The propagation of elastic waves in crystals and other anisotropic media*, Reports on Progress in Physics **22**, 74 (1959).

64. Musgrave, M.J.P., Crystal Acoustics: Introduction to the Study of Elastic Waves and Vibrations in Crystals, (Holden-Day, San Francisco, 1970), p. 288.

65. Nagle, R.K. and E.B. Saff, Fundamentals of Differential Equations, (The Benjamin/Cummings Publishing Co., Inc., Redwood City, 1989), p. 682.

66. Neumann, G., in *Landolt-Börnstein: Numerical data and functional relationships in science and technology*, edited by Mehrer, H. (Springer-Verlag, Berlin, 1990), p. 148.

67. Nilsson, G. and G. Nelin, *Phonon dispersion relations in Ge at 80 K*, Phys. Rev. B **3**, 364 (1971).

68. Nolder, R.L. and D.N. Malone, *Gold-silicon preform, die attach system*, Reliability Physics 25th annual proceedings, IEEE, 1987, p. 169.

69. Northrop, G.A., *Phonon imaging*, Ph.D. Thesis, University of Illinois at Urbana-Champaign, 1982.

70. Northrop, G.A. and J.P. Wolfe, *Ballistic phonon imaging in solids - a new look at phonon focusing*, Physical Review Letters **43**, 1424 (1979).

71. Northrop, G.A. and J.P. Wolfe, *Ballistic phonon imaging in germanium*, Physical Review B **22**, 6196 (1980).

72. Northrop, G.A. and J.P. Wolfe, *Phonon imaging: theory and applications*, Proceedings of a NATO Advanced Study Institute on Nonequilibrium Phonon Dynamics, 1984, (Plenum Press, 1985), **124**, p. 165.

73. Northrop, G.A. and J.P. Wolfe, *Phonon reflection imaging: a determination of specular versus diffuse boundary scattering*, Physical Review Letters **52**, 2156 (1984).

74. Nye, J.F., Physical Properties of Crystals: Their Representation by Tensors and Matrices, (Oxford University Press, Oxford, 1957), p. 322.

75. Okamoto, H. and T.B. Massalski, in *Binary Alloy Phase Diagrams*, edited by Massalski, T.B., J.L. Murray, L.H. Bennett and H. Baker (William W. Scott, Jr., Metals Park, 1984), p. 263.

76. Parker, S.P., McGraw-Hill Concise Encyclopedia of Science and Technology, (McGraw-Hill Publishing Co., New York, 1989), p. 992

77. Philofsky, E., *et al.*, *Phase transformations in eutectic gold-silicon alloys on single-crystal silicon*, J. Electrochem. Soc.: Solid-State Science and Technology **119**, 527 (1972).

78. Pietsch, G.J., *et al.*, *Chemomechanical polishing of silicon: Surface termination and mechanism of removal*, Applied Physics Letters **64**, 3115 (1994).

79. Poate, J.M., *et al.*, Thin Films - Interdiffusion and Reactions, (John Wiley & Sons, New York, 1978), p. 428.

80. Pomerantz, M. and R.J. von Gutfeld, *Heat pulse studies of phonon scattering by impurities in Si and Ge*, Proceedings of the Ninth International Conference on the Physics of Semiconductors, 1968, (Publishing House Nauka, 1968), **2**, p. 690.

81. Porter, D.A. and K.E. Easterling, Phase Transformations in Metals and Alloys, (Chapman & Hall, London, 1981), p. 446.

82. Procop, M. and B. Sandow, *Au-Ge based ohmic contacts on GaAs*, Physica Status Solidi A **95**, K211 (1986).

83. Robinson, G.M., *et al.*, *Optical interferometry of surfaces*, Scientific American **July**, 66 (1991).

84. Rösch, F. and O. Weis, *Geometric propagation of acoustic phonons in monocrystals within anisotropic continuum acoustics: Part I. sapphire an quartz*, Zeitschrift für Physik B **B25**, 101 (1976).

85. Rösch, F. and O. Weis, *Geometric propagation of acoustic phonons in monocrystals within anisotropic continuum acoustics: Part II. diamond, silicon an germanium*, Zeitschrift für Physik **B25**, 115 (1976).

86. Rösch, F. and O. Weis, *Phonon transmission from incoherent radiators into quartz, sapphire, diamond, silicon and germanium within anisotropic continuum acoustics*, Zeitschrift für Physik B **B27**, 33 (1977).

86a. Schroder, D.K., Semiconductor Material and Device Characterization, (John Wiley & Sons, Inc., New York, 1990), p. 599.

87. Seeger, K., Semiconductor Physics: An Introduction, (Springer-Verlag, Berlin, 1991), p. 502.

88. Serway, R.A., Physics for Scientists and Engineers with Modern Physics, (Saunders College Publishing, Philadelphia, 1986), p. 1108.

89. Shields, J.A., *The scattering of high-frequency acoustic phonons in silicon and GaAs*, Ph.D. Thesis, University of Illinois at Urbana-Champaign, 1992.

90. Shutt, T., *Personal communication: pulse arrival times versus RC and NTD time constants*, 1994.

91. Steinbrüchel, C., *The scattering of phonons of arbitrary wavelength at a solid:solid interface: model calculation and applications*, Zeitschrift für Physik B **B24**, 293 (1976).

92. Stockwell, W., *et al.*, *Cryogenic germanium detectors for a WIMP dark matter search*, SPIE **2280**, 374 (1994).

93. Taborek, P. and D.L. Goodstein, *Diffuse reflection of phonons and the anomalous Kapitza resistance*, Physical Review B **22**, 1550 (1980).

94. Taylor, B., *et al.*, *Phonon focusing in solids*, Physical Review Letters **23**, 416 (1969).

95. Taylor, B., *et al.*, *Focusing of phonons in crystalline solids due to elastic anisotropy*, Physical Review B **3**, 1462 (1971).

96. Thomas, G. and M.J. Goringe, Transmission Electron Microscopy of Materials, (John Wiley & Sons, New York, 1979), p. 388

97. Tiller, W.A., The Science of Crystallization: Macroscopic Phenomena and Defect Generation, (Cambridge University Press, Cambridge, 1991), p. 483.

98. Tuah-Poku, I., *et al.*, *A study of the transient liquid phase bonding process applied to a Ag/Cu/Ag sandwich joint*, Metallurgical Transactions **19A**, 675 (1988).

99. Viswanathan, K.S., *Phonon Focusing in Crystals*, Physics of Phonons, Proceedings of the XXIII Winter School of Theoretical Physics, 1987, (Springer-Verlag, 1987), **285**, p. 301.

100. von-Gutfeld, R.J., in *Physical Acoustics: Principles and Methods*, edited by Mason, W.P. (Academic Press, New York, 1968), p. 233.

101. von-Gutfeld, R.J. and J. A.H. Nethercot, *Heat pulses in quartz and sapphire at low temperatures*, Physical Review Letters **12**, 641 (1964).

102. Wagner, R.S. and W.C. Ellis, *Vapor-liquid-solid mechanism of single crystal growth*, Applied Physics Letters **4**, 89 (1964).

103. Wang, N., *A cryogenic phonon detector to search for dark matter particles*, Ph.D. Thesis, University of California at Berkeley, 1991.

104. Weis, O., *Thermal phonon radiation*, Zeitschrift für Angewandte Physik **26**, 325 (1969).

105. Weis, O., *Reflection, transmission and mode conversion of plane sound waves at a plane interface between two different anisotropic solids*, Zeitschrift für Physik B **B34**, 55 (1979).

106. Weis, O., in *Nonequilibrium Phonons in Nonmetallic Crystals*, edited by Eisenmenger, W. and A.A. Kaplyanskii (North-Holland Physics Publishing, Amsterdam, 1986), p. 1.

107. Weis, O., *Phonon scattering at plane interfaces and surfaces*, Physics of Phonons, Proceedings of the XXIII Winter School of Theoretical Physics, 1987, (Springer-Verlag, 1987), **285**, p. 313

108. Wilk, G.D., *et al.*, *Low-temperature homoepitaxial growth on Si(111) mediated by thin overlayers of Au*, Appl. Phys. Letters **65**, 866 (1994).

109. Wolfe, J.P., *Ballistic heat pulses in crystals*, Physics Today **33**, 44 (1980).

110. Xiong, F., *et al.*, *Liquid-metal-mediated homoepitaxial film growth of Ge at low temp*, Applied Physics Letters **59**, 3586 (1991).

111. Yost, F.G., *Ultimate strength and morphological structure of eutectic bonds*, Journal of Electronic Materials **3**, 353 (1974).

112. Zhang, R., *et al.*, *The fractal character of anneal-induced aggregation in bylayer films of the Ge-Au and Ge-Ag systems*, Thin Solid Films **208**, 295 (1992).

113. Ziman, J.M., Principles of the Theory of Solids, (Cambridge University Press, Cambridge, 1972), p. 435.

Appendix A: The P2 Device

The purpose of the P2 (phonon detector 2) experiment was to examine the effect of initial Au thickness and epitaxial continuity on phonon propagation through the Ge-Au eutectic interface on a prototype composite phonon mediated detector. The P2 device, shown in figure A1, consisted of 4 neutron transmutation doped (NTD) (100) Ge bolometers eutectically bonded to an antenna. The antenna was a large mass (~17g) p-type (100) Ge antenna (N_A-N_D ~ $2x10^{12}cm^{-3}$). The initial Au thicknesses for the bolometers were 300 Å/side, 500 Å/side, and two 1000 Å/side. Epitaxial continuity was eliminated on one of the 1000 Å/side interfaces by misorienting the bolometer with respect to the antenna by rotating the bolometer ~10° parallel to the interface. The experimental procedure and results are described elsewhere. [Stockwell, et al., 1994, 92] Briefly, phonons were created in the antenna which propagated through the eutectic interface and were detected by the NTD bolometers. Two heat pulsing methods were used to produce phonon excitation (events): electrical heat pulsing (1.56 MeV) and gamma ray interaction. Detection of the events indicated that neither initial Au thickness nor epitaxial continuity through the interface affected the heat pulse shape. Each bolometer showed the same intensity per time for an event (see figure A2). The bolometers were to integrate the phonon-produced signal quickly (without phonon reflection), effectively acting as a black body. However, this did not occur. Further studies are necessary to determine why this occurred.

The purpose of this appendix is to discuss why ballistic phonon propagation is not present in the P2 experiment. Several aspects of the P2 experiment are noted to explain why ballistic phonon propagation was not seen and that the cause was not the Ge-Au-Ge eutectic interface. The following points are noted.

- Even if ballistic propagation was the predominant mode of phonon propagation in the P2 experiment, the RC time constant of the electronics used to measure interactions is not fast enough (~ 60 μs) to measure the ballistic component (~ 0.5 μs/2 mm from TOF data) of the interaction. That is, the antenna was 6 mm in height resulting in a calculated ballistic propagation mode arrival time of about 1.5 μs; therefore, the electronics are too slow to see it. Additionally, the NTD RC time constant is considered to be about 100 μs. Furthermore, the pulse arrival time in the P2 experiment was within the range of not less than 10 μs up to 200 μs. Consequently, neither the NTD RC time constant nor the pulse arrival time allowed the ballistic phonon mode to be detected.[Shutt, 1994, 90]

- The question is, what type of excitation is produced by: 1) a heat pulse, and 2) gamma ray? The excitation is high for the gamma ray. For the heat pulse, the power transmitted to the film is about 1.56 MeV, which is large enough to be a high excitation.

- The propagation mode for this experiment was not classical because of the interaction type. The type of interaction was of high excitation, so spontaneous decay did occur. The ballistic propagation mode(or other classical modes) did not exist. The closest propagation mode to the ballistic is the quasiballistic mode. The difference between the two is shown in figure 3.7. Clearly, the shape of the TOF pulses acquired in the phonon imaging experiments are ballistic in nature (see figures 3.31a, 3.31b, 3.32, 3.32b). A plot of a heat pulse obtained in the P2 experiment is shown in figure A2. The inset plot is shown with a time scale indicative of those seen in the phonon imaging studies. Certainly, a comparison of the pulse shapes in figure A2 with figure 3.7 indicates the pulse method was a high excitation type. Therefore, either quasiballistic or quasidiffusive nonequilibrium phonon propagation modes were produced in the P2 experiment.[Levinson, 1986, 49]

- The reasons listed above are why a difference is not seen in the energy pulses in P2 as a function of Au thickness. Regardless of whether or not the interface was causing a propagation mode conversion from ballistic to diffusive, the only phonon propagation mode that was detectable was the quasidiffusive mode. Furthermore, the scattering occurring at the interface would not cause a complete phonon propagation mode conversion from ballistic to diffusive of the Au thickness used in the P2 experiment (the 1000 Å/side bolometer was inactive). In other words, of the propagation modes existing following interface transmission, the ballistic mode was certainly prevalent as seen in the phonon imaging experiments.

- According to Levinson, excitation of superthermal phonons in isotopically pure crystals at low temperatures is necessary to observe quasiballistic propagation (to prevent Umklapp processes), and, to his knowledge, no one has done such an experiment. [Levinson, 1986, 49]

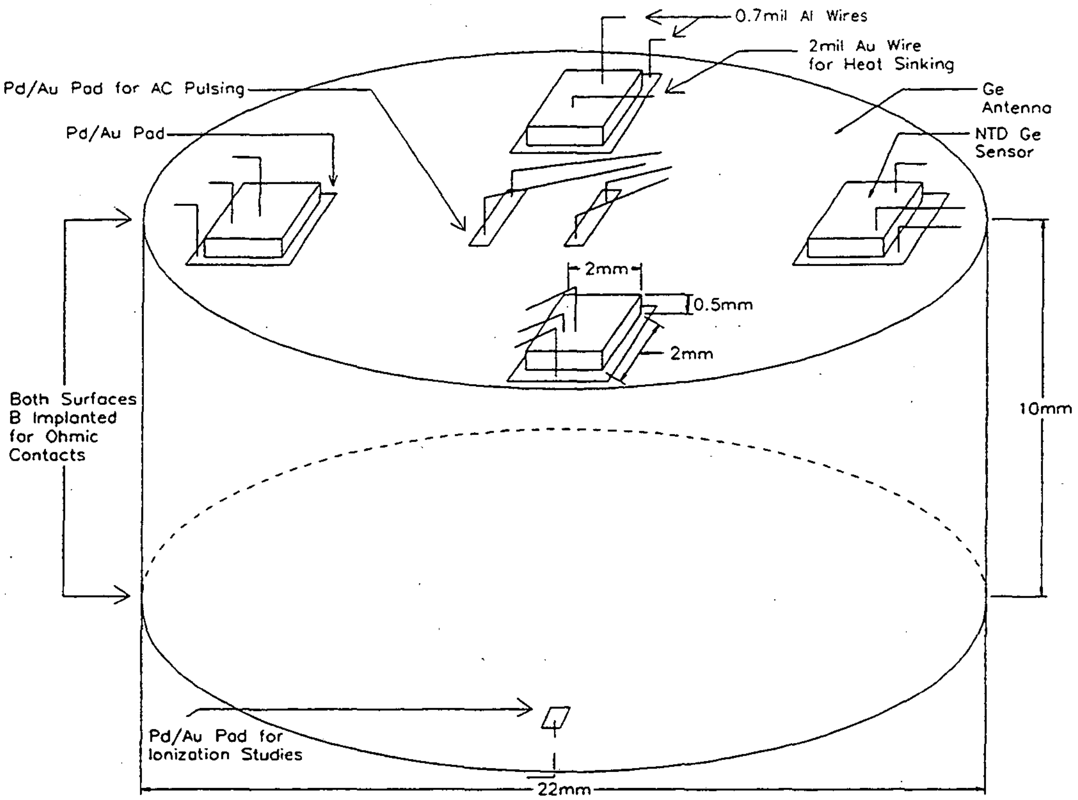

Figure A1: The P2 device.

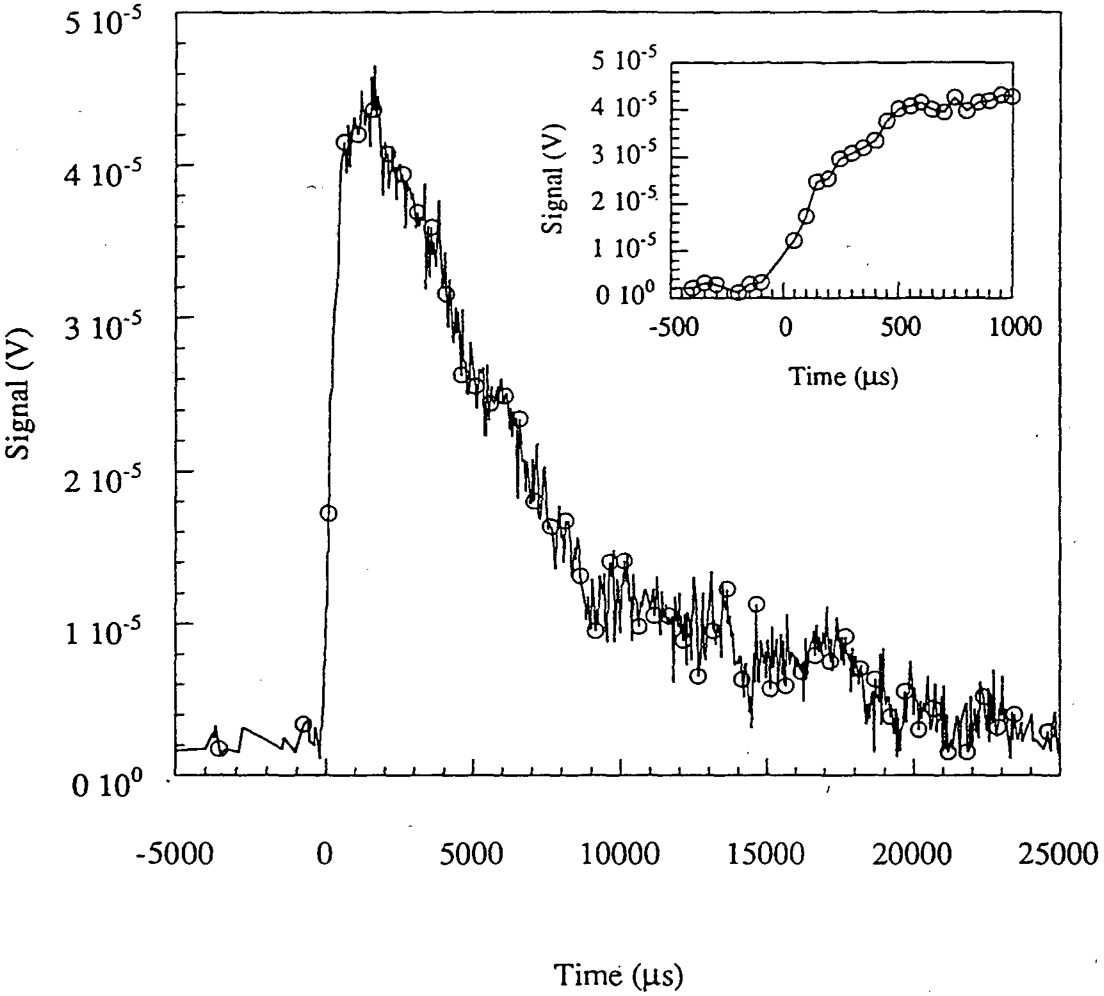

Figure A2: A heat pulse spectrum as detected from the P2 device. The inset was an attempt to show the pulse on a similar time scale as the time of flight (TOF) spectra shown in figures 3.31 and 3.32. The slow rise time and even slower fall time of the heat pulse indicates the propagation mode is quasidiffusive.

LAWRENCE BERKELEY LABORATORY
CENTER FOR ADVANCED MATERIALS
1 CYCLOTRON ROAD
BERKELEY, CALIFORNIA 94720